

AD 722131

RESEARCH ON IMAGING PROPERTIES OF OPTICAL PARAMETRIC UPCONVERTER

FINAL REPORT

AIL REPORT 8585-1

by

W. Chiou and F. Pace

July 1971

Prepared under

Contract N00014-70-C-0161

ARPA Order No. 306, Amendment 17

Program Code 9E30K21

for

Office of Naval Research
Washington, D. C. 20360

AIL, a division of Cutler-Hammer
Deer Park, New York 11729

Reproduced by
NATIONAL TECHNICAL
INFORMATION SERVICE
Springfield, Va. 22151

176

DISCLAIMER NOTICE

THIS DOCUMENT IS THE BEST
QUALITY AVAILABLE.

COPY FURNISHED CONTAINED
A SIGNIFICANT NUMBER OF
PAGES WHICH DO NOT
REPRODUCE LEGIBLY.

RESEARCH ON IMAGING PROPERTIES OF OPTICAL PARAMETRIC UPCONVERTER

FINAL REPORT

AIL REPORT 8585-1

by

W. Chiou and F. Pace

July 1971

Prepared under

Contract N00014-70-C-0161

ARPA Order No. 306, Amendment 17

Program Code 9E30K21

for

**Office of Naval Research
Washington, D. C. 20360**

**AIL, a division of Cutler-Hammer
Deer Park, New York 11729**

SUMMARY

The imaging properties of parametric upconversion have been investigated analytically and experimentally for the case of monochromatic object waves, and photographs of upconverted $10.6\text{ }\mu\text{m}$ images obtained.

Analyses: Using geometric optics an expression was derived relating the locations of the object, the pump and the upconverted image. It was found that in general the image quality is degraded by a thickness aberration resulting from sum-frequency contributions from each differential slab of the nonlinear interaction material. The magnitude of this first order thickness aberration was found to approach zero for the case of plane wave pump interacting with plane wave object waves. The angular aperture of the upconverter was found to be determined by the phase match conditions. The effect of higher order factors such as crystal birefringence, phase mismatch, and pump wave divergence were considered qualitatively.

The analysis was then extended by applying the techniques of physical optics. Using Fourier transformer formalism an expression was derived relating the angular spectrum of the sum-frequency field with that of the object and pump fields. Phase mismatch, crystal birefringence, and the effects of a finite aperture were included in this analysis. Two cases were examined in detail, one using a plane wave pump and the other with a Gaussian distributed pump beam. The Gaussian pump case was found to suffer more image degradation than the plane wave case which approached the diffraction limit.

A characteristic equation was developed to describe the overall performance of the image upconverter. Object scene radiance, image detail, exposure time, quantum conversion efficiency, detector sensitivity and the interaction aperture are related to a universal constant.

Experimental Results: A series of image upconversion experiments were carried out with a 10.6- μm illuminated object, a 1.06- μm pump and an oriented proustite crystal (Ag_3AsS_3). The line spread functions were measured for two upconversion configurations: plane wave interactions and the Gaussian shaped pump beam. Measured results on image location, aberrations, the field of view, and angular resolution agree reasonably well with the theoretical results. For the plane wave pump case about 70 x 20 resolution elements were measured. Two dimensional images of a resolution test chart have been recorded on photographic film.

Conclusions: As a result of this analytical and experimental investigation it is concluded that the monochromatic image upconversion process can approach diffraction limited operation if the upconversion process takes place with plane wave object and pump beams (Fourier space interaction).

A parametric study has been done for such imaging upconverter characteristics as conversion efficiency, number of resolution elements, pump power, pump power density, crystal figure of merit, and overall sensitivity. This approach indicates some present limitations of the upconversion process and the future possibilities that can be based on the extrapolation and trends in the present technology.

Publications: 1. W. Chiou, "Geometric Optics Theory of Parametric Image Upconversion," Journal of Applied Physics, Vol 42, p 1985, March 1971.

2. W. Chiou and F. Pace, "Image Upconversion of Infrared 10.6- μm Radiation," IEEE/OSA Conference on Laser Engineering and Applications, Washington, D.C. June 1971.

Table of Contents

	Page
Chapter 1 Introduction	1
Chapter 2 Geometric Optics Theory of Parametric Image Upconversion	7
I Introduction	7
II Image Formation by Infinitesimally Thin Image Upconverter	8
III Aberrations of Image Upconverter with Nonlinear Material of Finite Thickness	15
IV Extended Pump Source, Angular Aperture, and Resolution	25
V Other Factors Affecting Image Formation of Image Upconverter	38
VI Conclusion	40
Chapter 3 Physical Optics Theory of Parametric Image Upconversion	43
I Introduction	43
II General Formulation	44
III Angular Spectrum of Image Field for Several Image Upconversion Systems	58
Chapter 4 Sensitivity of An Image Upconversion System	81
I Introduction	81
II Characteristic Equation of an Ideal Image Upconverter System	82

Table of Contents (Cont)

	Page
III Performance of a Non-ideal Image Upconverter System	88
IV Noise Equivalent Power of an Image Upconverter	94
Chapter 5 Image Upconversion Experiments	97
I General Consideration	97
II Experimental Arrangement	99
III Measurement of Line Spread Functions	101
IV Measurement of Resolution and Infrared Object Field of View	113
V Sum-Frequency Images of Resolution Test Chart with Fourier Configuration Up-converter	119
VI Imaging Upconverter Sensitivity	133
References	141
Appendix A Fourier Representation of Complex Field Distribution	145
Appendix B Wave Equation for Angular Spectrum	147
Appendix C Fourier Integral Representation of Non-linear Polarization	151
Appendix D Mismatch Factor	153
Appendix E Hankel Transform of $\frac{\sin(ax^2)}{(ax^2)}$	157
Appendix F Evaluation of Mismatch Factor for Nearly Isotropic Crystal ($\xi \approx 0$)	159

List of Illustrations

Figure		Page
1	Phase-Match Condition for Parametric Upconversion	10
2	Formation of Image With Infinitesimally Thin Upconverter	12
3	Image Formation for Parametric Upconverter with Finite Thickness Nonlinear Material	17
4	Normalized Thickness Aberration as a Function of Axial Object Distance, With Pump Position as a Parameter	26
5	Thickness Coma of an Image Upconverter as a Function of Axial Object Distance	27
6	Angular Relations in Crystallographic Coordinate System	30
7	Phase-Match Angles for Ag_3AsS_3 10.6 to 0.96 μm Upconversion	32
8	Crystal Orientation and Angular Aperture for Ag_3AsS_3 10.6 to 0.96 μm Image Upconverter	33
9	Blurring of Sum-Frequency Image Due to Aberrations of Parametric Upconverter	35
10	Resolution Calculation	36
11	Relation Between the Coordinates (x, y, z) and the Crystallographic Axis (X, Y, Z)	48
12	Geometric Representation of Mismatch Relation	52

List of Illustrations (Cont)

Figure		Page
13	Illustration of Double Refraction of Sum-Frequency Wave	56
14	Geometric Relation Used to Obtain Characteristic Equation of the Image Upconverter	85
15	Experimental Arrangement for Parametric Image Upconversion	100
16	Intensity Profile of Sum-Frequency Beam at the Input Surface of Image Lens No. 11.	103
17	Line Spread Function of a Fourier Configuration Upconverter System	105
18	Line Spread Function of a Fourier Configuration Upconverter	106
19	Experimental Arrangement to Realize an Upconverter With Gaussian Beam Pump and Cylindrical Object Wave	108
20	Line Spread Functions Measured at Different Distance From Lens No. 11 (Gaussian Beam Pump and Cylindrical Object Wave Configuration)	110
21	Experimental Setup for Measurements of Resolution and Field of View	115
22	On-Axis and Off-Axis Spread Function of Fourier Configuration Upconverter	117
23	Measured Off-Axis Line Spread Function	118

List of Illustrations (Cont)

Figure		Page
24	Resolution Test Chart	121
25	Intensity Profile of 0.967 μm Image of 10.6 μm Illuminated Resolution Target Elements 1/1 Through 1/6	125
26	Intensity Profile of 0.967 μm Image of 10.6 μm Illuminated Resolution Target Elements 1/1 Through 1/6	126
27	Intensity Profile of 0.967 μm Image of 10.6 μm Illuminated Resolution Target Elements 1/4, 1/5, 1/6 and 0/1	127
28	Intensity Profile of 0.967 μm Image of 10.6 μm Illuminated Resolution Target Elements 0/4 Through 0/6	128
29	Intensity Profile of 0.967 μm Defocussed Image of 10.6 μm Illuminated Resolution Target Elements 1/1 Through 1/6	129
30	Intensity Profile of 0.967 μm Image of 10.6 μm Illuminated Resolution Target Elements 1/1 Through 1/6 (Multi-Mode 1.06 μm Pump)	130
31	0.967 μm Image of 10.6 μm Illuminated Resolution Test Target	132
F-1	Wave Vector Relation	161

CHAPTER 1. INTRODUCTION

This is the final report under Contract N00014-70-C-0161 having as its objective the demonstration and operation of a 10.6- μm image converter system with as high a conversion efficiency as possible, a resolution of 150×150 resolution elements and noise equivalent power (NEP) of 10^{-12} watt/ $\text{Hz}^{1/2}$.

The parametric image upconverter represents a new class of infrared (IR) device technology. It combines the following characteristics hitherto unattainable:

- Permits detection of 10.6- μm radiation by conventional image tube techniques
- Obtains imaging in real time (no mechanical scanning as in present FLIR's)
- Inherently low noise
- Operates at or near room temperature
- Can be designed for any wavelength in the 1 to 13 μm region
- Coherent (upconverter can preserve frequency and phase)

In the IR parametric upconverter technique, a strong laser pump at ω_p is employed to upconvert IR signal radiation ω_{IR} to the sum-frequency $\omega_s = \omega_{\text{IR}} + \omega_p$ in the visible or near visible region of the spectrum. The frequency translation is achieved by propagating three waves (signal, pump, and sum-frequency) nearly collinearly and phase-matched in a crystal (such as proustite) having a large value of nonlinear susceptibility. The upconverted signal can then be detected by a photoemissive device such as a photomultiplier, image orthicon, image intensifier, or silicon vidicon. The use of an Nd:YAG laser is contemplated as a pump source due to its CW, pulsed high-power output capability, and mode purity. Moreover, higher quantum

efficiency photocathodes and silicon vidicon are presently under development at the upconverter output wavelength.

A. PROGRAM APPROACH

The approach chosen to achieve the program objectives includes the following tasks:

- Obtain analytical expressions for image upconversion analogous to the thick lens formula by means of a modified geometrical optics technique
- Use physical optics techniques to predict image upconverter line and point spread functions
- Measure the line spread function of the upconverter, at various positions in the field of view. Investigate effect of Gaussian distribution of pump beam to the image resolution.
- Investigate and compare the characteristics of two generic upconverter systems, the one with the nonlinear material in the image space and the other with the nonlinear material in the Fourier space. The objective is to simultaneously optimize conversion efficiency and image quality.
- Incorporate all of the previous findings into a laboratory device that demonstrates an image with quality approaching the 150×150 resolution element program objective
- Measure and optimize image quality, conversion efficiency, and NEP in the demonstration setup

B. ANALYTICAL RESULTS

Qualitative descriptions of parametric image upconversion are currently available in literature. However, very little has been published on the quantitative considerations necessary for selection and evaluation of image upconverter systems possessing acceptable image and sensitivity characteristics.

Analyses and experiments, designed to fill this gap, were carried out.

Imaging properties of a parametric image upconversion process are investigated both theoretically and experimentally in the present study. The theoretical treatment given here is more rigorous than previous work^(13,14,15). The particular case of the nonlinear interaction of a monochromatic object wave and a monochromatic pump wave is considered. The theory can easily be extended to the case of the polychromatic object waves if one considers a monochromatic object wave as a Fourier component of polychromatic object radiation.

The geometric optics theory of the parametric image upconversion is presented in Chapter 2. A ray tracing technique is used in the analysis. If the phase relation of object waves is not conserved by the parametric process, the ray tracing technique is not valid. The coherent nature of the process, necessary for the effective interaction of the three waves (signal, pump, and sum frequency), transfers the phase of the object waves to the sum-frequency waves. This consideration qualitatively justifies the geometric optics treatment on the parametric image upconversion process. A more rigorous justification is given below. A formula relating the locations of a point object, a point pump source, and an upconverted point image is obtained for a dispersive infinitesimal slab of nonlinear material. It is assumed in the analysis that all waves are phase matched and are paraxial. An image produced by a finite thickness nonlinear crystal is next considered. A finite thickness crystal gives rise to thickness aberrations because the upconverted image position is different for the various differential slabs of the crystal. Thickness aberrations are inherent in the process and differ from lens aberrations in ordinary lenses. The amount of aberrations for several different upconversion systems is analyzed. It is found that the converter pumped by a plane wave pump and interacting with a plane object

wave is free of thickness aberrations. The angular aperture of the upconverter is shown to be determined by the phase-match condition. The effect of diverging pump beam on image quality is also considered. The effect of other less important factors, such as crystal birefringence and phase mismatch is considered qualitatively.

The parametric image upconversion process is analyzed in Chapter 3 by the physical optics technique. The purpose of this analysis is twofold; the first is to obtain an expression for the upconverted image field in terms of the infrared object field, the second is to confirm the ray tracing techniques used in the geometric optics theory. The Fourier transform formalism is adopted here because of the complexity of the object wave and the image wave. A wave equation for the angular spectrum (Fourier component) of field disturbances with a source term is obtained. The angular spectrum of non-linear polarization wave is considered to be the source term in the wave equation. The wave equation is solved using a technique developed by Kleinman⁽²³⁾. Phase mismatch and crystal birefringence are included in this treatment. The solution relates the angular spectrum of sum-frequency field to that of infrared object field. An equation relating the positions of upconverted image, object, and pump is obtained by using stationary phase condition. The equation is identical with that derived in the geometric optics theory if crystal birefringence is negligibly small. This result clarifies the range of validity of geometric optic theory. The analysis also confirms that aberrations exist for finite interaction lengths. The result agrees with the thickness aberration predicted in the geometric optics analysis as described above. Several different image upconverter systems are analyzed. It is shown that the amount of aberration for a plane wave pumped upconverter is independent of the object position if object wave is not a plane wave. This result agrees with that of the geometric optics treatment. The special case of Gaussian distribution beam pumped upconverter is considered. It is found that Gaussian beam pump can, under certain condition, introduces additional degradation in the upconverted image.

The characteristic equation which describes overall system performance of an image upconverter is considered in Chapter 4. This equation relates infrared object radiance, the amount of image detail, exposure time, quantum conversion efficiency, detector sensitivity, and the interaction aperture to a characteristic constant $h\nu_i$, where h is Planck constant and ν_i is infrared frequency of monochromatic object radiation. Characterization of an image upconverter enables one to understand the limiting performance of a particular system.

C. EXPERIMENTAL RESULTS

Two image upconverter configurations have been considered for imaging experiments. Image properties of two upconverter configurations, namely:

- Plane wave object and plane wave pump
- Spherical wave object and plane wave pump have been measured

The first configuration was chosen because of its low thickness aberrations. The second configuration was chosen because, although it has a larger value of aberration, it provides a check on this theory

Image properties were evaluated by measuring the line spread function first rather than recording an image of a resolution test pattern. The line spread function technique uses simple one-dimensional measurement techniques and the data obtained can provide a description of the system in the formalism of optical transfer functions employed in optical image resolution analyses.

Measured data on image location, image size, and number of resolution elements show reasonable agreement with theoretically calculated values. The field of view of the experimental system was 12 degrees. The number of resolvable elements contained in this field of view was 70 (one element/3 milliradians).

Upconverted images at $0.967\text{ }\mu\text{m}$ of a $10.6\text{ }\mu\text{m}$ illuminated resolution test chart are then quantitatively measured with the scanning technique and are recorded on photographic films. The images recorded contain 70×20 resolution elements.

As a result of the theoretical and experimental study, it is found that the monochromatic image upconversion process can be nearly diffraction limited.

CHAPTER 2. GEOMETRIC OPTICS THEORY OF PARAMETRIC IMAGE UPCONVERSION

I. INTRODUCTION

The photomultiplier detection of infrared (IR) radiation by means of the parametric upconversion process⁽¹⁻⁵⁾ has stimulated great interest in the next step of upconversion of IR images⁽⁶⁻⁹⁾ to the visible or near-visible region. The theory of parametric upconversion is well-established⁽¹⁰⁻¹²⁾; however, image upconversion requires considerations beyond those for single-resolution element theory. Firester analyzed the problem using both Fourier transform⁽¹³⁾ and geometric optics⁽¹⁴⁾ approaches. Because of the simplifying assumptions in his analysis, some interesting image upconverter properties are not apparent in his results. Andrews⁽¹⁵⁾ has reported resolution calculations, also based on a ray-tracing method, of image upconverters utilizing specific optical systems. His analysis applies for a near-plane wave pump and therefore does not cover the case of an off-axis IR object.

In this paper, the discussion is limited to image aspects of the upconverter; the problems common to a single-resolution element upconverter (such as conversion efficiency, bandwidth, and material selection) are not considered.

A formula relating the location of the upconverted image to location of the pump and the IR object is derived in Section II for a very thin upconverter. The result shows that a point IR object will be imaged into a point. The formation of the upconverted image by a thick upconverter is considered in Section III. The finite thickness of the nonlinear material causes aberrations peculiar to the parametric image upconversion.

II. IMAGE FORMATION BY INFINITESIMALLY THIN IMAGE UPCONVERTER

This section contains a discussion of the formation of the sum-frequency image of an IR object by an infinitesimally thin upconverter. Infinitesimally thin means that the thickness of the nonlinear material is small compared with other dimensions such as the object, pump, and image distances and the transverse dimensions of the crystal, but that it is larger than the wavelengths involved; that is, large enough for traveling-wave parametric interaction inside the nonlinear material. For this case, it will be shown that a point IR object is imaged to a point sum-frequency image.

The image location is obtained by tracing spherical pump rays, spherical IR object rays, and spherical sum-frequency rays that are parametrically interacting in the nonlinear material. For simplicity, the analysis is carried out in a two-dimensional model.

To further simplify the analysis, the following assumptions are made:

1. The pump, the IR object, and the sum-frequency waves are in near-phase-match condition throughout the interaction volume; the slight phase mismatch is neglected.
2. Because all rays are paraxial, all the angles are small enough to use the approximation $\tan \theta \approx \theta$.
3. The pump is a point source. The pump beam generated by a single-transverse-mode laser can be considered as a point source. (The effect of an extended pump source, which represents a multi-transverse-mode laser beam, will be considered later.)

4. The reflected components of the pump, the IR object, and especially the sum-frequency and higher-order scattered waves⁽¹⁶⁾ generated at the surface of the material are ignored because these rays do not contribute to the image formation.

The first assumption is justified since the maximum allowable phase mismatch is small compared with the other wave vectors involved. Assumptions 2 and 3 are discussed in Section IV.

To provide a consistent convention for the use of positive and negative quantities in the analysis, simple Cartesian coordinates are used. If α' and ψ' are defined as the angles of the IR wave vector K_i and the sum-frequency wave vector K_s , measured from the pump-wave vector K_p (Figure 1) inside the nonlinear material, the phase-match condition results in the following relationship:

$$\sin \psi' = \frac{K_i}{K_s} \sin \alpha'$$

For paraxial approximation,

$$\psi' \approx \frac{K_i}{K_s} \alpha' = \beta \alpha' \quad (1)$$

The angular demagnification factor $\beta = K_i/K_s$ is not constant because $|K_i|$ and $|K_s|$ change with direction; however, for a small-angle approximation, the change is neglected.

Because of the change in the indices of refraction at the air-crystal interface, the direction of the wave vectors inside the nonlinear material will be modified according to Snell's law, as shown in Figure 2b. The relationships between the angles are:

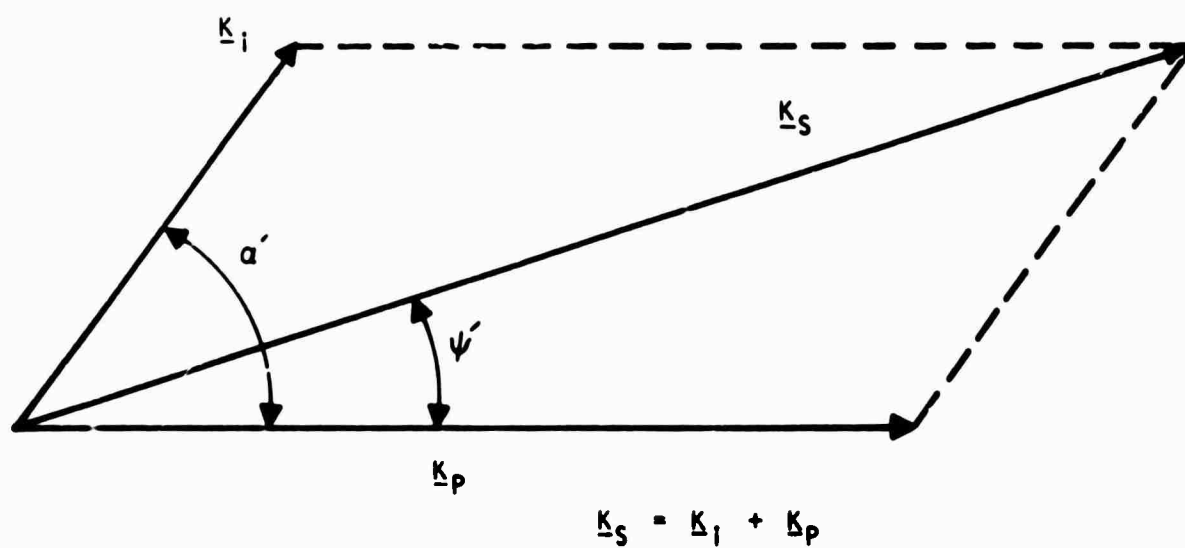


FIGURE 1. PHASE-MATCH CONDITION FOR PARAMETRIC UPCONVERSION

$$\begin{aligned}\theta'_p &= \frac{\theta_p}{n_p} \\ \theta'_i &= \frac{\theta_i}{n_i} = \frac{1}{n_i} (\theta_p + \alpha)\end{aligned}\tag{2}$$

where

θ_ℓ ($\ell = i, p, s$) = angle between K_ℓ ($\ell = i, p, s$) and
the reference axis normal to the
interface

n_ℓ ($\ell = i, p, s$) = index of refraction for the wave designated
by the subscript ℓ

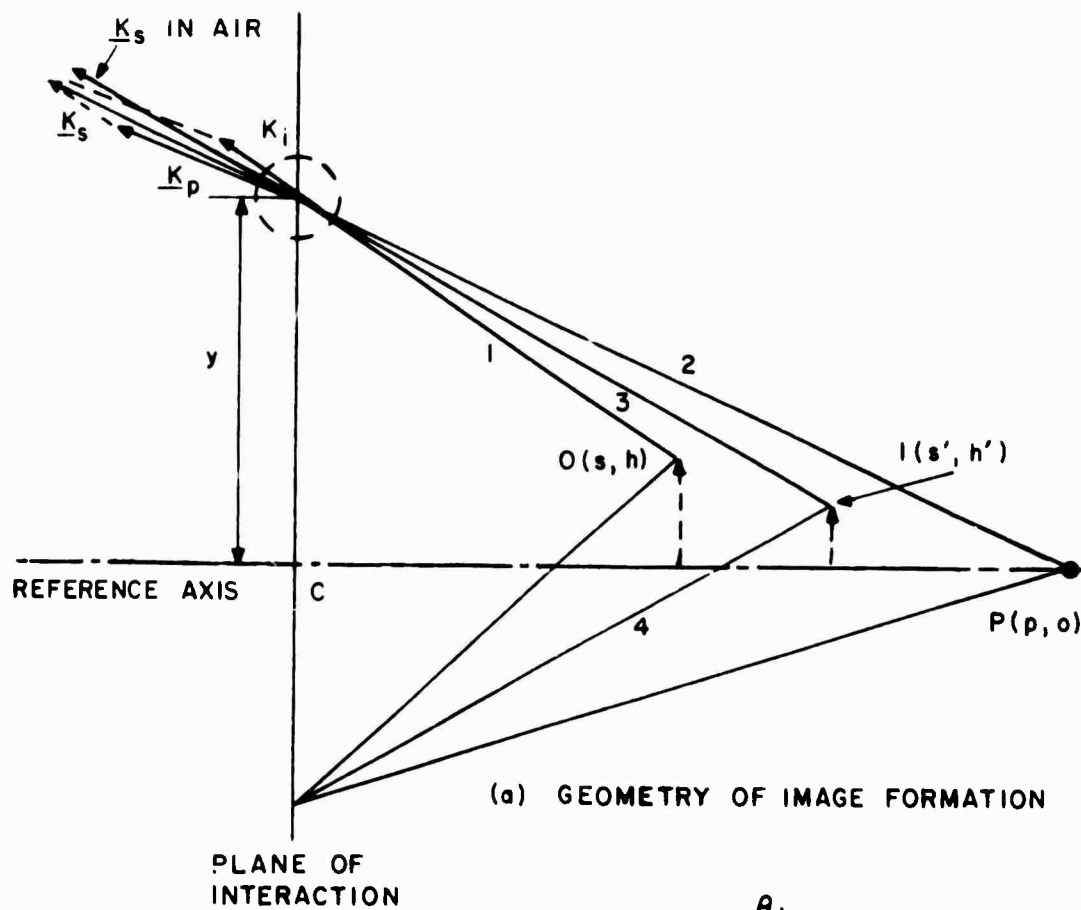
The primed angles are measured inside the nonlinear material, and the unprimed angles are measured in the air. The angles ψ' and α' are obtained from equations 1 and 2:

$$\begin{aligned}\alpha' &= \frac{\alpha}{n_i} + \theta_p \left(\frac{1}{n_i} - \frac{1}{n_p} \right) \\ \psi' &= \beta \left[\frac{\alpha}{n_i} + \theta_p \left(\frac{1}{n_i} - \frac{1}{n_p} \right) \right]\end{aligned}\tag{3}$$

The direction of the sum-frequency wave exiting from the infinitesimally thin nonlinear material is then by Snell's law:

$$\theta_s = n_s \theta'_s = (\theta'_p + \psi') n_s\tag{4}$$

Figure 2a shows the geometry of upconverter image formation. The point IR object is located at (s, h) , the point pump source is located at (p, o) , and the sum-frequency image is formed at (s', h') . IR ray 1 makes an angle θ_i and pump ray 2 makes an angle θ_p with the reference axis; they interact at the



$$\theta'_i = \frac{\theta_i}{n_i}$$

$$\theta'_p = \frac{\theta_p}{n_p}$$

$$\theta'_s = \frac{\theta_s}{n_s} = \theta'_p + \psi'$$

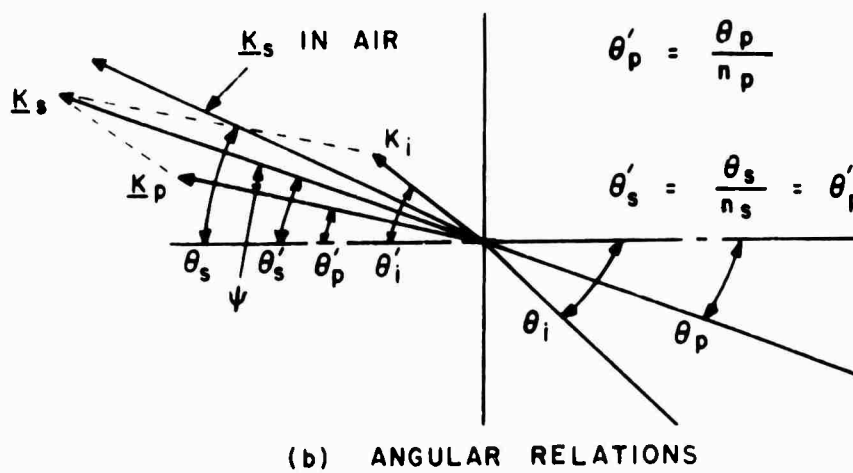


FIGURE 2. FORMATION OF IMAGE WITH INFINITESIMALLY THIN UPCONVERTER

material located distance y from the reference axis and generate sum-frequency ray 3. The direction of ray 3 is calculated from equation 4. The intersection of ray 3 with ray 4, which is generated at another point in the material, is the sum-frequency image and is located at (s', h') .

From the geometry of Figure 2a,

$$\begin{aligned}\frac{y - h'}{s'} &= \theta_s \\ \frac{y - h}{s} &= \theta_i\end{aligned}\tag{5}$$

and

$$\frac{y}{p} = \theta_p$$

Substituting equations 2, 3, and 4 into equation 5,

$$y \left[\frac{1}{-s'} + \frac{1}{s} \left(\frac{n_s}{n_i} \beta \right) + \frac{n_s}{n_p} \frac{1}{p} (1 - \beta) \right] + \left[\frac{h'}{s'} - \frac{h}{s} \frac{n_s}{n_i} \beta \right] = 0$$

This equation must hold for any y for the upconverter to form an image. Each quantity inside the brackets, therefore, must be equal to zero:

$$\frac{1}{s'n_s} - \frac{\beta}{sn_i} = \frac{1 - \beta}{n_p p}\tag{6}$$

$$\frac{h'}{h} = M_t = \beta \frac{n_s s'}{n_i s}\tag{7}$$

Equation 6 is the thin-lens formula for the image upconverter, and equation 7 gives the transverse magnification. Equations 6 and 7 and the geometry shown in Figure 2 are for a case of a real point pump source and a real object located in the right half-plane. Similar equations can be derived for

other arrangements. The phase-match condition, however, limits the number of arrangements that can be used for an image upconverter; it restricts the entrance angles θ_p and θ_i , and limits the angular aperture of an upconverter (as discussed in Section IV). For instance, most upconverters using presently available nonlinear crystals do not allow an arrangement in which a real pump source and a real object are located on opposite sides of the crystal.⁽¹⁵⁾ Equations 6 and 7 apply to the following cases, which permit upconversion to take place.

1. A real point pump source and a real IR object on the same side of the material (Figure 2). The image is virtual, erect, and on the same side as the object.
2. A real point pump source and a virtual object are on opposite sides of the material. The image can be either virtual or real.
3. A virtual point pump source and a real object are on opposite sides of the material. The image can be either virtual or real. This is a dual of case 2.
4. A virtual point pump source and a virtual object are on the same side of the material. The image is on the same side of the virtual object and real. This case is a dual of case 1.

A virtual point source represents a converging spherical wave, and a real point source represents a diverging spherical wave.

It is sometimes convenient to describe an optical system by a paraxial-ray transfer matrix. It relates the position y_1 and the slope (inclination) θ_1 of the ray in the input plane of the system to the position y_2 and the slope θ_2 of the ray in the exit plane of the system as follows:

$$\begin{bmatrix} y_2 \\ \theta_2 \end{bmatrix} = \begin{bmatrix} A & B \\ C & D \end{bmatrix} \begin{bmatrix} y_1 \\ \theta_1 \end{bmatrix} \quad (8)$$

If (y_1, θ_1) and (y_2, θ_2) are defined as the IR ray entrance position and slope, and the sum-frequency ray exit position and slope, respectively, an image upconverter by a ray transfer matrix can be described. From equations 3, 4, and 5, for an infinitesimally thin upconverter;

$$\begin{bmatrix} y_s \\ \theta_s \end{bmatrix} = \begin{bmatrix} 1 & 0 \\ \frac{n_s(1-\beta)}{n_p p} & \beta \frac{n_s}{n_i} \end{bmatrix} \begin{bmatrix} y_i \\ \theta_i \end{bmatrix} \quad (9)$$

The determinant of the ray matrix is clearly not unity, as expected from the nonreciprocity of the upconversion process. The propagation of paraxial rays through an image upconverter system containing optical components such as lenses and transmission media can now be obtained by multiplying the ray-transfer matrix of each optical element.

III. ABERRATIONS OF IMAGE UPCONVERTER WITH NONLINEAR MATERIAL OF FINITE THICKNESS

1. IMAGE FORMATION WITH THICK MATERIAL

The discussion of image formation by an infinitesimally thin image upconverter in Section II has furnished a relatively simple method of calculating the position and size of the image. In practice, the thickness of nonlinear material is neither infinitesimal nor infinite so that the effect of material thickness on image formation must be considered. The straight forward method of attacking this problem is to trace all rays interacting at different transverse planes inside the material.

All the assumptions made in Section II are considered to be valid throughout the discussion in this section.

Figure 3 illustrates the geometry of ray tracing. The object, image, and pump rays, which interact at transverse plane T, are traced using a procedure similar to that described in Section II. Transverse plane T is located at distance t from the center of material C, which is taken as the origin of the coordinate system. The pump, object, and image are located, respectively, at (p, o) , (s, h) , and (s', h') . The points O' and P' are, respectively, the object and pump locations, corrected for refraction at the material surface. The points O' , N , and L are on a straight line representing an object ray inside the material and making angle θ_i' with respect to the reference axis X. The straight line $P'ML$ is an equivalent pump ray. The straight line LNO' is an image ray, making an angle θ_i' with the X-axis, inside the material. The straight line KI , making an angle θ_s with the X-axis, is an image ray in air.

The following relationships are obtained by geometry:

From $\Delta O'AL$,

$$\theta_i' = \frac{AL}{O'A} = \frac{BL - h}{O'A} \quad (10)$$

From $\Delta P'BL$,

$$\theta_p' = \frac{BL}{P'B} \quad (11)$$

From ΔOGN ,

$$\theta_i = \frac{GN}{OG} = \frac{NF - h}{s - \frac{D}{2}} \quad (12)$$

From ΔPMF ,

$$\theta_p = \frac{FM}{PF} = \frac{FM}{p - \frac{D}{2}} \quad (13)$$

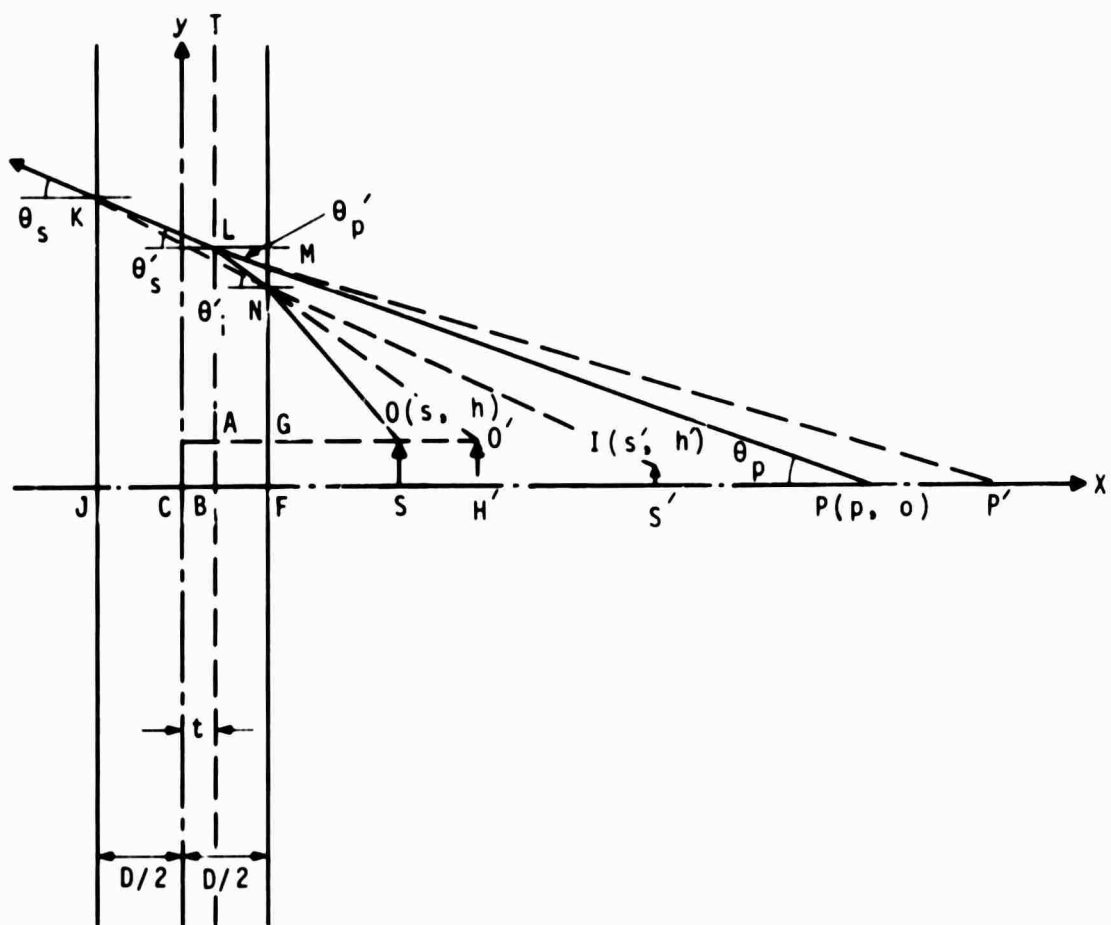


FIGURE 3. IMAGE FORMATION FOR PARAMETRIC UPCONVERTER WITH FINITE THICKNESS NONLINEAR MATERIAL

From $\Delta O'GN$,

$$\theta_i' = \frac{GN}{O'G} = \frac{FN - h}{O'A - \left(\frac{D}{2} - t\right)} \quad (14)$$

From $\Delta P'MF$,

$$\theta_p' = \frac{FM}{P'F} = \frac{FM}{P'B - \left(\frac{D}{2} - t\right)} \quad (15)$$

Using Snell's law and equations 10, 12, and 14,

$$\theta_i' = \frac{BL - h}{\left(s - \frac{D}{2}\right) n_i + \left(\frac{D}{2} - t\right)} \quad (16)$$

Similarly, from equations 11, 13, 15, and Snell's law,

$$\theta_p' = \frac{BL}{\left(p - \frac{D}{2}\right) n_p + \left(\frac{D}{2} - t\right)} \quad (17)$$

By geometry,

$$y_s = KJ = LB + \theta_s' \left(\frac{D}{2} + t\right) \quad (18)$$

and

$$\theta_s = \frac{KJ - h'}{s' + \frac{D}{2}} = n_s \theta_s' \quad (19)$$

Substituting the relationship

$$\theta_s' = \theta_p' (1 - \beta) + \beta \theta_i' \quad (20)$$

obtained from the phase-matching condition and after rearranging equations 18 and 19,

$$y \left[\frac{1}{(s' + D/2)} \left(1 + \frac{(D/2 + t)(1 - \beta)}{n_p(p - D/2) + (D/2 - t)} + \frac{(D/2 + t)\beta}{n_i(s - D/2) + (D/2 - t)} \right) - \frac{n_s(1 - \beta)}{n_p(p - D/2) + (D/2 - t)} - \frac{n_s\beta}{n_i(s - D/2) + (D/2 - t)} \right] - \left[\frac{h'}{s' + D/2} - \frac{\beta h}{(s - D/2)n_i + (D/2 - t)} \left(n_s - \frac{D/2 + t}{s' + D/2} \right) \right] = 0 \quad (21)$$

where $y = BL$

Since equation 21 must hold for every y and h for image formation, each member within the braces $\{ \}$ must be separately equal to zero. Equations expressing the image generated at a transverse plane T are then given by:

$$\frac{1}{(s' + \frac{D}{2})n_s - (\frac{D}{2} + t)} - \frac{\beta}{n_i(s - \frac{D}{2}) + (\frac{D}{2} - t)} = \frac{1 - \beta}{n_p(p - \frac{D}{2}) + (\frac{D}{2} - t)} \quad (22)$$

and

$$h' = h \frac{\beta \left[n_s \left(s' + \frac{D}{2} \right) - \left(\frac{D}{2} + t \right) \right]}{n_i \left(s - \frac{D}{2} \right) + \left(\frac{D}{2} - t \right)} \quad (23)$$

The image location (s', h') is, as expected, a function of both D and t . The images generated at the different transverse planes of a single object are formed at different locations. The dependence of the image position s' upon t leads to a blurring of the image. This effect is analogous to lens spherical aberration but is peculiar to the image upconverter. The thickness aberration is due to the finite thickness of the material, whereas, lens spherical aberration is due to the obliquity of nonparaxial rays.

Spherical aberration would be added to the thickness aberration if exact-ray tracing is used rather than paraxial-ray tracing. Other monochromatic aberrations (such as coma, astigmatism, curvature of field, and distortion) would have to be considered if higher-order theory were used for the analysis.

Equations 22 and 23 have been derived for a case where both the pump source and the object are located outside the nonlinear material. If a pump source, either real or virtual, is located inside the material, equations 22 and 23 are modified by equating pump refractive index n_p to unity. A similar modification, $n_i = 1$, should be made for the case where an IR object is inside the material. The modification is necessary for this case because the refraction of the pump and object rays at the front surface of the crystal does not affect the imaging process. The refraction of the sum-frequency rays, however, must be taken into account regardless of the pump and the object locations, because the image will be observed in air rather than inside the nonlinear material. The existence of chromatic aberration is evident from the dispersion of the material. Chromatic aberration exists even in an infinitesimally thin image upconverter. Since chromatic aberration is not peculiar to the image upconverter, even though it may differ somewhat from lens chromatic aberration, it will not be considered further.

2. PLANE-WAVE IR BEAM

Plane-wave IR beam incidence parallel to the reference axis can be presented by equating the object distance s to infinity. The sum-frequency image position is then given by:

$$s' = \frac{n_p \left(p - \frac{D}{2} \right) + \left(\frac{D}{2} - t \right) + (1 - \beta) \left(\frac{D}{2} + t \right)}{n_s (1 - \beta)} - \frac{D}{2} \quad (24)$$

The sum-frequency wave focal points, generated at the front and back surfaces of the material, are obtained by equating t to $\frac{D}{2}$ and $-\frac{D}{2}$, respectively:

$$s_f' = \frac{n_p \left(p - \frac{D}{2} \right)}{n_s (1 - \beta)} + D \left(\frac{1}{n_s} - \frac{1}{2} \right) \quad \text{for } t = \frac{D}{2} \quad (25)$$

and

$$s_b' = \frac{n_p \left(p - \frac{D}{2} \right)}{n_s (1 - \beta)} + D \left[\frac{1}{n_s (1 - \beta)} - \frac{1}{2} \right] \quad \text{for } t = -\frac{D}{2} \quad (26)$$

The longitudinal-thickness aberration, defined as the difference between these two focal points, is then:

$$\Delta s' = |s_b' - s_f'| = \left| \frac{D\beta}{n_s (1 - \beta)} \right| \quad (27)$$

The longitudinal-thickness aberration for plane-wave IR beams depends only on the material properties, but not upon the pump position. The lateral-thickness aberration is given by:

$$\Delta y' = \Delta s' \tan \theta_{s \max} \quad (28)$$

where $\theta_{s \max}$ is the maximum angle that the sum-frequency ray makes with the reference axis.

3. PLANE-WAVE PUMP BEAM

Plane-wave pump-beam incidence, normal to the material is considered next. For this case, the pump distance p becomes infinite and the image is located at:

$$s' = \frac{1}{n_s \beta} \left[n_i \left(s - \frac{D}{2} \right) + \left(\frac{D}{2} - t \right) + \beta \left(\frac{D}{2} + t \right) \right] - \frac{D}{2} \quad (29)$$

The longitudinal-thickness aberration becomes

$$\Delta s' = |s_b' - s_f'| = \left| D \frac{1 - \beta}{n_s \beta} \right| \quad (30)$$

It is independent of the IR object location. The longitudinal-thickness aberrations of the plane-wave IR beam and the plane-wave pump beam are related by

$$\frac{(\Delta s')_{s = \infty}}{(\Delta s')_{p = \infty}} = -\frac{\beta^2}{(1 - \beta)^2} \quad (31)$$

Since β is usually less than unity for image upconversion, the longitudinal-thickness aberration is smaller for the parallel-object-ray case than for the parallel-pump-beam case.

The lateral-thickness aberration is given also by equation 28.

4. PUMP SOURCE AND IR OBJECT IN SAME TRANSVERSE PLANE

The image position is given by equations 22 and 23, using the relationship $s = p$. Since both s' and h' are functions of t , the blurring of the image could not be avoided. Because Firester⁽¹⁴⁾ ignored refraction, he concluded that resolution for this optical arrangement was unlimited. The non-zero aberration is due to dispersion of the material. Indeed, s' will be independent of t if the material is nondispersive. However, h' is still dependent on the object position. If $p = s$ and $n_s = n_p = n_i$, in equation 22 and 23, then

$$s' = p + D \left(\frac{1}{n} - 1 \right) \quad (32)$$

$$h' = h\beta \quad (33)$$

Since s' is independent of t , the longitudinal-thickness aberration does not exist; also the transverse image spread defined by $\Delta h' = |h'_f - h'_b|$ becomes

$$\Delta h' = 0 \quad (34)$$

Above result indicates that the obliquity of the IR object ray would not cause image blurring if the crystal dispersion can be neglected. Image blurring $\Delta h'$ of a dispersive crystal due to the object ray obliquity is, however, not zero in general. This effect resembles the coma of an ordinary lens. This effect is called thickness coma since it is due to the finite thickness of the material, but it is not caused by violation of paraxial approximation as in the case of an ordinary lens.

The longitudinal-thickness aberration, $\Delta s'$, of a dispersive material for the case $s = p$, is generally not zero but is minimum.

5. PARALLEL-PUMP AND PARALLEL-OBJECT RAYS

Pump and object rays can be made parallel to the axis with a suitable lens arrangement. Since both s and p are equal to infinity, the image will be formed at infinity. Thickness aberration and thickness coma should disappear for this case. This arrangement represents upconversion in Fourier space and is an aberration-free image system. The resolution for this arrangement is limited by higher-order effects discussed later.

6. PUMP AND OBJECT AT CENTER OF MATERIAL

Pump and object can be positioned at the center of the material with a suitable optical system. The pump and object distances are zero for

this case. The refractive indices n_p and n_i are equal to unity because the pump and the object are inside the material.

The image locations s' and h' are given by

$$s' = \frac{D}{2} \left(\frac{1}{n_s} - 1 \right) \quad (35)$$

$$\frac{h'}{h} = \beta \quad (36)$$

Both the longitudinal thickness aberration and the thickness coma are zero as is evident from Equations (35) and (36).

7. COMPUTED VALUES OF ABERRATION AND COMA FOR SPECIFIC CASES

Consider, next, a specific upconverter configuration using a proustite (Ag_3AsS_3) crystal, pumped by an Nd : YAG laser ($1.06 \mu\text{m}$), and a signal from a CO_2 laser ($10.6 \mu\text{m}$). For this typical values of thickness aberration and coma have been computed.

Figure 4 shows the longitudinal aberration that occurs due to the longitudinal thickness of the nonlinear crystal material. Longitudinal aberration takes the image of a point and elongates it along the optical axis of the upconverter system. The values of pump position (p), object position (s), and aberration ($\Delta s'$) have been normalized with respect to the thickness (D), of the crystal material. Each curve corresponds to a different value of normalized pump position (p/D) with respect to the region of nonlinear interaction. When the apparent object distance (s/D) is equal to the apparent pump distance, that is, the spatial wavefronts are matched, the longitudinal-thickness aberration becomes a minimum. Other requirements permitting upconverter operation should be set at this value.

As the pump distance goes to infinity ($p/D = \infty$), that is, the pump wave becomes a plane wave, the normalized aberration achieves a fixed value of 3.9. If both the object distance and the pump distance are infinite, the case covered in Section III-5, the aberration becomes zero.

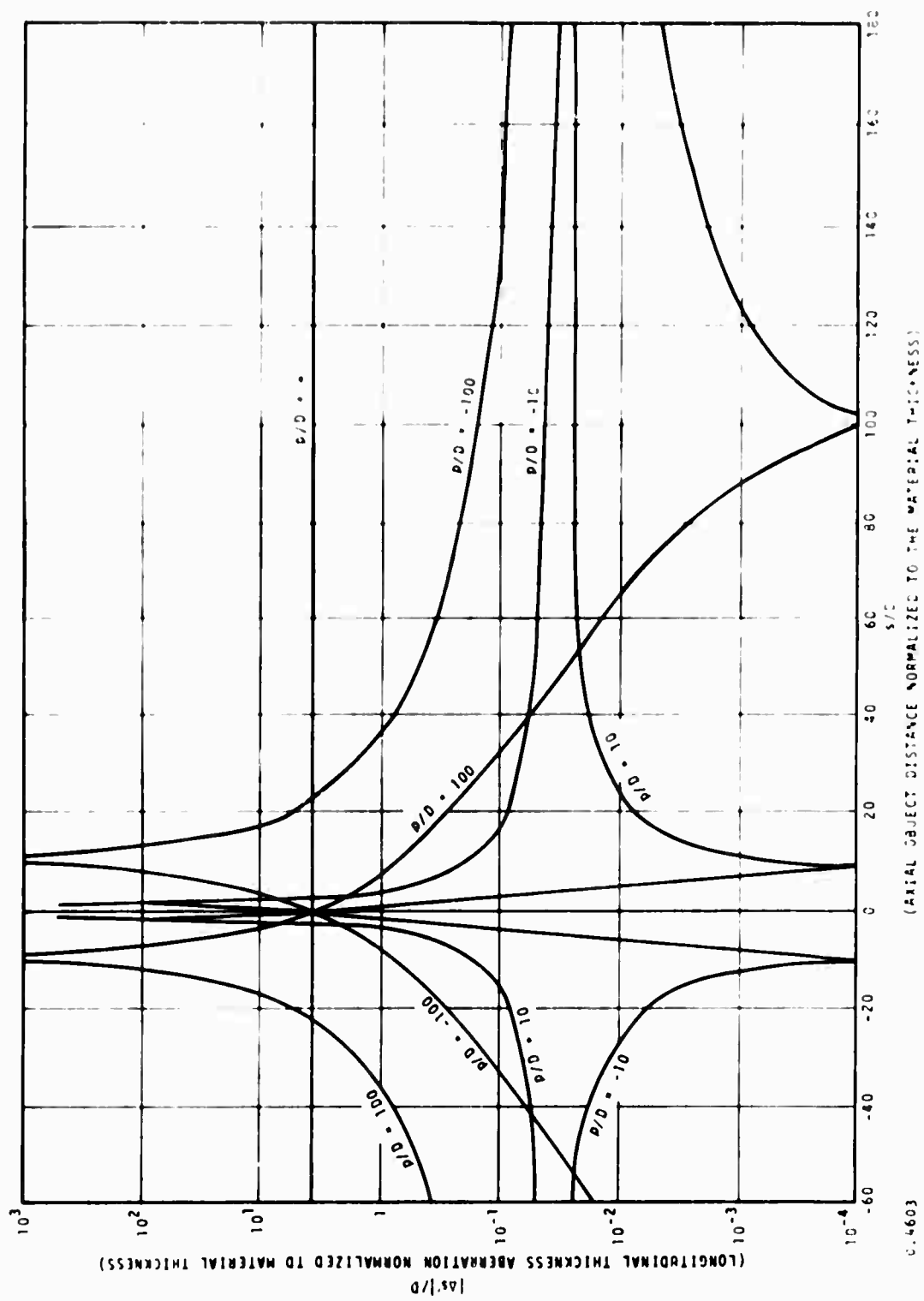
Figure 5 shows the thickness coma values computed for a fixed pump position. This curve is representative of a family of such curves and indicates a decrease in coma as the curvature of the signal wavefront is decreased. For small values of off-axis displacement (h), the values of coma will generally be very small for large values ($|s/D| > 10$) of object distance.

IV. EXTENDED PUMP SOURCE, ANGULAR APERATURE, AND RESOLUTION

Degradation of image quality due to an extended pump source, as well as the angular aperture of a parametric image upconverter, are considered in this section. Formulae for resolution calculation are also presented.

1. EXTENDED PUMP SOURCE

In general, a pump source used for an image upconverter is a laser. A pump laser can be operated either in a single-transverse mode or in a multitransverse mode. The pump wavefront of a single-mode laser beam will always be a single-spherical wave or near-plane wave. The assumption of a point-source pump with a spherical wavefront used in the preceding sections therefore applies to this case. A multitransverse mode laser beam can be considered as a composite of many spherical wavefronts. The pump source can then be considered as an extended source of finite size. The pump radiation at each point in the material will be represented by wave vectors with a range of directions equal to the divergence of the



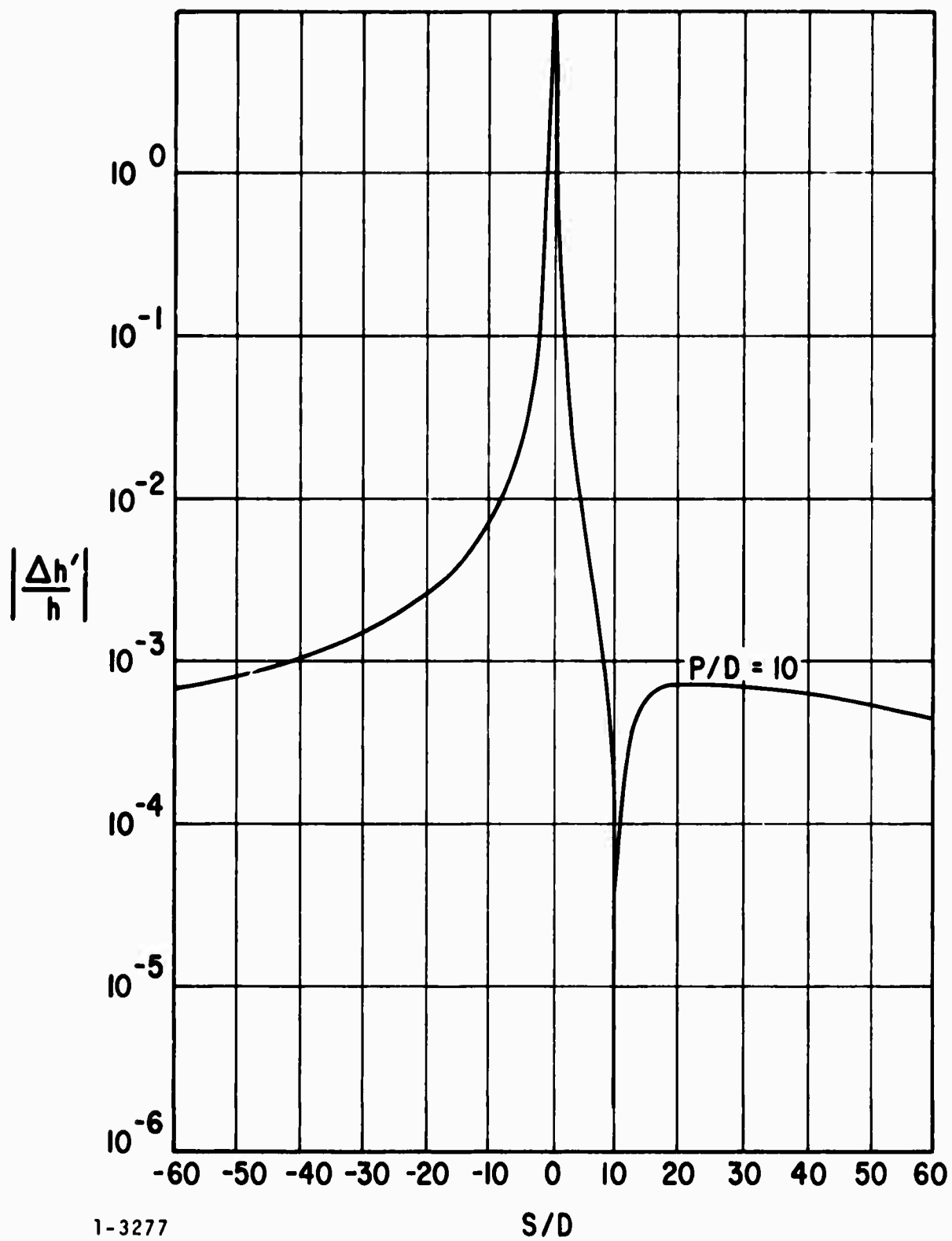


FIGURE 5. THICKNESS COMA OF AN IMAGE UPCONVERTER AS A FUNCTION OF AXIAL OBJECT DISTANCE

pump beam. The size of an extended pump source is related to the divergence angle δ , for a small-angle approximation, by

$$a = p\delta \quad (37)$$

where

a = equivalent pump size

δ = pump divergence angle

The divergence of the pump waves will cause a divergence in the sum-frequency waves for a fixed object-wave vector. The same sum-frequency divergence could be caused by an equivalent object divergence if the pump divergence δ is made zero. The equivalent object divergence ϵ that would give the same sum-frequency divergence as the pump divergence can be obtained from the angular relationship

$$\theta_s = \frac{n_s}{n_p} (1 - \beta) \theta_p + \frac{n_s}{n_i} \beta \theta_i \quad (38)$$

The change in θ_s due to the change in θ_p , keeping θ_i constant is

$$\frac{\partial \theta_s}{\partial \theta_p} \Delta \theta_i = 0 = \frac{n_s}{n_p} (1 - \beta) \quad (39)$$

Similarly

$$\frac{\partial \theta_s}{\partial \theta_i} \Delta \theta_p = 0 = \frac{n_s}{n_i} \beta \quad (40)$$

The equivalent object divergence ϵ is then obtained by equating equations 39 and 40:

$$\epsilon = \frac{n_i}{n_p} \frac{1 - \beta}{\beta} \delta \quad (41)$$

An image upconverter with a point object and an extended-pump source can now be represented by an equivalent system consisting of a point pump source and a finite object. The angular resolution of an upconverter with a multitransverse-mode laser pump is therefore limited by the angle ϵ .

2. ANGULAR APERTURE

To be useful, an image system should have a reasonably wide field of view. The principal factor that restricts the field of view of a parametric image upconverter is the phase-matching condition.

For crystal of length D , phase-matched upconversion takes place as long as $|\Delta \underline{K}| = |\underline{K}_s - \underline{K}_p - \underline{K}_i| \leq \frac{2\pi}{D}$, where $\Delta \underline{K}$ is assumed to be along the direction of \underline{K}_s for convenience, as shown in Figure 6. Three-dimensional phase matching instead of two-dimensional matching should be considered for an image converter if the anisotropy of the crystal is significant. Only the two-dimensional match, shown in Figure 4, is discussed.

The phase-match error ΔK is given by

$$\Delta K = K_s - (K_p + K_i \cos \alpha') \sec \psi' \quad (42)$$

where

$$\tan \psi' = \frac{K_i \sin \alpha'}{K_p + K_i \cos \alpha'} \quad (43)$$

The small-angle approximation $\sin x \approx x$ reduces equation 43 to the angular-demagnification relation. The previous sections assumed that

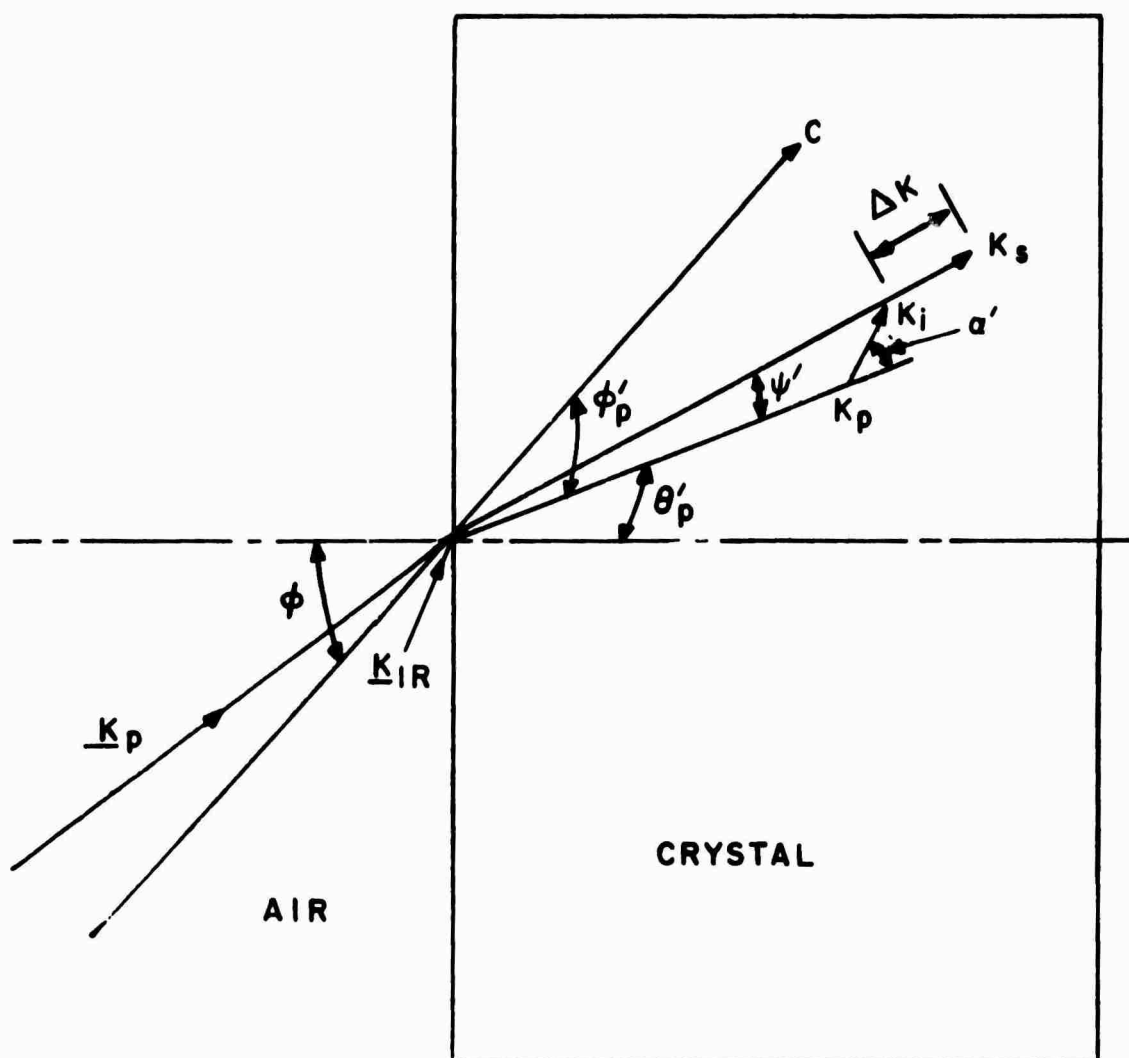


FIGURE 6. ANGULAR RELATIONS IN CRYSTALLOGRAPHIC COORDINATE SYSTEM

ΔK is negligibly small compared with the smallest K . Given the values of θ'_p , α' , and ϕ (the angle between the crystallographic C axis and the normal to the crystal surface), ΔK can be obtained using equations 42 and 43.

Figure 7 shows the numerical results, using refractive index data reported by Hobden⁽¹⁷⁾, for a 1-cm long Ag_3AsS_3 upconverter. The IR object and the pump wavelengths are $10.63 \mu\text{m}$ and $1.064 \mu\text{m}$, respectively; they are polarized, respectively, extraordinary and ordinary. The angles ϕ'_p and ϕ'_i are related to θ'_p and θ'_i , respectively, by:

$$\theta'_\ell = \phi - \theta'_\ell \quad (\ell = i \text{ or } p) \quad (44)$$

It has been shown that, in general, noncritical phase matching gives a larger field of view for the object field than other phase-matching arrangements.⁽¹⁸⁾

This is true only if nonmonotonical angular variations of sum-frequency output are not allowed. This situation is demonstrated in Figure 7 by the lines marked a, b, and d. The change in ΔK is monotonic when the IR object incident to angle θ'_i is monotonic along lines a, b, and d. Consequently, the angular sum-frequency output variation exhibits a single maximum where $|\Delta K|$ is minimum. It is clear from Figure 7 that line b has the largest object angular aperture. The field of view can be increased slightly if double maxima in the sum-frequency output angular variation is allowed. Line c in Figure 7 represents this case.

For a 1-cm long Ag_3AsS_3 image upconverter with a $10.6\text{-}\mu\text{m}$ object and a $1.06\text{-}\mu\text{m}$ pump, the maximum angular aperture lies within the shaded area of Figure 7. The allowable maximum $|\Delta K|$ is chosen to be 2π for convenience; the sum-frequency output is zero at this value of ΔK . Figure 8 shows the field of view of a 1-cm long Ag_3AsS_3 image upconverter.

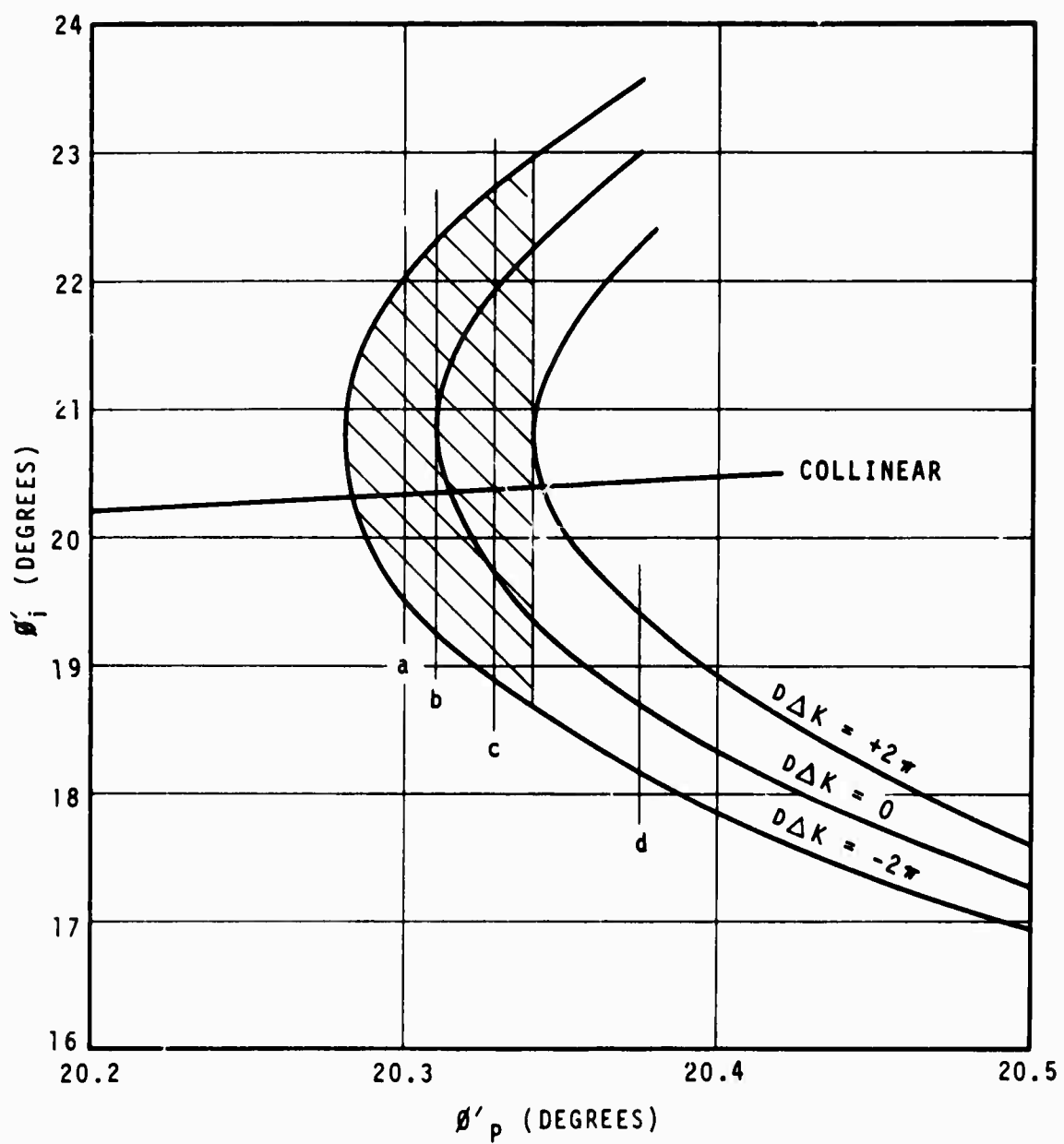


FIGURE 7. PHASE-MATCH ANGLES FOR Ag_3AsS_3 10.6 TO 0.96 μm UPCONVERSION

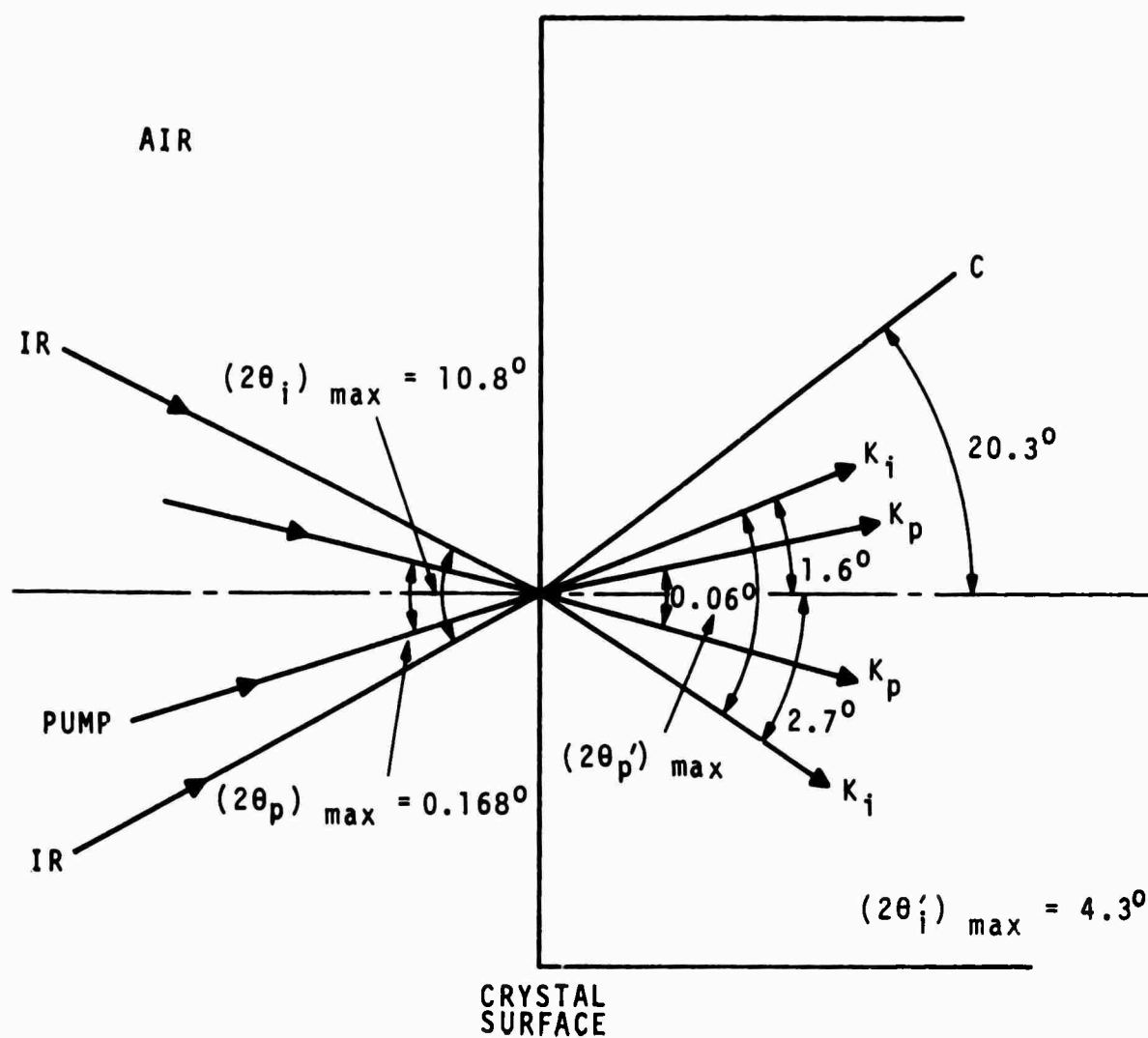


FIGURE 8. CRYSTAL ORIENTATION AND ANGULAR APERTURE FOR Ag_3AsS_3 10.6 TO 0.96 μm IMAGE UPCONVERTER

The crystal should be cut so that the optical axis makes an angle of 20.3 degrees with the normal to the surface. The angular aperture of other non-linear materials suitable for image upconversion has been shown to be less than a few hundred milliradians.⁽¹⁵⁾ Therefore, the paraxial assumption used in the preceding discussion of angular aperture is shown to be valid.

3. RESOLUTION

The resolution of an image upconverter can be calculated if the aberrations and the angular aperture of the system are known. Only the point pump source is considered here. The modification to an extended pump source is straightforward since its affect on the object field is known.

Figure 9 shows the image of a point IR object located at (s, h) ; the pump is located at (p, o) . The image is a line connecting points I_f and I_b , which are, respectively, the images generated at the front and the back surfaces of the material. Images generated on a transverse plane located between these extreme surfaces lie along the $I_f I_b$. Because of thickness aberration, the lateral aberration is not zero; also, the thickness coma produces the transverse spread $\Delta h'$. The transverse dimension of the image is the sum of these two aberrations:

$$H' = \Delta h' + \Delta s' \theta_{s \max} = |h'_f - h'_b| + |s'_f - s'_b| \theta_{s \max} \quad (45)$$

Again, $\theta_{s \max}$ is the maximum angle that the sum-frequency ray makes with the reference axis.

To analyze the resolution of an image upconverter, consider the geometry of Figure 10. Two object points, located at (s, h_1) and (s, h_2) , are imaged into lines I_1 and I_2 . In order that these two images be resolvable, the point (s'_{f1}, h'_{f1}) and the point $(s'_{f2}, h'_{b2} - \Delta s' \theta_{s \max})$ should coincide.

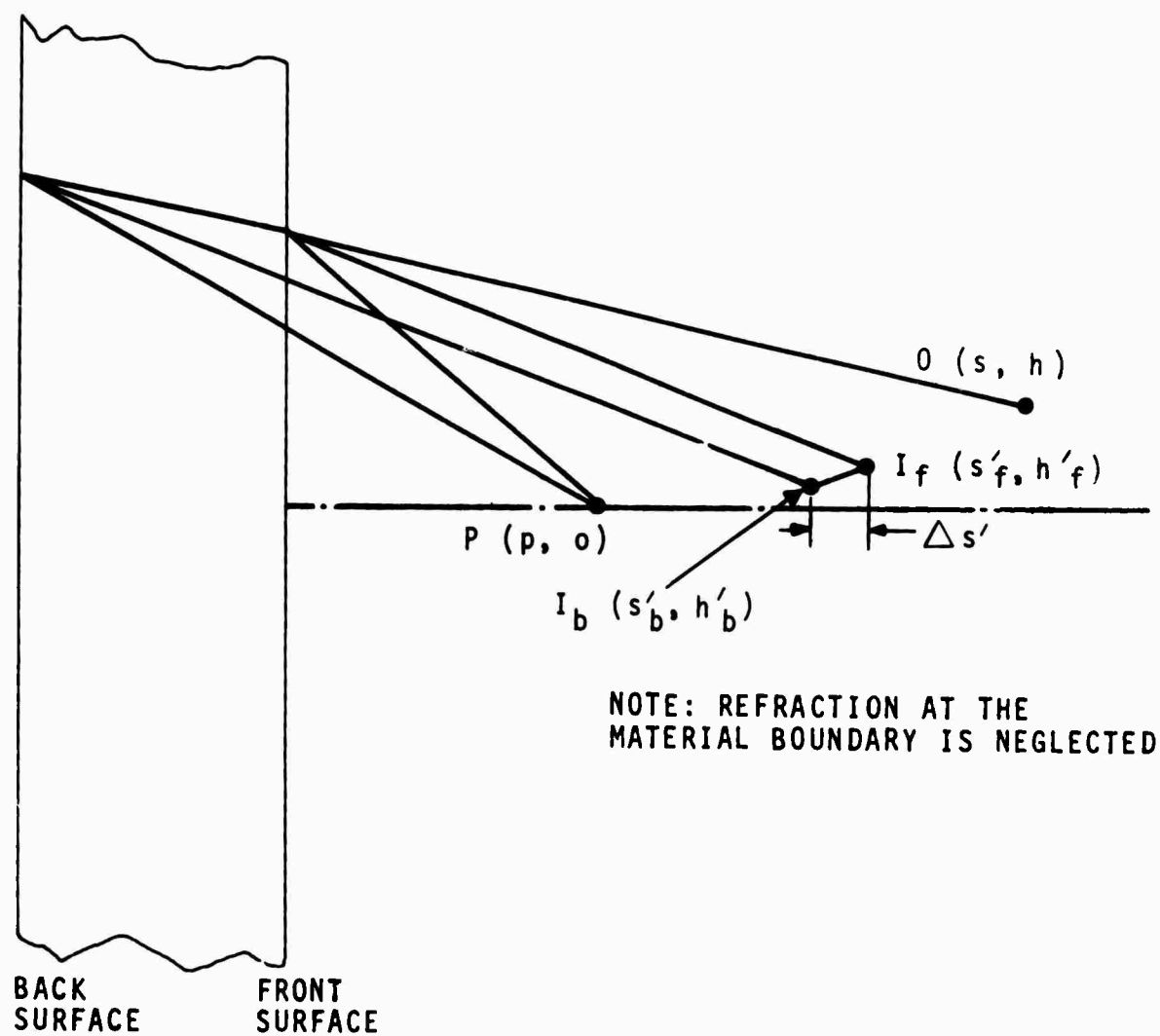


FIGURE 9. BLURRING OF SUM-FREQUENCY IMAGE DUE TO ABBERRATIONS OF PARAMETRIC UPCONVERTER

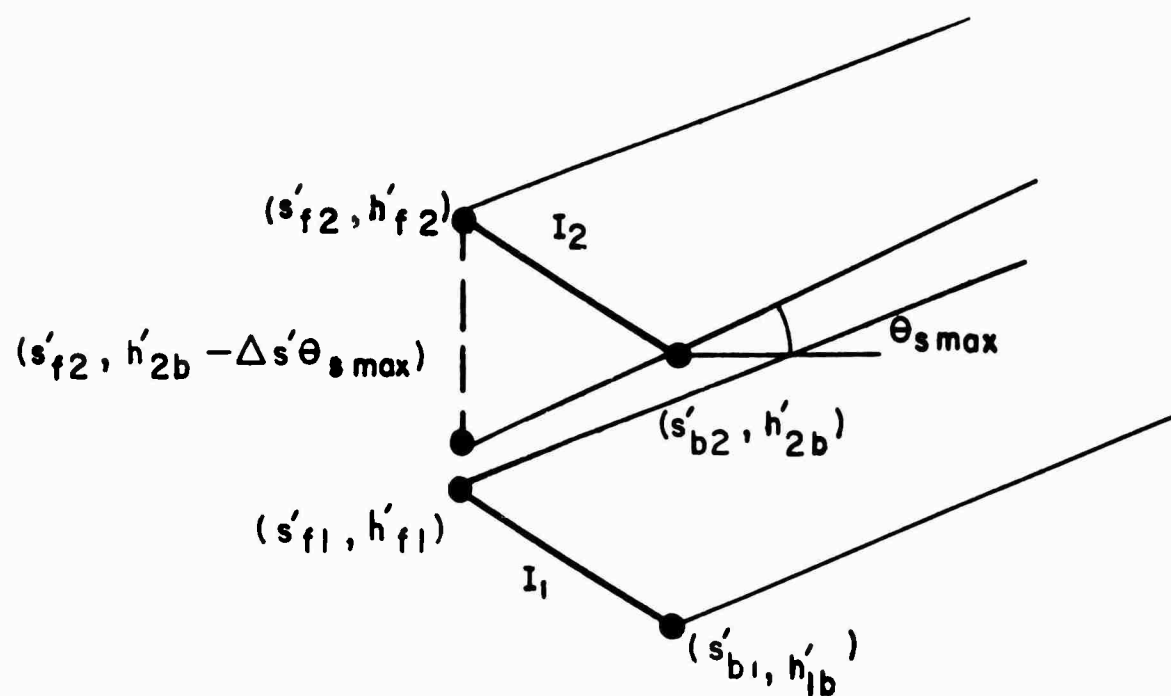


FIGURE 10. RESOLUTION CALCULATION

$$s'_{f1} - s'_{f2} \quad (46)$$

$$h'_{f1} = h'_{b2} - \Delta s' \theta_{s \max} \quad (47)$$

Equation 46 is automatically satisfied. The change in $\theta_{s \max}$ due to the difference in object transverse location is neglected. Using equation 23, equation 47 is rewritten as

$$h_1 M_{tf} = h_2 M_{tb} - \Delta s' \theta_{s \max} \quad (48)$$

The minimum resolvable transverse size of an object located at (s, h) becomes

$$\Delta h = h \left| \frac{M_{tf}}{M_{tb}} - 1 \right| + \frac{\Delta s'}{M_{tb}} \theta_{s \max} \quad (49)$$

The linear resolution of the object field about (s, h) is then given by

$$R = \frac{1}{\Delta h} \text{ elements/unit length} \quad (50)$$

The angular resolution, γ , which is more meaningful than the linear resolution for some optical systems, for a small-angle approximation is given by

$$\gamma = Rs/\Delta h \quad (51)$$

The resolution of a plane-wave pump case is now considered as an example. For this case, $p = \infty$, $\theta_p = 0$, and $\theta_{s \max} = \frac{n_s}{n_i} \beta \theta_{i \max}$ according to equation 20.

The minimum resolvable transverse size is equal to the lateral-thickness aberration, because $\Delta h'$ is zero in this case:

$$(\Delta h)_{p=\infty} = D \frac{1 - \beta}{n_i} \theta_{i \max} \quad (52)$$

The linear resolution, given by

$$R_p = \infty = \frac{n_i}{D(1 - \beta) \theta_{i \max}} \quad (53)$$

is independent of the object location.

V. OTHER FACTORS AFFECTING IMAGE FORMATION OF IMAGE UPCONVERTER

A nonlinear crystal used for upconversion must be anisotropic for parametric interaction to take place. The electro-optic tensor, which is responsible for the generation of nonlinear polarization in the material, is nonzero if the crystal does not possess a center of symmetry. Anisotropy and dispersion are also required for phase match. The treatment presented in the preceding sections does not include the effect of anisotropy. The effect of dispersion was partially accounted for by using different indices of refraction for different wavelengths.

The first effect of anisotropy is due to the angular change of the index of refraction of the extraordinary wave. This change also affects the angular demagnification factor, since it is a ratio of the IR wave vector to the sum-frequency wave vector. The image of a point object generated even by an infinitesimally thin material will not be a point if the angular change of the index of refraction is included.

The second effect of anisotropy is due to double refraction. The wave vector normal to the wavefront and the Poynting vector are not in the same direction in an anisotropic crystal. The analysis given in the preceding sections is not rigorous ray tracing because of double refraction. The ray tracing inside the material should be done along the rays instead of along the wave vectors. Snell's law should be used for rays instead of for the

wavefront, and the angular demagnification factor should be modified for ray angles. Also, the effective interaction thickness of the upconverter will be different from the material physical thickness if double refraction is considered.

Another effect of dispersion is variation of the angular demagnification factor with wavelength. The natural consequence of dispersion is chromatic aberration, which is important if the object spectrum or the pump spectrum is wide. Image degradation caused by chromatic aberration will not be severe for most of the presently available optical upconverters because of narrow infrared spectral bandwidths, typically in order of 10^{-1} cm. It, however, may become predominant for a large bandwidth upconverter, such as the one reported by Midwinter. ⁽¹⁹⁾

Another factor affecting the image formation is the three-dimensional effect. The ray-tracing analysis presented in previous sections is carried out in two dimensions. The reference axis normal to the crystal surface from the point pump is not a symmetry axis. This means that a parametric image upconverter is not circular symmetric. The angular demagnification factor and the refractive indices depend on the transverse coordinates (x, y) (not the same as the crystallographic coordinates), where the interaction takes place. This is a three-dimensional generalization of the double-refraction effect previously discussed. If the nonlinear crystal was oriented so that the crystallographic C axis (optic axis) is normal to the entrance and exit surface, and the angular aperture was spread almost evenly about the C axis, the image upconverter would be circular symmetric. However, the requirement for phase matching and maximum light transmission necessitate crystal cuts that do not permit circular symmetry. A

three-dimensional field of view is therefore not a circular cone. The lack of symmetry introduces distortion of the upconverted image. A practical image upconverter, therefore, must not use highly anisotropic material for high-quality imaging.

The discussion of angular aperture presented in Section IV applies to a spherical pump beam; that is, the pump intensity remains constant over the wavefront. In practice, however, the pump beam is near Gaussian; its intensity decreases with the distance from the beam axis. The brightness of the image of a finite object decreases accordingly with the transverse distance from the reference axis. This means that the image does not have clear definition at its edge. The fading of the image also implies the reduction in the field of view of an imaging system. The fading of the image occurs even along the reference axis, where it is well within the field of view of the object field. The resolution calculation becomes ambiguous with a Gaussian pump beam.

VI. CONCLUSION

Formation of a sum-frequency image by means of parametric upconversion has been analyzed for general pump and object configurations by applying the ray-tracing method. A formula relating the image location to the object and the pump locations has been derived. A geometric optics theory of aberrations for parametric image upconversion has been described. The aberrations are due to the finite thickness of the nonlinear material. This phenomenon is peculiar to the parametric image-upconversion process. Aberrations due to the finite thickness of the material vanish when both the pump and the object waves are parallel-plane waves. The longitudinal aberration is minimum when the pump and the object are located on the

same transverse plane. The limiting resolution of an image upconverter can be calculated when the aberrations for the particular image upconverter are known. A method for calculating the resolution has been described.

The primary factor that limits the field of view of a parametric image upconverter is the phase-match condition. Other factors, such as dispersion, anisotropy, and nonparaxial rays degrade the image, but are second-order effects.

same transverse plane. The limiting resolution of an image upconverter can be calculated when the aberrations for the particular image upconverter are known. A method for calculating the resolution has been described.

The primary factor that limits the field of view of a parametric image upconverter is the phase-match condition. Other factors, such as dispersion, anisotropy, and nonparaxial rays degrade the image, but are second-order effects.

CHAPTER 3 PHYSICAL OPTICS THEORY OF PARAMETRIC IMAGE UPCONVERSION

I. INTRODUCTION

Imaging theory of parametric image upconversion was treated by the geometric optics approach in preceding chapter. An equation relating locations of object, pump, and image was derived and the existence of image aberrations due to the finiteness of the nonlinear material thickness was made clear. In geometric optics treatment of parametric image upconversion, some higher order factors that would affect imaging properties were neglected. It was considered also in the geometric optics theory that upconverted image is formed by constructive interference between the waves radiated from each differential slab of polarization in the material. This concept lead to thickness aberration of the image upconversion. To verify the concept of constructive interference and to understand the higher order effects; such as, anisotropy, phase-mismatch, and finite interaction aperture, the problem must be treated in the formalism of physical optics. It is the purpose of this chapter to treat the problem in the framework of wave theory. The problem considered here is to determine the nature of the image field arising from a dielectric polarization generated at the sum-frequency by interaction of the object field and the pump field in the nonlinear material. The imaging properties of the parametric image upconversion has been treated by Firester⁽¹³⁾ in the formalism of Fourier optics⁽²²⁾ that resembles closely to the treatment of linearly-invariant filter system. The advantage of such an approach is that the process of upconversion of the complex non planar objects field to the complex non planar image field can be studied by investigating the interaction of planar angular spectrum components in the nonlinear material.

The results obtained by Fourier optics treatment describe more quantitatively the imaging properties of upconversion process and can be tied directly to the formalism of optical transfer function description of an imaging system.

General formulation of image upconversion process taking into account of phase-mismatch and the crystal anisotropy is presented in Section II. The treatment presented follows Kleiman⁽²³⁾ closely and is more rigorous than Firester⁽¹³⁾. The basic equations that describe the angular spectrum of image field in terms of object and pump angular spectrum are obtained. The concept of constructive interference of radiation from differential slabs is also verified in Section II. Imaging properties, such as angular spectrum of image field, image position, and the point spread function of several image upconversion systems, namely i) planar wave pump system, ii) spherical wave pump system, and iii) Gaussian wave pump system are considered in Sec. III. The results obtained agree with the geometric optics results. The effect of finite interaction aperture on upconverted images is also discussed in Sec. III. The effective interaction aperture at the sum-frequency is smaller than the aperture at pump and/or object frequencies.

II. GENERAL FORMULATION

1. Basic Equations

Mathematically, the formulation is based upon Maxwell's equation for a lossless anisotropic medium free of charges and currents but containing a prescribed source in the dielectric polarization. All linear induced polarization is assumed to be included in the dielectric constant tensor. The analysis follows very closely to Kleiman's treatment^(23, 24) of second

harmonic generation except that the analysis will be carried out in Fourier spatial frequency space rather than in spatial coordinate space. It is shown in Appendix A that the Fourier decomposed angular spectrum of the field disturbance can be considered as plane waves propagating in different directions. Parametric interaction of complex (non planar) waves in the nonlinear material can be understood by studying the interaction of their angular spectrum components. The Fourier optics formalism puts the problem in the framework of linear transverse-spatial invariant system.

The theory of parametric upconversion involving three plane waves has been treated in considerable detail^(1, 10, 25). Under matching conditions the plane wave signal field $E_i(z)$ and the output plane wave sum-frequency field $E_s(z)$ satisfy the relations⁽¹⁾.

$$E_s(z) = \left(\frac{\omega_s}{\omega_i} \right)^{1/2} E_i(0) \sin\left(\frac{\pi z}{\ell}\right) \quad (54)$$

and

$$E_i(z) = E_i(0) \cos\left(\frac{\pi z}{\ell}\right) \quad (55)$$

where the characteristic length ℓ for power conversion

$$\ell^{-1} = \frac{2\omega_i \omega_s d}{C^2(K_i K_s)^{1/2}} E_p(0) \quad (56)$$

with K the wave number, ω the angular temporal frequency, d the appropriate component of the second-order polarization tensor, and $E_p(0)$ the pump electric field at input surface of the nonlinear material. In the limit $z \ll \ell$, the sum-frequency field is given by⁽¹⁾,

$$E_s(z) \approx 2\pi d \left(\frac{1}{n_s n_i} \right)^{1/2} \frac{\omega_s}{C} E_i(0) E_p(0) z \quad (57)$$

As shown by Kleinman⁽²³⁾, the linear growth of $E_s(z)$ is ascribed to constructive interference between a forced wave generated by the polarization and a free wave generated at the surface by the forced wave. It is equally valid, as we shall see later, to ascribe the growth to constructive interference between the waves radiated from each differential slab of polarization in the material. We developed geometric optics theory according to latter view. Eq. (57) is the solution for the matching case satisfying $E_s(0) = 0$. Actually Eq. (57) does not give the correct sum-frequency field. The value of $E_s(0)$ is related to the amplitude of nongrowing waves in the medium and a reflected wave at the surface^(23, 10, 26). These waves are, however, many order of magnitude weaker than the growing wave.

The rigorous analysis of upconversion process is based upon the inhomogeneous vector wave equation^(10, 23, 24).

$$\nabla \times \nabla \times \underline{E}_s(\underline{r}) - \left(\frac{\omega_s}{C} \right)^2 \underline{\epsilon} : \underline{E}_s(\underline{r}) = 4\pi \left(\frac{\omega_s}{C} \right)^2 \underline{P}(\underline{r}) \quad (58)$$

where $\underline{\epsilon} = \underline{I} + 4\pi \underline{\chi}^{(1)}$ ($\underline{\chi}^{(1)}$ is the linear susceptibility tensor) and \underline{E}_s are respectively dielectric constant tensor and electric field at the frequency $\omega_s = \omega_i + \omega_p$. The plane polarization wave $\underline{P}(\underline{r}, t)$ is related to the signal electric field $\underline{E}_i(\underline{r})$ and pump field $\underline{E}_p(\underline{r})$ by the relation

$$\underline{P}(\underline{r}, t) = \underline{P}(\underline{r}) e^{-i\omega_s t} = \underline{d} : \underline{E}_i(\underline{r}) \underline{E}_p(\underline{r}) e^{-i(\omega_i + \omega_p)t} \quad (59)$$

For non planar signal and/or pump fields, which is the case for imaging, it would be advantageous to solve the inhomogeneous wave equation for the angular spectrum component waves rather than solving Eq. (58) directly. The wave equation for Fourier components wave is (Appendix B)

$$\nabla \times \nabla \times \underline{\mathcal{E}}_{-\underline{s}}(\underline{k}_{-\underline{s}}, z) - \underline{\epsilon}_e : \underline{\mathcal{E}}_{-\underline{s}}(\underline{k}_{-\underline{s}}, z) = 4\pi \left(\frac{\omega_s}{C} \right)^2 \underline{\mathcal{P}}(\underline{k}_{-\underline{s}}, z) \quad (60)$$

It is apparent that operation ∇ on angular spectrum only has $\frac{\partial}{\partial z} \hat{z}_0$ operation. In this analysis Cartesian coordinates x, y, z are defined such that z is in the propagation direction normal to the surface of the crystal, and the optic axis (consider only uniaxial crystals) - is in the xz plane (Fig. 11). If both signal and pump fields are ordinary wave polarized with the electric vectors perpendicular to the xz plane (along the y direction) the effective component of the polarization wave and the sum-frequency electric field are polarized along the x axis. For this simple case Eq. (60) becomes

$$\left(\frac{\partial^2}{\partial z^2} + \epsilon_e \right) \mathcal{E}_{sx}(\underline{k}_{-\underline{s}}, z) = 4\pi \left(\frac{\omega_s}{C} \right)^2 \mathcal{P}_x(\underline{k}_{-\underline{s}}, z) \quad (61)$$

where

$$\begin{aligned} \epsilon_e &= (\epsilon_e)_{11} \\ \mathcal{P}_x &= d \mathcal{E}_{iy}(\underline{k}_{-\underline{s}}, z) \otimes \mathcal{E}_{py}(\underline{k}_{-\underline{s}}, z) \\ &\text{(See Appendix C)} \end{aligned}$$

The general solution of Eq. (60) consists of an inhomogeneous wave (or forced wave) which is some convenient particular solution of inhomogeneous equation, and suitable free waves which are solutions of the homogeneous equation obtained by setting $\mathcal{P}_{-\underline{s}} = 0$. The free waves are required so as to satisfy the boundary conditions at the crystal surface. The

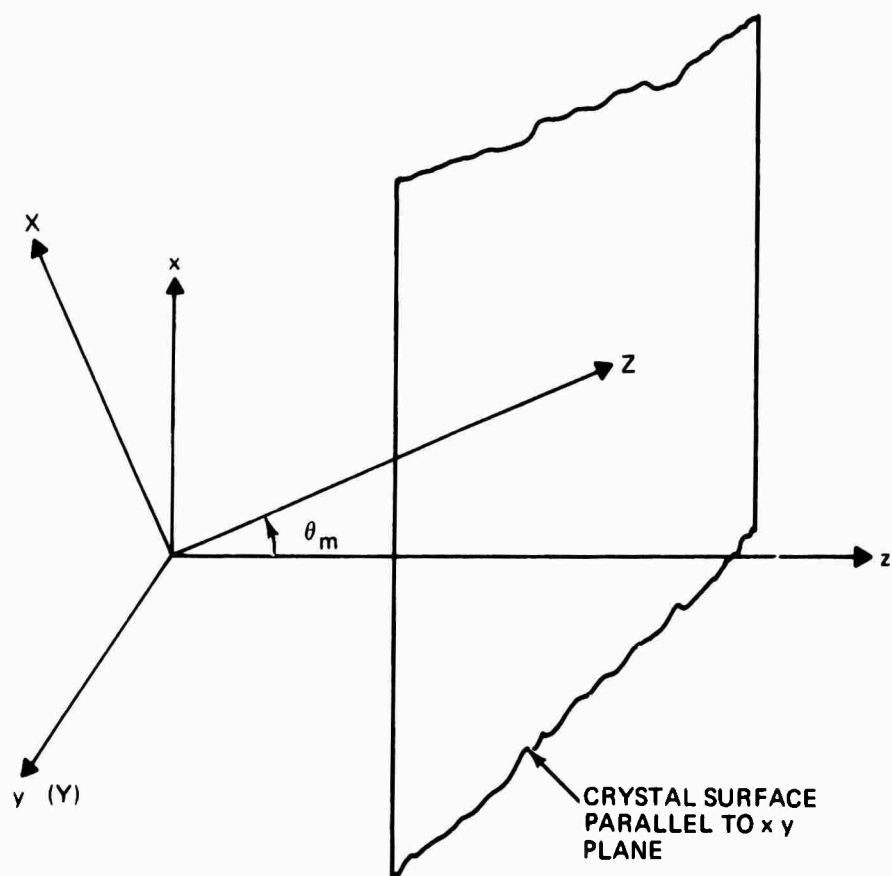


FIGURE 11. RELATION BETWEEN THE COORDINATES (x , y , z) AND THE CRYSTALLOGRAPHIC AXIS (X , Y , Z)

free waves have the form

$$\delta \underline{u} \exp i \left(\frac{\omega_s^2}{C^2} n_s^2 - \kappa_s^2 \right)^{1/2} z \quad (62)$$

where the refractive index n_s is a function of the free wave propagation direction \underline{s} (unit vector) of the wave vector

$$\underline{K} = \frac{\omega_s}{C} n_s \underline{s} \quad (63)$$

The relation between the wave vector \underline{K} of free wave and the wave vector \underline{K}_s of the polarization wave $\underline{P}_s(\underline{r})$ will be considered later. The polarization direction \underline{u} satisfies the relation

$$\underline{\alpha}_s : \underline{u} = 0 \quad (64)$$

where

$$\underline{\alpha}_s = \frac{\omega_s^2}{C^2} (n_s^2 \underline{I} - \underline{\epsilon}) - \kappa_s \kappa_s \quad (65)$$

where \underline{I} is the unit dyadic and $\underline{\epsilon}$ is the dielectric constant tensor at sum-frequency ω_s . Equations (64) and (65) determine both n_s and the polarization direction \underline{u} . We define a quantity n' , called effective index, and a unit vector $\underline{\sigma}$ by the relation

$$\underline{K}_s = \frac{\omega_s}{C} n' \underline{\sigma} \quad (66)$$

In general $n' \neq n_s(\underline{\sigma})$, but $n' = n_s(\underline{\sigma})$ along the phase-match direction.

When $n' \neq n_s(\underline{\sigma})$, the polarization wave is said to be mismatched, the mismatch is described quantitatively by φ in the relation⁽²³⁾

$$n' \underline{\sigma} - n_s \underline{s} = \varphi \underline{N} \quad (67)$$

or

$$\underline{K}_s = \underline{K} + \frac{\omega}{C} \underline{s} \cdot \underline{N} \quad (68)$$

where \underline{N} is the direction (unit vector) normal to the incident surface of the crystal. These equations determine both \underline{s} and \underline{u} to be associated with a prescribed \underline{K}_s . Here \underline{u} and \underline{s} specify a free wave expressed by Eq. (62) which must exist in the presence of the forced wave in order to satisfy boundary condition at the crystal surface. The dominant effect of presence of both forced and free waves is the production of growing wave through interference of a free wave and forced wave⁽²³⁾. When $\varphi = 0$ the waves are said phase matched and the growing wave is given by Eq. (57). More generally under nearly matching conditions following Kleinman⁽²³⁾ it can be shown that the growing wave is given by

$$\underline{S}(\underline{K}_s, z) = z G(2 + \epsilon) \underline{\underline{z}} : \underline{\underline{\sigma}}(\underline{K}_s, z) \quad (69)$$

where

$$G(a) = \frac{1 - e^{-a}}{a} = \int_0^1 e^{-ax} dx \quad (70)$$

and

$$2 + \frac{\omega}{C} \underline{s} \cdot \underline{z} = z |\underline{K}_s - \underline{K}| \quad (71)$$

The dyadic $\underline{\underline{z}}$ is defined by⁽²³⁾

$$\underline{\underline{z}} = -2 + i \frac{\omega}{C(n_s n_i)} \frac{1}{2} [(\underline{N} \cdot \underline{u})(\underline{v} \cdot \underline{u}) - \underline{N} \cdot \underline{\sigma}]^{-1} \underline{u} \underline{u} \quad (72)$$

To a good approximation ϵ can be written (23)

$$\epsilon = \frac{2\pi}{C(\ln n_1)} \left(\frac{\omega_s}{\omega_p} \right)^2 \quad (73)$$

provided waves travel nearly normal to the surface. For the case of an ordinary pump wave, an ordinary signal wave, and an extraordinary sum-frequency wave, the growing wave in Eq. (69) becomes

$$\delta_{\text{ex}}(x_0, z) = \frac{2\pi}{C(\ln n_1)} \left(\frac{\omega_s}{\omega_p} \right)^2 \epsilon(2\omega_s) \phi_{\text{ex}}(x_0, z) \quad (74)$$

Equations (69) and (74) can be written in more familiar form¹ by noting that

$$\epsilon(2\omega_s) = e^{-i\phi} \frac{\sin \phi}{\phi}$$

II-2 EVALUATION OF MISMATCH FACTOR

Before Eq. (69) can be applied it is necessary to express the mismatch factor ϕ in terms of wave vectors. Eq. (68) gives that

$$\phi = \frac{\omega_s}{C} (\underline{K}_s - \underline{K}) \cdot \underline{N} \quad (76)$$

As shown in Figure 12 the wave vector \underline{K} of free waves is constrained to lie on the wave vector surface $\frac{\omega_s}{C} n(\underline{s})$ for the sum-frequency ω_s ; the wave vector \underline{K}_s of polarization wave is given by $\underline{K}_s = \underline{K}_1 + \underline{K}_p$ and is arbitrary. We shall denote the wave vector of polarization wave in the matching direction by \underline{K}_M . We shall assume, for simplicity, that the surface normal \underline{N} is a matching direction and also that \underline{K}_M is in the direction \underline{N} . Figure 12 shows geometrically the mismatch relation expressed by Eq. (76). We have taken the z direction to be along \underline{N} , the optic axis in the xz plane, and the y direction normal to the plane of figure. The tangent plane to the

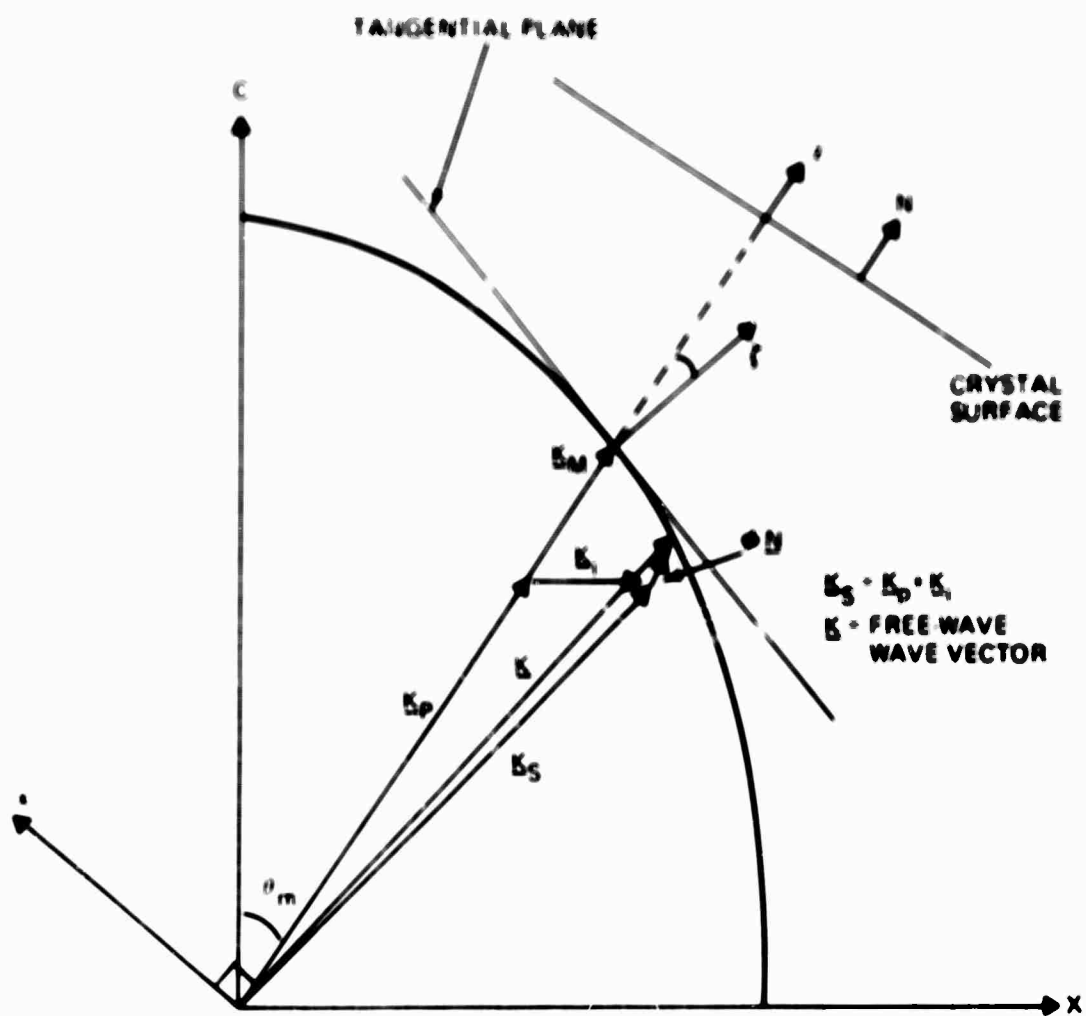


FIGURE 12. GEOMETRIC REPRESENTATION OF MISMATCH RELATION

wave vector surface at \underline{K}_M is shown, and the normal to this plane make the angle ζ with the z axis. It should be noted that the angle ζ represents anisotropy of the crystal at the frequency ω_s . The anisotropy angle ζ is given by (Appendix D).

$$\tan \zeta = n^2(\theta_m) \cos \theta_m \sin \theta_m \left(\frac{1}{n_o^2} - \frac{1}{n_e^2} \right) \quad (77)$$

where θ_m - angle between the optic axis and the phase match direction
 $n(\theta_m)$ - index of refraction along \underline{K}_M at ω_s
 n_e - extraordinary-wave index of refraction at ω_s
 n_o - ordinary-wave index of refraction at ω_s

This angle also governs the double refraction effect, in which both the ordinary and extraordinary waves are at the same frequency. In this analysis it was assumed that the signal field and the pump field are both polarized as ordinary waves and the sum-frequency field is polarized as extraordinary waves. The mismatch factor φ according to Eq. (76) is the distance from \underline{K}_s to the wave vector surface measured parallel to \underline{N} . This is apparent from the boundary condition that requires continuity of transvers wave vectors of both forced and free waves across the boundary surface.

$$\underline{\kappa} = \underline{\kappa}_s = \underline{\kappa}_p + \underline{\kappa}_i \quad (78)$$

This condition assures also the continuity of an angular spectra with spatial angular frequency $\underline{\kappa}_s$ across the crystal boundary. It is somewhat tedious but can be shown that (Appendix D)

$$\frac{\omega_s}{C} \varphi = K_{sz} - K_M + \kappa_{sx} \tan \zeta + \frac{K}{2} \left[\left(\frac{K_M \kappa_{sx} C^2}{n_e n_o \omega_s^2} \right) + \left(\frac{\kappa_{sy} C}{n_e \omega_s} \right)^2 \right] \quad (79)$$

where

$$K_{\perp}^2 = K_{\perp x}^2 + K_{\perp y}^2$$

and

$$K_{\perp}^2 = (K_{\perp}^2 + K_{\parallel}^2)$$

Since the crystal is usually nearly isotropic and the quantity in the square bracket is second-order in $(K_{\perp} - K)$ and smaller than the linear quantity, it is proper to use simpler form

$$\frac{K_{\perp}^2}{C} \approx K_{\perp}^2 - K_M^2 = K_{\perp x}^2 \left(1 - \frac{K_{\perp}^2}{2K_M^2} \right) \quad (80)$$

We have used $\tan \epsilon \approx \epsilon$ in Eq. (80) since $\epsilon \ll 1$.

II-3 RESULTANT SUM-FREQUENCY FIELD

The sum-frequency angular spectrum component $\delta_{\underline{s}=\underline{s}}(\underline{\kappa}, z)$ given by Eq. (69) is generated by a plane wave polarization $\phi(\underline{\kappa}, z)$, which is a Fourier component of total polarization wave $\underline{P}(z)$. The resultant sum-frequency field produced by $\underline{P}(z)$ is Fourier transform of $\delta_{\underline{s}=\underline{s}}(\underline{\kappa}, z)$

$$E_{\underline{s}}(\underline{r}) = \int \delta_{\underline{s}=\underline{s}}(\underline{\kappa}, z) e^{i\underline{\kappa} \cdot \underline{s}} d\underline{\kappa} \quad (81)$$

Substituting Eq. (69) into Eq. (81) the resultant field can be written

$$E_{\underline{s}}(\underline{r}) = z \int_0^1 d\eta \int \underline{\kappa} : \phi(\underline{\kappa}, z) e^{-2i\eta \underline{\kappa} \cdot \underline{r}} e^{i\underline{\kappa} \cdot \underline{r}} d\underline{\kappa} \quad (82)$$

where use has been made of integral representation in Eq. (70).

For paraxial assumption the quadratic term $\kappa_s^2/2K_M^2$ can be neglected. It then follows from Eqs. (82) and inverse Fourier integral representation of $\phi(\underline{\kappa}, z)$ that

$$\begin{aligned} \underline{E}_s(\underline{r}) = \frac{1}{(2\pi)^2} \int_0^1 d\eta \int d\underline{r}' e^{i\underline{k}_s \cdot \underline{r}'} \underline{P} e^{-i\eta z(K_{sx} - K_{Mx} + K_{sy})} \\ \cdot \int d\underline{p}' \underline{P}(\underline{r}') e^{-i\underline{k}_s \cdot \underline{p}'} \end{aligned}$$

The integration over \underline{r}' gives the factor

$$(2\pi)^2 \delta(\underline{x} - \underline{x}' - \eta \underline{z}) \delta(\underline{y} - \underline{y}')$$

The integration over \underline{p}' gives

$$\underline{E}_s(\underline{r}) = \underline{z} \int_0^1 d\eta e^{-i\eta K_M D} \underline{z} : \underline{P}(\underline{x} - \eta \underline{z}, \underline{y}, \underline{z}) \quad (84)$$

Then the field at the exit surface of the nonlinear crystal ($z = D$) can be written

$$\underline{E}_s(\underline{p}, D) = D \int_0^1 d\eta e^{-i\eta K_M D} \underline{z} : \underline{P}(\underline{x} - \eta D, \underline{y}, D) \quad (85)$$

If we let $(1 - \eta) D = z$ and make z as a dummy variable of integration Eq. (85) becomes

$$\underline{E}_s(\underline{p}, D) = e^{-iK_M D} \int_0^D dz e^{iK_M z} \underline{z} : \underline{P}(\underline{x} - (D - z), \underline{y}, D) \quad (86)$$

This expression shows that the resultant sum-frequency field is produced by constructive interference of the waves radiated from each differential slab of polarization in the material. It is this concept that was used in the geometric optics theory. Double refraction (or anisotropy effect) of the sum frequency electric field is included in Eq. (86) through the parameter $(\underline{x} - (D - z))$. Now refer to Figure 13 the line at angle ζ , which is normal to the tangential plane to the wave vector surface, represents the direction of energy flow of the sum-frequency field⁽²⁷⁾. It is intuitive to expect that the path of integration to obtain resultant field should be along the energy flow direction rather than the z direction. To understand the implication of

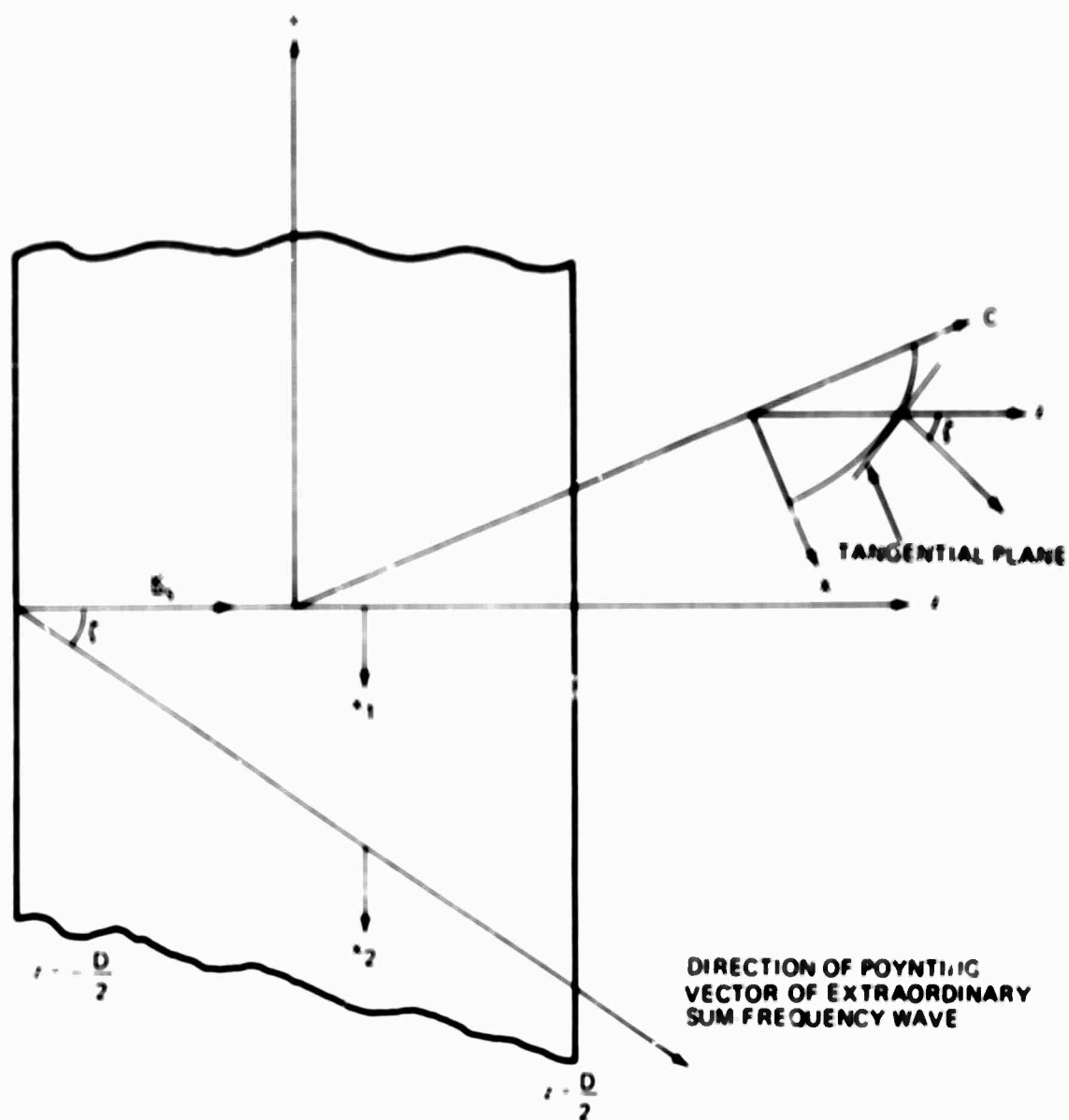


FIGURE 13. ILLUSTRATION OF DOUBLE REFRACTION OF SUM-FREQUENCY WAVE

the parameter $\lambda = (1) + (2)$, let us denote points in the polarization wave the source points, by (x_1, y_1, z_1) , and points in the sum-frequency wave the observer points, by (x_2, y_2, z_2) . We regard Eq. (86) as an integral over source points giving the sum-frequency field at an observer point. We shall measure the source points from the coordinate origin. We define x_2 for the observer points in such a way that $x_2 = 0, y_2 = 0$ lies on the line making angle ℓ with the z axis. Then $x_2 = (z_2)$ and the path of integration over the source points is specified by $x_1 = x_2 + (z_1), y_1 = y_2 + y$, with x_2 hold constant in the integration since it refers to the observation point. Then when we set $z_2 = 0$, we obtain the integration parameter $x_1 = \lambda = (1) + (2)$. This can be interpreted that the sum-frequency field at the points $(x, y, 0)$ is obtained by integration along the energy flow line.

The angular spectrum of the sum-frequency field at the exit surface of the crystal is simply

$$\delta_{-s}(k_{-s}, 0) = D e^{-i \frac{\Delta K D}{2}} \frac{\sin \left(\frac{\Delta K D}{2} \right)}{\left(\frac{\Delta K D}{2} \right)} \delta_{-s}(k_{-s}, D) \quad (87)$$

where

$$\Delta K = K_{sz} - K_n = (k_{sx} + \frac{k_s^2}{2K_M})^2 \quad (88)$$

Eq. (87) indicates that the angular spectrum at the exit surface is not a summation over the contributions of the Fourier components of the polarization in the differential slab. Firester⁽¹³⁾ calculated the angular spectrum at the exit surface by summing over the angular spectrum of same spatial frequency k_s radiated in each differential slab. By doing so he obtained the factor

$$\sin \left[\frac{k_s^2 D}{4} \left(\frac{1}{K_i} - \frac{1}{K_s} \right) \right] / \left[\frac{k_s^2 D}{4} \left(\frac{1}{K_i} - \frac{1}{K_s} \right) \right] \text{ and considered it as a}$$

consequence of mismatch. This interpretation is contrary to his initial assumption of isotropical phase match condition. Because of this he arrived at incorrect relation for locations of the object and the upconverted image.

III. ANGULAR SPECTRUM OF IMAGE FIELD FOR SEVERAL IMAGE UPCONVERSION SYSTEMS

The results obtained in preceding section will be used to evaluate the angular spectrum of the sum-frequency image field for several upconverter systems. It should be pointed out here that Eq. (69) takes into account of mismatch and anisotropy. It will be shown that the finite interaction aperture may be included in the calculation by introducing aperture function. It will be shown in this section that the image position relation derived in the geometric optics theory is obtained from stationary phase consideration. To compare the results of this section with that of geometric optics theory, it was assumed that the nonlinear material fills the space bounded by parallel planes $z = -D/2$ and $z = D/2$ (Fig. 13). It was also assumed that all field quantities have definite polarization, since parametric upconversion in a nonlinear crystal generally requires definite polarization for phase matching. For simplicity we again consider that the infrared object and the pump waves are polarized as ordinary waves and the sum-frequency fields are polarized as extraordinary wave. For this case the field and the polarization wave can be described by scalar quantities.

III-1 PLANE WAVE PUMP SYSTEM

For a plane pump wave propagating in the direction of the axis

$$E_p(r) = E_p e^{iK_p z} \quad (89)$$

its angular spectrum is simply a two-dimensional delta function multiplied by a phase factor

$$\delta_{-p-p}(\kappa, z) = E_p e^{iK_p z} \delta(\kappa_{-p}) / (2\pi)^2 \quad (90)$$

Inside the material the pump angular spectrum becomes

$$\delta_p(\underline{k}_p, z) = T_p \delta_p(\underline{k}_p) e^{-i \left[K_{pa}^2 - K_p^2 \left(z - \frac{D}{2} \right) \right]} \quad (91)$$

where

$$-\frac{D}{2} < z < \frac{D}{2}$$

$$K_{pa} = \frac{2\pi}{\lambda_p} \text{ - free space wave number}$$

$$K_p = \frac{2\pi n_p}{\lambda_p} \text{ - wave number in the crystal}$$

and

T_p - transmission coefficient for the pump wave at the material surface

Let the object field distribution across the plane $z = s$ be denoted by $E_1(\underline{\rho}, s)$, then its angular spectrum inside the nonlinear crystal is given by

$$\delta_1(\underline{k}_1, z) = T_1 \delta_1(\underline{k}_1, -s) e^{-i \left[(K_{1a}^2 - \epsilon_1^2)^{1/2} \left(z - \frac{D}{2} \right) + (K_1^2 - \epsilon_1^2) \left(z - \frac{D}{2} \right) \right]} \quad (92)$$

where

$$-\frac{D}{2} < z < \frac{D}{2}$$

$$\delta_1(\underline{k}_1, -s) = \frac{1}{(2\pi)^2} \int E_1(\underline{\rho}, -s) e^{-i \underline{k}_1 \cdot \underline{\rho}} \quad (93)$$

$$K_{1a} = \frac{2\pi}{\lambda_1} \text{ - free space wave number}$$

$$K_1 = \frac{2\pi n_1}{\lambda_1} \text{ - wave number inside the crystal}$$

T_i - transmission coefficient for the angular spectrum at the material surface.

Transmission coefficient T_i depends on the vector $\underline{\kappa}_i$, since $\underline{\kappa}_i$ determines the incidence angle of a spectral component and transmission coefficient depends on the incidence angle. For the paraxial assumption, which is valid for the most of upconverters, we can neglect the $\underline{\kappa}_i$ dependence of transmission coefficient T_i and approximate it by a constant.

The angular spectrum of polarization wave, convolution of $\mathcal{S}_{p-p}(\underline{\kappa}, z)$ and $\mathcal{S}_i(\underline{\kappa}_i, z)$, is given by

for $-\frac{D}{2} \leq z \leq \frac{D}{2}$

$$\begin{aligned} \Phi(\underline{\kappa}_s, z) = dT_p T_i \mathcal{S}_p \mathcal{S}_i(\underline{\kappa}_s, -s) e^{-i[K_{pa} \frac{D}{2} - K_p(z + \frac{D}{2})]} \\ e^{i[(K_{ia}^2 - \kappa_s^2)^{1/2}(s - \frac{D}{2}) + (K_i^2 - \kappa_i^2)^{1/2}(z + \frac{D}{2})]} \end{aligned} \quad (94)$$

$$\Phi(\underline{\kappa}_s, z) = 0 \quad \text{for } -\frac{D}{2} > z > \frac{D}{2}$$

From phase match condition $K_{sz} = K_{iz} + K_{pz}$ and $\underline{\kappa}_s = \underline{\kappa}_i + \underline{\kappa}_p$ and $\underline{K}_p = K_p \hat{z}_o$ it can be shown

$$K_{sz} = K_p + (K_i^2 - \kappa_s^2 - \kappa_s^2)^{1/2} = (K_s^2 - \kappa_s^2)^{1/2}$$

where

$$\underline{K}_s = K_{sz} \hat{z}_o + \underline{\kappa}_s$$

Substituting this relation, Eq. (94) can be rewritten as

$$\begin{aligned} \Phi(\underline{\kappa}_s, z) = dT_p T_i \mathcal{S}_p \mathcal{S}_i(\underline{\kappa}_s, -s) e^{iK_{pa} \frac{D}{2}} e^{i[(K_{ia}^2 - \kappa_s^2)^{1/2}(z + \frac{D}{2}) - (K_{ia}^2 - \kappa_{pa}^2)^{1/2} \frac{D}{2}]} \\ e^{i(K_{ia}^2 - \kappa_s^2)^{1/2} s} \end{aligned} \quad \text{for } -\frac{D}{2} \leq z \leq \frac{D}{2} \quad (95)$$

The angular spectrum of the sum-frequency field is obtained from Eqs. (74), (75) and (95),

$$\begin{aligned} \mathcal{E}_s(\underline{\kappa}_s, z) = i \frac{2\pi\omega_s d T_p T_i \mathcal{E}_p}{C(n_s n_i)^{1/2}} \mathcal{E}_i(\underline{\kappa}_s, -s)(z + \frac{D}{2}) \frac{\sin \left[\frac{\Delta k(z + \frac{D}{2})}{2} \right]}{\left[\frac{\Delta k(z + \frac{D}{2})}{2} \right]} \\ \times e^{-i \frac{\Delta K(z + \frac{D}{2})}{2}} e^{-i \left[(K_{ia}^2 - \kappa_s^2)^{1/2} \frac{D}{2} + K_{pa} \frac{D}{2} - (K_{ia}^2 - \kappa_s^2)^{1/2} s - (K_s^2 - \kappa_s^2)^{1/2} (z + \frac{D}{2}) \right]} \\ -\frac{D}{2} \leq z \leq \frac{D}{2} \end{aligned} \quad (96)$$

where ΔK is given by Eq. (88)

The angular spectrum of upconverted field beyond the exit surface of crystal is given by

$$\mathcal{E}_s(\underline{\kappa}_s, z) = T_s \mathcal{E}_s(\underline{\kappa}_s, \frac{D}{2}) e^{i(K_{sa}^2 - \kappa_{sa}^2)^{1/2} (z - \frac{D}{2})} \quad z > \frac{D}{2} \quad (97)$$

where

T_s = transmission coefficient at the exist surface

$K_{sa} = \frac{2\pi}{\lambda_s}$ = free space wave number at ω_s

It follows then from Eqs. (96) and (97)

$$\begin{aligned}
\mathcal{G}_{\underline{s}}(\underline{\kappa}_{\underline{s}}, z) = \mathcal{G}_{\underline{i}}(\underline{\kappa}_{\underline{s}}, -s) \frac{\text{Sin}(\frac{\Delta KD}{2})}{\frac{\Delta KD}{2}} e^{-i\frac{\Delta KD}{2}} \cdot \frac{2\pi_i \omega_s T_s T_i T_p d\mathcal{G}_p D}{C(n_s n_i)^{1/2}} \\
\cdot e^{-i[(K_{ia}^2 - \kappa_s^2)^{1/2}(\frac{D}{2} - s) + K_{pa}\frac{D}{2} - (K_s^2 - \kappa_s^2)^{1/2}D - (K_{sa}^2 - \kappa_s^2)^{1/2}(z - \frac{D}{2})]}
\end{aligned} \quad (98)$$

where

$$z > \frac{D}{2}$$

For the case of a plane object wave $E_i(\underline{r}) = E_i e^{i\kappa \cdot \underline{\rho}} e^{iK_{iz}z}$, its angular spectrum are

$$\mathcal{G}_{\underline{i}}(\underline{\kappa}_{\underline{s}}, -s) = \mathcal{G}_{\underline{i}} \delta(\underline{\kappa}_{\underline{s}} - \underline{\kappa})$$

The resultant sum-frequency field, which can be calculated by taking Fourier transform of Eq (98), becomes

$$\begin{aligned}
E_s(\underline{\rho}, z) = i \frac{2\pi\omega_s dT_i T_p T_s T_p E_i D}{C(n_s n_i)^{1/2}} \frac{\text{Sin}(\frac{\Delta KD}{2})}{(\frac{\Delta KD}{2})} e^{-i\frac{\Delta KD}{2}} \\
\cdot e^{-i[(K_{ia}^2 - \kappa^2)^{1/2}\frac{D}{2} + K_{pa}\frac{D}{2} - (K_s^2 - \kappa^2)^{1/2}\frac{D}{2} + (K_{sa}^2 - \kappa^2)(z - \frac{D}{2})]} \\
\text{for } z > \frac{D}{2}
\end{aligned} \quad (99)$$

The sum-frequency field is also a plane wave and its amplitude is reduced by the mismatch function $\text{Sin}(\frac{\Delta KD}{2})/(\frac{\Delta KD}{2})$. For plane object wave propagating along the z axis κ is equal to zero and the mismatch function becomes unity because of $\Delta K = 0$, and Eq. (97) reduces to Eq. (57) if we ignore the phase change expressed as exponential in Eq. (99).

We shall next consider the relation of image location to the object location by investigating the phase factor of Eq. (98). Using Eq. (88) for ΔK and the approximation

$$(K^2 - \kappa^2)^{1/2} \approx K - \frac{\kappa^2}{2K}$$

which is valid for paraxial assumption, the phase factor of $\mathcal{E}_{\underline{\kappa}_s}(z)$ is given by

$$\begin{aligned} & (K_{sa} - \frac{\kappa_s^2}{2K_{sa}})(z - \frac{D}{2}) - (K_{ia} - \frac{\kappa_s^2}{2K_{ia}})(\frac{D}{2} - s) + K_{pa} \frac{D}{2} + (K_s - \frac{\kappa_s^2}{2K_s})D \\ & - [K_s - K_M + \zeta_{\underline{\kappa}_{sx}} + \frac{\kappa_s^2}{2}(\frac{1}{K_M} - \frac{1}{K_s})] \frac{D}{2} \end{aligned}$$

Since the constant phase factor that is independent of $\underline{\kappa}$ is common to all the angular spectrum and represent a constant phase shift, it can be ignored.

The phase factor that depends on $\underline{\kappa}$ is then

$$\Phi(\underline{\kappa}_s) = - [\zeta_{\underline{\kappa}_{sx}} \frac{D}{2} + \frac{\kappa_s^2}{2} (\frac{z}{K_{sa}} - \frac{D}{2K_{sa}} - \frac{D}{2K_{ia}} + \frac{D}{2K_M} + \frac{s}{K_{ia}} + \frac{D}{2K_s})] \quad (100)$$

Optimum focusing occurs when $\Phi(\underline{\kappa}_s)$ is identically equal to zero for all $\underline{\kappa}_s$.

If this condition is satisfied, the phase angle of all angular spectrum becomes identically equal and the resultant field at the sum frequency will form a clearly defined image across a plane $z = -s'$ which makes $\Phi(\underline{\kappa}_s) \equiv 0$.

Unfortunately, the condition $\Phi(\underline{\kappa}_s) = 0$ for all $\underline{\kappa}_s$ can not be satisfied, since we have one equation and two independent variable $\underline{\kappa}_{sx}$ and $\underline{\kappa}_{sy}$.

There is no unique solution $z = -s'$ that makes $\Phi(\underline{\kappa}_s) = 0$ for all $\underline{\kappa}_s$.

There is, however, a solution $z = -s'$ for a particular $\underline{\kappa}_s$. This can be interpreted that different components of angular spectrum focus on different

transverse plane. The sum frequency field produces, therefore, a blurred image. The origins of this image degradation are crystal anisotropy and phase mismatch. It is natural to expect that the upconverter is not circular symmetric because of crystal anisotropy.

When the linear phase factor $\xi_{\underline{\kappa}_{sx}} D$ is ignored, which is valid assumption for the most of upconverters because of paraxial assumption and small anisotropy, there is a unique solution $z = -s'$ that makes $\Phi(\underline{\kappa}_s) = 0$ for all $\underline{\kappa}_s = 0$ for all $\underline{\kappa}_s$ provided $K_s = |\underline{K}_i + \underline{K}_p|$ is a constant,

$$s' = s \frac{K_{sa}}{K_{ia}} + \frac{DK_{sa}}{2} \left(\frac{1}{K_s} + \frac{1}{K_M} - \frac{1}{K_{ia}} - \frac{1}{K_{sa}} \right) \quad (101)$$

For infinitesimally thin crystal, $D \approx 0$ and Eq. (101) reduces to

$$s' = s \lambda_i / \lambda_s \quad (102)$$

This equation is identical to the result obtained by the geometric optics theory. (Eq. (6) of Chapter 2 with $p = \infty$).

The assumption $K_s = \text{constant}$ is not valid since K_s is related to

$\underline{\kappa}_i (= \underline{\kappa}_s)$ by the equation

$$K_s^2 = \kappa_s^2 + (K_{iz} + K_p)^2$$

When both pump and object waves are ordinary waves, it is true that $K_i^2 + K_p^2 (= \kappa_i^2 + K_{iz}^2 + K_p^2)$ is a constant, but K_s is obviously not a constant. The unique solution $z = -s'$ that makes $\Phi(\underline{\kappa}_s) \equiv 0$ for all $\underline{\kappa}_s$ does, therefore, not exist even for an upconverter of isotropic crystal. It is clear now that thickness aberration introduced in the geometric optics theory is due to non-uniqueness in the position of stationary phase plane and amplitude reduction of angular spectrum of the image field caused by the mismatch.

The angular aperture of the upconverter can be calculated from the condition $\text{Sin}(\frac{\Delta KD}{2}) = 0$. This relation will give the extreme values for $\underline{\kappa}_s$ and consequently the maximum object wave incidence angle. This procedure is carried out in the geometric optics theory and the result is presented in Sec. IV-2, Chapter 2.

The amount of longitudinal spread of upconverted image may be evaluated from Eq. (101) by substituting extreme values of $\underline{\kappa}_s$ obtained from the condition $\text{Sin}(\frac{\Delta KD}{2}) = 0$. The electric field distribution of sum-frequency image of a point object located at $z = -s$ will be considered. We assume that crystal anisotropy is small so that $\zeta = 0$. The image field distribution will be evaluated over the plane $z = -s'$ given by Eq. (101). The angular spectrum $\mathcal{E}_i(\underline{\kappa}, -s)$ of a point object field $E_i \delta(\underline{\rho} - \underline{\rho}_i)$ is

$$\mathcal{E}_i(\underline{\kappa}_s, -s) = \mathcal{E}_i e^{i \underline{\kappa}_s \cdot \underline{\rho}_i} \quad (103)$$

We set $\underline{\rho}_i = 0$ for simplicity.

The angular spectrum over the plane $z = -s'$ is, neglecting constant phase factor, then

$$\mathcal{E}_s(\underline{\kappa}_s, -s') = \mathcal{E}_s \frac{\text{Sin}(\frac{\Delta KD}{2})}{(\frac{\Delta KD}{2})} \quad (104)$$

where

$$\mathcal{E}_s = i \frac{2\pi\omega \underline{T}_s \underline{T}_s \underline{T}_i \underline{p}_p \underline{p}_i}{c(n_s n_i)^{1/2}} \quad (105)$$

$$\Delta K \approx -\frac{\underline{\kappa}_s^2}{2K_i} \quad (\text{See Appendix F})$$

The image field is Fourier transform of Eq. (104)

$$E_s(\underline{\rho}, -s') = -\mathcal{G}_s \int \left[\frac{\sin\left(\frac{\kappa_s^2 D}{4K_i}\right)}{\left(\frac{\kappa_s^2 D}{4K_i}\right)} \right] e^{i\kappa_s \cdot \underline{\zeta}_s} d\kappa_s$$

Using polar coordinate expression $\underline{\kappa}_s = \kappa_s e^{i\theta}$ and $\underline{\rho} = \rho e^{i\alpha}$, we can convert above integration to Hankel transform

$$E_s(\underline{\rho}, -s') = -2\pi\mathcal{G}_s \int_0^\infty \frac{\sin\left(\frac{\kappa^2 D}{4K_i}\right)}{\left(\frac{\kappa^2 D}{4K_i}\right)} J_0(\kappa\rho) \kappa d\kappa \quad (106)$$

where J_0 is zeroth order Bessel function. $E_s(\rho, -s)$ can be expressed in the form (Appendix E)

$$E_s(\rho, -s') = -\frac{4\pi K_i \mathcal{G}_s}{D} \left[\frac{\pi}{2} - \text{Si}\left(\frac{K_i \rho^2}{D}\right) \right] \quad (107)$$

where sine integral function is given by

$$\text{Si}(x) = \int_0^x \frac{\sin t}{t} dt$$

The function $\left[\frac{\pi}{2} - \text{Si}\left(\frac{K_i \rho^2}{D}\right) \right]$ has the same character as the function describing diffraction from a round hole. The image field distribution $E_s(\rho, -s')$, consequently the extent of aberration, is independent of the object location. This result agrees with that of the geometric optics theory.

It should be noted that the spread of sum-frequency image given in Eq. (107) is caused by thickness aberration. The spread is not due to aperture diffraction, since we assumed an infinitely wide crystal. It is easily seen from Eq. (107) that the field spread becomes wider for the thicker nonlinear material. It also can be shown that $E_S(\rho, -s')$ approaches to the delta function as the material thickness D approaches zero.

The sum-frequency electric field expressed in Eq. (107) is a point spread function of the system under consideration. The minimum resolvable image spot size according to Rayleigh criteria may be calculated by noting that the function $\frac{\pi}{2} - \text{Si}(x)$ possesses first zero at $x \approx 2$. The radius of resolvable spot size is then

$$\rho_{\text{res.}} = 1.4 (D/K_i)^{1/2} \quad (108)$$

III-2 SPHERICAL WAVE PUMP SYSTEM

We shall consider the upconverter pumped by spherical waves. A point pump source that radiates spherical wave is located at the point $(x_p, y_p, -p)$. The pump field distribution across the plane $z = -p$ is expressed by

$$E_p(\underline{\rho}, -p) = E_p \delta(x-x_p) \delta(y-y_p)$$

The angular spectrum of this point pump source is then

$$\mathcal{E}_p(\underline{k}, -p) = \mathcal{E}_p e^{-i\underline{k} \cdot \underline{\rho}_p}$$

where

$$\mathcal{E}_p = E_p / (2\pi)^2 \quad \text{and} \quad \underline{\rho}_p = x_p \hat{x}_0 + y_p \hat{y}_0$$

We assume again that an object is located on the plane $z = -s$ and its angular spectrum is given by $\mathcal{G}_i(\underline{\kappa}_i, -s)$. The angular spectral of pump field and object field inside the crystal are respectively

$$\mathcal{G}_{p-p}(\underline{\kappa}_p, z) = T_p \mathcal{E}_p e^{-i[\underline{\kappa}_p \cdot \underline{\rho}_p - (K_{pa}^2 - \kappa_p^2)^{1/2}(p - \frac{D}{2}) - (K_p^2 - \kappa_p^2)^{1/2}(z + \frac{D}{2})]} \quad \text{for } -\frac{D}{2} \leq z \leq \frac{D}{2} \quad (109)$$

$$\mathcal{G}_i(\underline{\kappa}_i, z) = T_i \mathcal{G}_i(\underline{\kappa}_i, -s) e^{i[(K_{ia}^2 - \kappa_i^2)^{1/2}(s - \frac{D}{2}) + (K_i^2 - \kappa_i^2)^{1/2}(z + \frac{D}{2})]} \quad -\frac{D}{2} \leq z \leq \frac{D}{2}$$

The angular spectrum of polarization wave, calculated again by taking convolution of $\mathcal{G}_{p-p}(\underline{\kappa}_p, z)$ and $\mathcal{G}_i(\underline{\kappa}_i, z)$ is given by

$$\begin{aligned} \mathcal{P}(\underline{\kappa}_s, z) = dT_i T_p \mathcal{E}_p e^{i[(K_s^2 - \kappa_s^2)(z + \frac{D}{2}) + K_{ia}(s - \frac{D}{2}) + (K_{pa}^2 - \kappa_s^2)^{1/2}(p - \frac{D}{2}) - \underline{\kappa}_s \cdot \underline{\rho}_p]} \\ \cdot \int d\underline{\kappa}' \mathcal{G}_i(\underline{\kappa}', -s) e^{-i[\kappa'^2(\frac{s - \frac{D}{2}}{2K_{ia}} + \frac{p - \frac{D}{2}}{2K_{pa}}) - \underline{\kappa}' \cdot [\frac{p - \frac{D}{2}}{K_{pa}} \underline{\kappa}_s + \underline{\rho}_p]]} \end{aligned}$$

$$-\frac{D}{2} \leq z \leq \frac{D}{2}$$

$$\mathcal{P}(\underline{\kappa}_s, z) = 0 \quad -\frac{D}{2} > z > \frac{D}{2} \quad (110)$$

The phase match condition $(K_p^2 - \kappa_p^2)^{1/2} + (K_i^2 - \kappa_i^2)^{1/2} = (K_s^2 - \kappa_s^2)^{1/2}$ and the approximation $(K^2 - \kappa^2)^{1/2} \approx K - \frac{\kappa^2}{2K}$ are used to arrive at Eq. (110). The angular spectrum of the sum-frequency field beyond the exit surface of crystal is

$$\begin{aligned} \mathcal{E}_{s-s, z} = i \frac{2\pi\omega_s T_i T_p T_s d\mathcal{E}_p D}{c(n_s n_i)^{1/2}} \frac{\sin(\frac{\Delta KD}{2})}{(\frac{\Delta KD}{2})} e^{-i\frac{\Delta KD}{2}} \\ \cdot e^{i[(K_s - \frac{\kappa_s^2}{2K_s})D + K_{ia}(s - \frac{D}{2}) + (K_{pa} - \frac{\kappa_s^2}{2K_{pa}})(p - \frac{D}{2}) - \underline{\kappa}_s \cdot \underline{\rho}_p + (K_{sa} - \frac{\kappa_s^2}{2K_{sa}})(z - \frac{D}{2})]} \\ \cdot \int d\underline{\kappa}' \mathcal{E}_i(\underline{\kappa}', -s) e^{i[\underline{\kappa}'^2(\frac{s - \frac{D}{2}}{2K_{ia}} + \frac{p - \frac{D}{2}}{2K_{pa}}) - \underline{\kappa}' \cdot (\frac{p - \frac{D}{2}}{K_{pa}} \underline{\kappa}_s + \underline{\rho}_p)]} \\ \cdot \int d\underline{\kappa}' \mathcal{E}_i(\underline{\kappa}', -s) e^{i[\underline{\kappa}' \cdot (\underline{\rho}_p - \underline{\rho}_i + \frac{p - \frac{D}{2}}{K_{pa}} \underline{\kappa}_s) - [\frac{s - \frac{D}{2}}{2K_{ia}} + \frac{p - \frac{D}{2}}{2K_{pa}}] \underline{\kappa}'^2]} \end{aligned} \quad z > \frac{D}{2} \quad (111)$$

Above expression may be evaluated analytically for a few simple object angular spectrum $\mathcal{E}_i(\underline{\kappa}_i, -s)$. The most interesting case is one in which

$$\mathcal{E}_i(\underline{\kappa}_i, -s) = \mathcal{E}_i e^{-i\underline{\kappa}_i \cdot \underline{\rho}_i}$$

Above is angular spectrum of a point object located at the point $(\underline{\rho}_i, -s)$.

The integral

$$I = \int d\underline{\kappa}' \exp\{i[\underline{\kappa}' \cdot (\underline{\rho}_p - \underline{\rho}_i + \frac{p - \frac{D}{2}}{K_{pa}} \underline{\kappa}_s) - [\frac{s - \frac{D}{2}}{2K_{ia}} + \frac{p - \frac{D}{2}}{2K_{pa}}] \underline{\kappa}'^2]\}$$

can be calculated by using the relation

$$\int e^{ibx^2} e^{-iax} dx = \left(\frac{\pi}{ib}\right)^{1/2} e^{i(a^2/4b)}$$

and

$$I=i \left[\frac{\frac{D}{2}}{2K_{ia}} + \frac{\frac{D}{2}}{2K_{pa}} \right] \exp i \left[\frac{\left(x_p - x_i + \frac{p-D}{2} \frac{\kappa_{sx}}{K_{pa}} \right)^2 + \left(y_p - y_i + \frac{p-D}{2} \frac{\kappa_{sy}}{K_{pa}} \right)^2}{4 \left(\frac{s-D}{2K_{ia}} + \frac{p-D}{2K_{pa}} \right)} \right] \quad (112)$$

We let $x_p = y_p = 0$ for simplicity in following calculation. The angular spectrum of image field produced by a point object and a point pump becomes

$$\begin{aligned} \delta_s(\kappa_s, z) = \delta_s \exp i \left[\left(K_s - \frac{\kappa_s^2}{2K_s} \right) D + K_{ia} \left(s - \frac{D}{2} \right) + \left(K_{pa} - \frac{\kappa_s^2}{2K_{pa}} \right) \left(p - \frac{D}{2} \right) - \frac{\Delta KD}{2} \right. \\ \left. + \left(K_{sa} - \frac{\kappa_s^2}{2K_{sa}} \right) \left(z - \frac{D}{2} \right) + \frac{\left(x_i - \frac{p-D}{2} \frac{\kappa_{sx}}{K_{pa}} \right)^2 + \left(y_i - \frac{p-D}{2} \frac{\kappa_{sy}}{K_{pa}} \right)^2}{2 \left(\frac{s-D}{K_{ia}} + \frac{p-D}{K_{pa}} \right)} \right] \quad (113) \end{aligned}$$

where

$$\delta_s = - \frac{4\pi\omega_s T_i T_p T_s dD \delta_i \delta_p}{c(n_s n_i)^{1/2} \left(\frac{s-D}{K_{ia}} + \frac{p-D}{K_{pa}} \right)} \frac{\sin\left(\frac{\Delta KD}{2}\right)}{\left(\frac{\Delta KD}{2}\right)} \quad (114)$$

The phase factor that depends on κ_s is found to be

$$\Phi(\kappa_s) = -\frac{\kappa_s}{2} \left[\frac{z - \frac{D}{2}}{K_{sa}} + \frac{D}{2K_s} + \frac{p - \frac{D}{2}}{K_{pa}} + \frac{D}{2K_M} - \frac{(p - \frac{D}{2})^2 / K_{pa}^2}{\left(\frac{s - \frac{D}{2}}{K_{ia}} + \frac{p - \frac{D}{2}}{K_{pa}} \right)} \right]$$

$$- \kappa_{sx} \left[\frac{\frac{D\zeta}{2} + \frac{x_i (p - \frac{D}{2}) / K_{pa}}{\left(\frac{s - \frac{D}{2}}{K_{ia}} + \frac{p - \frac{D}{2}}{K_{pa}} \right)} \right] - \frac{\kappa_{sy} y_i (p - \frac{D}{2}) / K_{pa}}{\left(\frac{s - \frac{D}{2}}{K_{ia}} + \frac{p - \frac{D}{2}}{K_{pa}} \right)}$$

If we neglect anisotropy factor ζ and let $x_i = y_i = 0$, we obtain an equation relating the image location ($z = -s'$) to the positions of point pump and point object.

$$\frac{-s' - \frac{D}{2}}{K_{sa}} + \frac{D}{2} \left(\frac{1}{K_s} + \frac{1}{K_M} \right) + \frac{(s - \frac{D}{2})(p - \frac{D}{2}) / K_{pa} K_{pi}}{\left(\frac{s - \frac{D}{2}}{K_{pi}} + \frac{p - \frac{D}{2}}{K_{pa}} \right)} = 0 \quad (116)$$

where $z = -s'$ makes $\Phi(\kappa_s) = 0$

For an infinitesimally thin material $D = 0$ and we obtain

$$\frac{K_{sa}}{s'} - \frac{K_{ia}}{s} = \frac{K_{pa}}{p} \quad (117)$$

Since $K_j = n_j K_{ja}$ (where $j = s, i, p$)

We may rewrite Eq. (117) in the form

$$\frac{K_s}{s'n_s} - \frac{K_i}{sn_i} = \frac{K_p}{pn_p}$$

and recognizing $\beta = K_i/K_s$ and $K_p/K_s = 1-\beta$ we obtain

$$\frac{1}{s'n_s} - \frac{\beta}{sn_i} = \frac{1-\beta}{pn_p} \quad (118)$$

This relation is identical to Eq. (6) of Chapter 2.

Longitudinal spread of the upconverted image by anisotropic nonlinear crystal with finite thickness is again apparent from lack of unique solution $z = -s'$ that makes Eq. (115) identically zero for all $\underline{\kappa}_s$. The effect of off-axis waves is accounted by terms which are linear in the transverse object vector $\underline{\rho}_i$ in Eq. (115). This effect leads for thickness coma of upconverted image.

If $\zeta = 0$ and $K_s = K_M = \text{constant}$, a good approximation for near isotropic material, Eq. (116) can be reduced to

$$\frac{1}{(s' + \frac{D}{2})n_s - D} - \frac{\beta}{(s - \frac{D}{2})n_i} = \frac{1-\beta}{(p - \frac{D}{2})n_p} \quad (119)$$

Above equation is equal to Eq. (22) of Chapter 2 if we set $t = \frac{D}{2}$ in latter equation. It is tempting to conclude from the result that a point object at $z = -s$ produces a point image at the sum-frequency at the point $z = -s'$ if crystal anisotropy and mismatch are negligibly small. This conclusion is in error because the condition $K_s = K_M = \text{constant}$ does not imply the matching condition $\Delta K \approx 0$. Under the matched isotropic operating condition, uncertainty in the location of stationary phase plane is introduced through κ_s dependence of K_s . In the geometric optics theory, we attributed thickness aberration as a consequence of interference of sum-frequency fields radiated from each differential slab of polarization wave. It is, however, shown in this chapter that the real causes of thickness aberration are mismatch and crystal anisotropy.

We shall next evaluate the image field of a on-axis point object under the assumption $\xi = 0$. We also assume that Eq. (119) is the stationary plane. The angular spectrum of image field then follows from Eq. (114)

$$\mathcal{G}_s(\kappa_s, -s') = E_s \frac{\sin(\frac{\Delta K D}{2})}{(\frac{\Delta K D}{2})} \quad (120)$$

where

$$E_s = - \frac{\omega_s T_i T_p T_s d D E_i E_p}{4\pi^3 c(n_s n_i)^{1/2} (\frac{s - \frac{D}{2}}{K_{ia}} + \frac{p - \frac{D}{2}}{K_{pa}})}$$

and

$$\Delta K = K_{sz} - K_M \approx - \frac{\kappa_s^2 n_s^2 (s' + \frac{D}{2})^2}{2K_M^2} \left[\frac{K_p}{n_p^2 (p - \frac{D}{2})^2} + \frac{K_i}{n_i^2 (s - \frac{D}{2})^2} \right]$$

$$\Delta K = - \frac{\kappa_s^2 n_s^2 (s' + \frac{D}{2})^2}{2K_M} \left[\frac{1-\beta}{n_p^2 (p - \frac{D}{2})^2} + \frac{\beta}{n_i^2 (s - \frac{D}{2})^2} \right] \quad (121)$$

(See appendix F)

The electric field distribution of image field is given by (Appendix E)

$$E_s(\rho, -s') = E_s \frac{2K_M}{n_s^2 (s' + \frac{D}{2})^2} \frac{1}{\frac{1-\beta}{n_p^2 (p - \frac{D}{2})^2} + \frac{\beta}{n_i^2 (s - \frac{D}{2})^2}} \quad (122)$$

$$\left\{ \frac{\pi}{2} - \text{Si} \left[\frac{\rho^2}{n_s^2 (s' + \frac{D}{2})^2} \cdot \frac{K_M}{\frac{1-\beta}{n_p^2 (p - \frac{D}{2})^2} + \frac{\beta}{n_i^2 (s - \frac{D}{2})^2}} \right] \right\} \quad (122)$$

It is apparent that the point spread function Eq. (122) depends on location of the point pump and the point object. This result agrees with the result of the geometric optics theory.

III-3 GAUSSIAN BEAM PUMPED SYSTEM

We consider the system in which the nonlinear crystal is placed in the near field of the fundamental TEM₀₀ mode of a laser output beam. The electric field distribution of this beam is Gaussian and the diffraction is minimum. According to theory the radial distribution of electric field of the fundamental mode is ⁽²⁸⁾,

$$E(\rho, z) = E_0 e^{-\rho^2/w^2} / (1 + \xi^2)^{1/2} \quad (123)$$

where $E_0 = \text{constant}$. The spot size at distance z is given by

$$w = a(1 + \xi^2)^{1/2}$$

where ξ is the normalized longitudinal distance from the beam focus. At the beam focus the spot size is minimum and is denoted by a . When the nonlinear crystal is placed in the near field $\xi \gg 1$ and the beam is nearly parallel. The pump electric field distribution just inside the entrance surface of the material, for the case considered, is given by

$$E_p(\rho, -\frac{D}{2}) = E_0 e^{-\rho^2/a^2} \quad (124)$$

The angular spectrum of pump field is

$$\delta_p(\kappa_p, -\frac{D}{2}) = a^2 \delta_p e^{-(a^2 \kappa_p^2/4)} \quad (125)$$

The angular spectrum $z = -\frac{D}{2}$ of object field emanating from $z = -s$ is again

$$\delta_i(\kappa_i, -\frac{D}{2}) = T_i \delta_i(\kappa_i, -s) e^{i(K_{ia}^2 - \kappa_i^2)^{1/2}(s - \frac{D}{2})}$$

Then the angular spectrum of polarization wave inside the crystal becomes

$$\begin{aligned} \varphi(\underline{\kappa}_S, z) = & a^2 \mathcal{E}_p dT_i e^{i[(K_S - \frac{\kappa_S^2}{2K_S})(z + \frac{D}{2}) + K_{ia}(s - \frac{D}{2})]} \\ & \cdot \int \mathcal{E}_i(\underline{\kappa}_S = \underline{\kappa}_p, -s) e^{-\frac{a^2 \kappa_p^2}{4}} e^{-a^2 \kappa_p^2 / 4} e^{-i(K_S - \kappa_p)^2 (s - \frac{D}{2}) / 2K_{ia}} d\kappa_p \end{aligned} \quad (126)$$

The angular spectrum of the upconverted image field is obtained following Eq. (69) and (97)

$$\begin{aligned} \mathcal{E}_S(\kappa_S, z) = & i \frac{2\pi a^2 \mathcal{E}_p T_i T_S dD \omega_S}{c(n_S n_i)^{1/2}} e^{i[(K_S - \frac{\kappa_S^2}{2K_S})D + (K_{Sa} - \frac{\kappa_S^2}{2K_{Sa}})(z - \frac{D}{2})} \\ & - \frac{\Delta KD}{2} + K_{ia}(s - \frac{D}{2})] \\ & \cdot \frac{\sin(\frac{\Delta KD}{2})}{(\frac{\Delta KD}{2})} \int \mathcal{E}_i(\kappa_S - \kappa', -s) e^{-\left(\frac{a^2 \kappa'^2}{4}\right)} e^{-i\left[\frac{(\kappa_S - \kappa')^2}{2K_{ia}}\right](s - \frac{D}{2})} d\kappa' \\ & z > \frac{D}{2} \end{aligned} \quad (127)$$

For a point object located at the point $(\underline{\rho}_i, -s)$, the angular spectrum of the image field is

$$\begin{aligned} \mathcal{E}_S(\kappa_S, z) = & i \frac{2\pi a^2 \mathcal{E}_p \mathcal{E}_i T_i T_S dD \omega_S}{c(n_S n_i)^{1/2}} \frac{\sin(\frac{\Delta KD}{2})}{(\frac{\Delta KD}{2})} e^{i[K_S D + (K_{ia} - \frac{\kappa_S^2}{2K_{ia}})(s - \frac{D}{2})} \\ & + (K_{Sa} - \frac{\kappa_S^2}{2K_{Sa}})(z - \frac{D}{2})] e^{-i\left(\frac{\Delta KD}{2}\right)} e^{-i(\underline{\rho}_i \cdot \underline{\kappa}_S)} \cdot I \end{aligned} \quad (128)$$

where integral I is given by

$$I = \int e^{\left[-\left(\frac{a^2}{4} + i\frac{s-D/2}{2K_{ia}}\right)k^2 + i\left(\rho_i - \frac{s-D/2}{K_{ia}}\right)k_s\right]} dk$$

Using $\int e^{-bx^2} e^{iax} dx = \sqrt{\frac{\pi}{b}} e^{-a^2/4b}$, we have

$$I = \frac{\pi}{\frac{a^2}{4} + i\frac{s-D/2}{2K_{ia}}} \exp \left\{ \frac{-1}{a^2 + \frac{2(s-D/2)}{K_{ia}}} \left[\left(x_i - \frac{s-D/2}{K_{ia}} k_{sx} \right)^2 + \left(y_i - \frac{s-D/2}{K_{ia}} k_{sy} \right)^2 \right] \right\}$$

When $\rho_i = 0$ and $a^2 \gg \frac{2(s-D/2)}{K_{ia}}$ which corresponds to the Fresnel zone of

Gaussian aperture, the expression for the angular spectrum of upconverted image field becomes.

$$\begin{aligned} \delta_s(\kappa_s, z) = & \frac{i8\pi\delta_p\delta_i T_s T_i dD\omega_s}{c(n_s n_i)^{1/2}} \frac{\sin\left(\frac{\Delta KD}{2}\right)}{\left(\frac{\Delta KD}{2}\right)} e^{-\left[(s-D/2)k_s/aK_{ia}\right]^2} \\ & \cdot e^{i\Phi(\kappa_s)} e^{i\left[\frac{K_s D}{2} + K_{ia}\left(s - \frac{D}{2}\right) + K_{sa}\left(z - \frac{D}{2}\right) + \frac{K_M D}{2}\right]} \end{aligned} \quad (129)$$

where

$$\begin{aligned} \Phi(\kappa_s) = & -\frac{\kappa_s^2}{2} \left(\frac{z}{k_{sa}} - \frac{D}{2K_{sa}} + \frac{D}{2K_s} + \frac{D}{2K_M} - \frac{D}{2K_{ia}} + \frac{s}{K_{ia}} \right) \\ & - \frac{\kappa_{sx}^2 D}{2} \end{aligned}$$

Above equation is identical to Eq. (100) obtained for plane wave pump case.

The discussion on aberration for plane wave pump system, therefore,

directly apply to the Gaussian wave pump system. The effect of Gaussian

field distribution appears as an attenuation factor $\exp\left[-\left(s - \frac{D}{2}\right)^2 \frac{\kappa^2}{a^2 K_{1a}^2}\right]$

It can be shown that Eq. (129) becomes equal to Eq. (98), if the Gaussian attenuation factor $\exp\left[-\left(\frac{s - \frac{D}{2}}{a K_{1a}} \kappa\right)^2\right]$ is neglected in Eq. (129) and $\delta_i(\kappa_s, -s)$ in Eq. (98) is set equal to δ_i , which is Fourier component of point object located at $\rho_i = 0$ and $z = -s$. This indicates that the Gaussian beam pumped upconverter can be considered to be equivalent to the plane

wave pumped system if $\left(s - \frac{D}{2}\right) \frac{\kappa}{K_{1a}} \ll a$. The condition $\left(s - \frac{D}{2}\right) \frac{\kappa}{K_{1a}} \ll a$ implies that the beam size of Gaussian pump beam is considerably greater than the interaction aperture determined by the object field of view.

As shown for the plane pump wave case the resolving power of the Gaussian wave pumped system remains constant for the range

$a > \left(s - \frac{D}{2}\right) \frac{\kappa}{K_{1a}}$. The resolving power of the Gaussian wave pumped system

would decrease with the beam size for the range $a < \left(s - \frac{D}{2}\right) \frac{\kappa}{K_{1a}}$ due to the Gaussian field distribution.

III-4 FINITE INTERACTION APERTURE

Finite interaction aperture resulting from the finite transverse dimension of the material can be accounted for by introducing aperture function

$$B(\underline{\rho}, -\frac{D}{2}) = \begin{cases} 1 & \rho \text{ in } A \\ 0 & \rho \text{ outside } A \end{cases} \quad (130)$$

If we express pump field at $z = -\frac{D}{2}$ by $E_p(\underline{\rho}, -\frac{D}{2})$ then

effective pump field distribution is

$$E_p^{\text{eff}} = E_p(\underline{\rho}, -\frac{D}{2}) B(\underline{\rho}, -\frac{D}{2}) \quad (131)$$

The angular spectrum of effective pump field is,

$$\mathcal{E}_p^{\text{eff}}(\underline{\kappa}_p, -\frac{D}{2}) = \mathcal{E}_p(\underline{\kappa}_p, -\frac{D}{2}) \otimes \mathcal{B}(\underline{\kappa}_p, -\frac{D}{2}) \quad (132)$$

where $\mathcal{B}(\underline{\kappa}_p, -\frac{D}{2})$ is angular spectrum of aperture function Eq. (130).

Similarly the angular spectrum of effective object field is given by

$$\mathcal{E}_i^{\text{eff}}(\underline{\kappa}_i, -\frac{D}{2}) = \mathcal{E}_i(\underline{\kappa}_i, -\frac{D}{2}) \otimes \mathcal{B}(\underline{\kappa}_i, -\frac{D}{2}) \quad (133)$$

The introduction of a finite interaction aperture due to the material dimension or other aperture stops has the effect of broadening the angular spectrum of both pump and object field disturbance. The smaller the aperture, the broader the angular spectrum. Since angular spectrum of the sum-frequency image field is proportional to convolution of Eq. (132) and (133), image angular spectrum will be a function of convolution of aperture spectrum; $\mathcal{B} \otimes \mathcal{B}$. This indicates that the effective aperture for the sum-frequency field is smaller than the material aperture A. For the case of uniform illuminated plane-wave interaction, the effective interaction area for the sum-frequency field is one half of the material aperture. This effect has also been pointed out by Boyd and Ashkin. ⁽²⁹⁾

$$B(\underline{\rho}, -\frac{D}{2}) = \begin{cases} 1 & \rho \text{ in } A \\ 0 & \rho \text{ outside } A \end{cases} \quad (130)$$

If we express pump field at $z = -\frac{D}{2}$ by $E_p(\underline{\rho}, -\frac{D}{2})$ then

effective pump field distribution is

$$E_p^{\text{eff}} = E_p(\underline{\rho}, -\frac{D}{2}) B(\underline{\rho}, -\frac{D}{2}) \quad (131)$$

The angular spectrum of effective pump field is,

$$\mathcal{S}_p^{\text{eff}}(\underline{\kappa}_p, -\frac{D}{2}) = \mathcal{S}_p(\underline{\kappa}_p, -\frac{D}{2}) \otimes \mathcal{B}(\underline{\kappa}_p, -\frac{D}{2}) \quad (132)$$

where $\mathcal{B}(\underline{\kappa}_p, -\frac{D}{2})$ is angular spectrum of aperture function Eq. (130).

Similarly the angular spectrum of effective object field is given by

$$\mathcal{S}_i^{\text{eff}}(\underline{\kappa}_i, -\frac{D}{2}) = \mathcal{S}_i(\underline{\kappa}_i, -\frac{D}{2}) \otimes \mathcal{B}(\underline{\kappa}_i, -\frac{D}{2}) \quad (133)$$

The introduction of a finite interaction aperture due to the material dimension or other aperture stops has the effect of broadening the angular spectrum of both pump and object field disturbance. The smaller the aperture, the broader the angular spectrum. Since angular spectrum of the sum-frequency image field is proportional to convolution of Eq. (132) and (133), image angular spectrum will be a function of convolution of aperture spectrum $\mathcal{B} \otimes \mathcal{B}$. This indicates that the effective aperture for the sum-frequency field is smaller than the material aperture A . For the case of uniform illuminated plane-wave interaction, the effective interaction area for the sum-frequency field is one half of the material aperture. This effect has also been pointed out by Boyd and Ashkin. ⁽²⁹⁾

CHAPTER 4 SENSITIVITY OF IMAGE UPCONVERSION SYSTEM

I. INTRODUCTION

An important consideration in defining the performance of any image system is the sensitivity. One way of describing the sensitivity is noise-equivalent-power (NEP) per single picture element. This is a useful criterion of some devices and it is usually a true measure of sensitivity that does not depend on the optics of system, exposure time, and amount of detail in the reproduced image⁽³¹⁾. Another way of comparing sensitivities is in terms of the threshold scene radiance⁽³¹⁾. Threshold scene radiance depends explicitly upon the exposure time, system optics, and the image detail.

The sensitivity, as expressed by NEP, of photoelectronic image tubes and photographic films considered by themselves is only a function of quantum efficiency of photosensitive surface and/or noise due to dark leakage and the amplifier which follows the photo-sensitive device. NEP of the image system utilizing parametric upconversion process is, however, implicitly dependent upon amount of image detail as is shown by the following consideration. For a given pump power, set either by available laser power output or by the power handling capacity of the nonlinear material, attainable conversion efficiency of upconversion process depends on the interaction aperture. Number of resolution elements of the diffraction limited image upconverter increases with the interaction area. Conversion efficiency of upconversion is inversely proportional to the interaction area. It then follows that the conversion efficiency decreases as more detail is required in the reproduced image. The reduction in conversion efficiency directly leads to increase in NEP. Sensitivity of the image upconverter expressed in terms of NEP is,

therefore, no more true than the sensitivity description in terms of threshold scene radiance. The NEP criterion is for a single picture element and is defined for unity signal-to-noise ratio, therefore it can not be used to discuss the system that must see half tone pictures. The NEP criterion is normalized for unit bandwidth or unit observation time and hence it is independent of exposure time. The above considerations suggests the desirability of expressing the system sensitivity in a more intrinsic fashion so that the threshold scene radiance, image detail including resolution and contrast, conversion efficiency, and the interaction aperture would be related to some universal constant. It is the purpose of this chapter to obtain a characterization of the image upconversion system which will involve both sensitivity and picture detail. Specific attention is paid to the system using a combination of an upconverter and a photoelectronic image recording device.

An equation characterizing of an ideal image upconversion system consisting of a quantum noise limited upconverter and a perfect picture pick-up device is derived in Section II. The threshold quantum number of the photoelectron camera tubes is considered in Section III. Threshold quantum number of picture tubes is defined as minimum required photo quanta per picture element per integration time to produce signal-to-noise ratio of unity at the output. The characteristic equation of a practical upconversion system using an imperfect pick-up device is also considered in Section III. Finally the NEP expression is presented in Section IV.

II. CHARACTERISTIC EQUATION OF AN IDEAL IMAGE UPCONVERTER SYSTEM (QUANTUM FLUCTUATION LIMITED PERFORMANCE)

Consider a square element of area of side length "a" on the up-converted image. It is assumed that a picture pickup device, with an ideal

photosensitive surface, is used to record the upconverted image. By "ideal" is meant that the photosensitive surface will record single incident quantum. Let this element of area a^2 absorb on the average Q_s quanta of wavelength λ_s in the exposure time t allotted. Because at a room temperature the absorption of near infrared and visible photo quanta obeys Poission statistics^(32, 33), the average absorption number Q_s will have associated with it deviations from the average whose root mean square value is $Q_s^{1/2}$. This deviation set a limit to the accuracy with which the average number Q_s may be determined. The smallest change in Q_s which can be detected is, therefore, of the order of $Q_s^{1/2}$.

Next consider two adjacent square elements A and B. The difference in average number of quanta arriving at these two elements can be distinguished provided:

$$(Q_{SA} - Q_{SB}) \geq \frac{(Q_{SA} + Q_{SB})/2}{\sqrt{(Q_{SA} + Q_{SB})/2}} = [(Q_{SA} + Q_{SB})/2]^{1/2}$$

This relation, indicates that the smallest intensity difference between adjacent two elements (denoted by ΔQ) which can be detected is also of order of the statistical fluctuations $Q_s^{1/2}$, where Q_s is an average quantum flux.

The irradiance H_s , in watt/cm², is related to Q_s in the following way

$$H_s = \frac{h\nu_s Q_s}{a^2 t} \quad (134)$$

We can now introduce the threshold contrast C_{th} as

$$C_{th} = \frac{H_{SA} - H_{SB}}{H_{SA}} = \frac{Q_{SA} - Q_{SB}}{Q_{SA}}$$

For most of any application $H_{SA} \approx H_{SB} \approx H_S$, therefore

$$C_{th} = \frac{\Delta Q_S}{Q_S} \sim Q_S^{-1/2} \quad (135)$$

From (134) and (135)

$$H_S \sim \frac{1}{C_{th}^2 a^2}$$

or

$$H_S C_{th}^2 \alpha^2 = \text{const.} \quad (136)$$

where α is the angle subtended by the element a^2 at the nonlinear crystal. (Fig. 14)

Radiance H_i of the infrared object which is upconverted is proportional to the image irradiance H_S , since the input electric field (power density) and the output electric field (power density) are linearly related and the upconversion process is noiseless⁽³⁷⁾. Eq. (136), therefore, can be rewritten as:

$$H_i C_{th}^2 \alpha^2 = \text{const} \quad (137)$$

Eq. (137) is the characteristic equation of an ideal image upconverter system. The constant term on the right depends on the particular system under consideration. The meaning of Eq. (137) is this: let any two of the quantities (H_i, C_{th}, α) be specified, then Eq. (137) sets the threshold value for the third.

To evaluate the constant term on the right of Eq. (137), we consider the upconverter system shown in Figure 14.

NON-LINEAR CRYSTAL
(QUANTUM CONVERSION
EFFICIENCY = η)

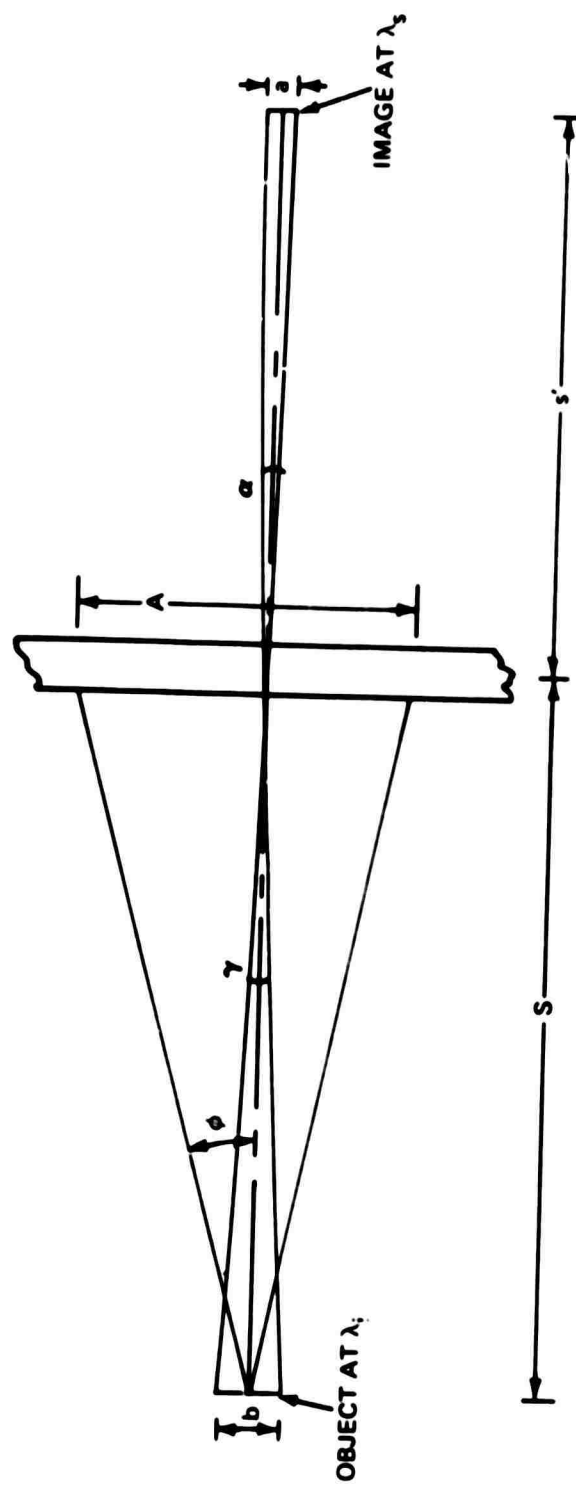


FIGURE 14. GEOMETRIC RELATION USED TO OBTAIN CHARACTERISTIC EQUATION OF THE IMAGE UPCONVERTER

To simplify the analysis the following assumptions were made:

- 1) The thickness of the nonlinear material is very small compared to other parameters, such as object and image locations, so that aberrations due to finite thickness are negligible.
- 2) Phase mismatch factor for all interacting rays is negligibly small so that the conversion efficiency is constant over whole angular aperture. This assumption implies that the angle subtended by the infrared object at the converter is very small compared to the field of view of the system. It also assures that all rays considered are paraxial and small angle approximation can be used.

If the object radiance is such that N_i quanta at the wavelength λ_i are radiated per unit area per unit time, the total number of quanta radiated by the infrared element with the side length "b" for exposure time t will be $N_i b^2 t$. Of this number only a fraction will be intercepted by the nonlinear crystal of active aperture diameter A situated distance s from the infrared object. The infrared quanta intercepted by the nonlinear crystal in time t is, for a Lambert distribution equal to $N_i b^2 t \sin^2 \phi$, where 2ϕ is the angle subtended by the nonlinear crystal at the object. These amount of quanta will interact with the pump quanta and together generate quanta at wavelength λ_s . The number of quanta Q_s generated at wavelength λ_s is given by

$$Q_s = \eta N_i b^2 t \sin^2 \phi \quad (138)$$

Where η is photon (quantum) conversion efficiency of the upconversion process and is assumed to be a constant for a given system.

All generated quanta Q_s will be directed and focused on the element of area a^2 at distance S' from the nonlinear crystal. From the geometry of Figure 14 and small angle approximation,

$$\sin \phi \approx \tan \phi = \frac{A}{2S} \quad (139)$$

Transverse magnification factor a/b is obtained in Chapter 2 as

$$\frac{a}{b} = \frac{\beta n_s S'}{n_i S} \quad (140)$$

where n_s and n_i are indices of refraction of nonlinear material at λ_s and λ_i respectively.

β is the angular demagnification factor defined in Chapter 2.

Substituting Eq. (139) and Eq. (140) in Eq. (138), Q_s become

$$Q_s = N_i t\eta \left(\frac{n_i A}{2\beta n_s} \right)^2 \alpha^2 \quad (141)$$

where $\alpha = \frac{a}{S}$, is the angle subtended by the element of area a^2 at the nonlinear crystal.

Using the relation $H_i = h\nu_i N_i$ we obtain from Eq. (141)

$$H_i = \frac{h\nu_i}{t\eta\alpha^2} \left(\frac{2\beta n_s}{n_i A} \right)^2 Q_s \quad (142)$$

Combining Eq. (134) and Eq. (142), we obtain the characteristic equation:

$$H_i C_{th}^2 \alpha^2 = \frac{4h\nu_i}{t\eta A^2} \left(\frac{\beta n_s}{n_i} \right)^2 \quad (143)$$

Threshold contrast C_{th} defined in Eq. (134) is over the upconverted image field, but it also represents threshold contrast of infrared object because of the linearity of the upconversion process. The angular size α in the left hand of Eq. (143) is for the upconverted image. From Eq. (140) the angular size γ of the infrared object element is related to α by

$$\alpha = \gamma \frac{n_s}{n_i}$$

The final form of the characteristic equation which describes the ideal performance of an image upconversion system is then

$$H_i C_{th}^2 \gamma^2 = \frac{h\nu_i}{t\eta\left(\frac{A}{2}\right)^2} \quad (144)$$

or

$$H_i C_{th}^2 \gamma^2 t\eta\left(\frac{A}{2}\right)^2 = h\nu_i$$

The six parameters needed to specify an ideal system are in left hand of Eq. (144). When any five of these are arbitrarily specified, the threshold value for the sixth is given by Eq. (144). It should be made clear at this point that the parameters γ , η , and A can not be arbitrarily specified independently from one another as will be shown later.

III. PERFORMANCE OF A NON-IDEAL IMAGE UPCONVERTER SYSTEM

The characteristic equation (114) describing the performance of an ideal image upconverter system was obtained by assuming:

- 1) Upconversion process is noiseless⁽³⁷⁾

- 2) All the radiation intercepted by the photosensitive surface of the pickup device arises from the radiation coming from the object. - i.e. no background noise
- 3) A noise-free image detector

The second assumption of background noise-free condition is usually met in practice since the background thermal radiation at the sum-frequency and signal frequency wavelength is small enough to be neglected at room temperature. The pump radiation, whose wavelength is very close to the sum-frequency wavelength, can practically be eliminated by interference filters. The use of optical filters in the system attenuates the sum-frequency radiation. In the following discussion this loss will be treated by considering the filters as an integral part of the image detector. A noise-free image detector is not achievable at present, i.e. the photosensitive surface requires more than one quanta to record incoming information. An equation describing the performance of a practical image upconverter system must therefore include the properties of the image detector.

Any image detecting device, such as a photoelectronic camera tubes, a photographic film and even the human eye can be used in a practical image upconverter system. In the following, we shall consider specifically the sensitivity of photoelectronic picture reproducing devices.

If the target of a photoelectronic pick-up system is read off by means of a scanning electron beam with frame time t_o , and if the number of picture elements is M , the sampling time τ of each picture element is τ_o/M . We will assume that the highest frequency in the image signal will be roughly $F \approx 1/2 \tau$, where τ is the picture element sampling (dwell) time. If the average number of photo-quanta absorbed in one picture element

of area a^2 between storage time intervals t is \bar{Q}_s and the quantum efficiency of the target is σ , an electron charge $\sigma \bar{Q}_s e$ is stored in a picture element between two scans*. Since this charge will be read off in time τ , the average signal current \bar{i}_s for one picture element

$$\bar{i}_s = \frac{\sigma \bar{Q}_s e}{\tau} \quad (145)$$

The shot noise associated with this signal current is^(33, 34)

$$(\overline{\Delta i_s})^2 = 2 e \bar{i}_s F \quad (146)$$

If it is necessary to amplify the signal, the noise current of the first amplifier, $(\overline{\Delta i_A})^2$ and thermal noise of the amplifier input resistance $(\overline{\Delta i_R})^2$ have to be added to the shot noise. In general, the dark current noise, $(\overline{\Delta i_d})^2$, generated either by thermal origin, charge leakage, or scanning beam current exists in any pick-up devices, and must be added to the above noise. The total mean squared noise current of the system is, therefore, given by

$$(\overline{\Delta i_n})^2 = b(\overline{\Delta i_s})^2 + (\overline{\Delta i_d})^2 + (\overline{\Delta i_R})^2 + (\overline{\Delta i_A})^2 \quad (147)$$

The constant b is introduced in above expression to take into account of noise figure of the pickup tubes⁽³⁴⁾. The signal-to-noise ratio is then given by

$$\frac{S}{N} = \frac{\bar{i}_s}{\sqrt{(\overline{\Delta i_n})^2}} \quad (148)$$

* The storage time interval t is not in general equal to the frame time interval t_o .

The threshold quantum number q_s (or noise equivalent quantum input) per picture element per exposure time is defined as that signal which gives rise to a unit signal-to-noise ratio.

We shall next evaluate the threshold quantum number q_s for several different classes of photoelectronic camera tubes.

1. Storage type with electron multiplication

The iconoscope, the image orthicon, the vidicon-multiplier belong to this class⁽³⁵⁾. The electron multiplication is practically noiseless so that the amplifier noise and the noise of signal resistance are negligible compared to other noise^(34, 36). The signal-to-noise ratio for this case becomes

$$\frac{S}{N} = \frac{\bar{i}_s}{\sqrt{(\Delta i_s)^2 + (\Delta i_d)^2}}$$

If the device is quantum noise limited, that is to say $\overline{(\Delta i_s)^2} \gg \overline{(\Delta i_d)^2}$, the signal-to-noise ratio is, using (145) and (146)

$$\frac{S}{N} = \sqrt{\sigma Q_s} . \quad (149)$$

The threshold quantum number q_s is given by

$$q_s = 1/\sigma \quad (150)$$

If the device is dark noise limited, $\overline{(\Delta i_d)^2} \gg \overline{(\Delta i_s)^2}$, the threshold quantum number is given by:

$$q_s = \frac{\tau}{e\sigma} \sqrt{\overline{(\Delta i_d)^2}} \quad (151)$$

2. Storage type with an amplifier

The vidicon and the orthicon belong to this class. In these devices there is no direct photoelectronic multiplication⁽³⁵⁾. The amplifier noise and the signal resistance noise are now dominant noise sources and the threshold quantum number is given by:

$$q_s = \frac{\tau}{e\sigma} \sqrt{(\Delta i_R)^2 + (\Delta i_A)^2} \quad (152)$$

3. Nonstorage Type with Multiplier

The image disector tube belongs to this category⁽³⁵⁾. This type is less sensitive than the storage type with electron multiplication, because the photoelectric charge is generated during only a picture element sampling time τ instead of a storage time t .

Let \bar{Q}_s' denotes the average number photo-quanta absorbed per picture element in the sampling (read out) time τ . The average signal current per picture-element is

$$\bar{i}_s = \frac{\sigma e \bar{Q}_s'}{\tau}$$

Fluctuation noise current associated with this current is again

$$\sqrt{(\Delta i_s)^2} = \sqrt{2e\bar{i}_s F} = \sqrt{\frac{e\bar{i}_s}{\tau}}$$

therefore the signal to noise ratio for quantum-limited case, is

$$\frac{S}{N} = \frac{\tau \bar{i}_s}{\sqrt{2e\bar{i}_s F}} = \sqrt{\sigma \bar{Q}_s'}$$

If incoming photon flux remains the same as the previous devices discussed, \bar{Q}_s' is related to \bar{Q}_s by the expression

$$\bar{Q}_s' = \frac{\tau}{t} \bar{Q}_s. \quad (153)$$

so that the signal-to-noise ratio becomes

$$S/N = \sqrt{\frac{\sigma}{M} \bar{Q}_s} \quad (154)$$

where

$$M = \frac{t}{\tau}.$$

From the above we see that the threshold quantum number, q_s , is $\frac{M}{\sigma}$. Therefore the threshold quantum number is greater than that encountered in storage devices by a factor of M .

As shown above, threshold quantum number per picture element per storage time of a photoelectronic camera tube follows two different type of relations depending upon whether it is operating in quantum limited region or amplifier (or dark) noise limited region.

The characteristic equation of a practical image upconverter system can now be derived. The number of quanta at sum-frequency per picture element required to produce unity signal-to-noise ratio is q_s and the corresponding minimum number of quanta at the signal frequency is then q_s/η . The characteristic equation (144), for a practical image upconverter system can now be written as

$$H_i C_{th}^2 \gamma^2 t \left(\frac{A}{2}\right)^2 \frac{\eta}{q_s} = h\nu_i \quad (155)$$

IV. NOISE EQUIVALENT POWER OF AN IMAGE UPCONVERTER

The noise equivalent power of a practical image upconverter system is derived below for comparison with the characteristic equation derived in preceding section. The noise equivalent power of a detection system is defined as the signal input power that gives rise to unit signal-to-noise ratio in unit bandwidth.

Threshold power at sum-frequency per picture element of an image detector with storage time t is equal

$$q_s h \nu_s$$

where q_s = threshold quantum number of the image detector as defined before.

h = Planck's constant.

ν_s = Sum-frequency

threshold power at infrared signal frequency is then

$$q_s h \nu_i / \eta$$

where

η = quantum conversion efficiency

ν_i = infrared signal frequency

The above is the threshold power for a unit signal-to-noise when the IF amplifier bandwidth is $F = \frac{1}{2\tau}$. Since the noise in this type of detector is proportion to the square root of the IF bandwidth, the threshold power for unit bandwidth, i. e. the NEP, is

$$\text{NEP} = \frac{q_s h \nu_i}{\eta \sqrt{F}} \quad (156)$$

where

NEP = noise equivalent power in watt/Hz^{1/2}

$$F = 1/2\tau$$

τ = sampling time per picture element and is related to the frame scan time t_o by

$$\tau = t_o/M$$

where

M = is number of picture element in a picture frame. Quantum conversion efficiency η is inversely proportional to the interaction aperture area.⁽¹⁾

$$\eta = K' / A^2 \quad (157)$$

where

A = diameter of interaction aperture

K' = constant for fixed available pump power

For a diffraction limited image upconversion system the maximum number of picture elements obtainable is, using Rayleigh criteria, given by

$$M = \left(\frac{2 \phi_{\max} A}{1.22 \lambda_i} \right)^2 \quad (158)$$

where

$2 \phi_{\max}$ = is angular aperture of the upconverter.

Quantum conversion efficiency may be expressed in terms of number of picture elements.

$$\eta M = K \quad (159)$$

Above expression is a characteristic equation of diffraction limited image upconversion process.

The constant K is characteristic of a given upconverter depending only on material constant and the pump power and is given by⁽¹⁾

$$K = \frac{44.8 P_p |d_{eff}|^2 D^2 \phi_{max}}{n_i n_p n_s \lambda_s \lambda_i^3} \quad (160)$$

The final expression of NEP is

$$NEP = \frac{h\nu_i q_s}{Kt} \left(\frac{Mt_o}{2} \right)^{1/2} \quad (161)$$

The storage time t and the frame scanning time t_o is not necessarily the same. They are equal for the storage type photo-electronic image device, but they are not equal for nonstorage type pickup tubes.

The NEP of the image upconversion system using a storage type pickup device is therefore

$$NEP = \frac{h\nu_i q_s}{K} \left(\frac{M}{2t_o} \right)^{1/2} \quad (162)$$

The image upconversion system with a nonstorage type pick-up device becomes

$$NEP = \frac{h\nu_i q_s}{K} \frac{M^{3/2}}{(2t_o)}^{1/2} \quad (163)$$

CHAPTER 5 IMAGE UPCONVERSION EXPERIMENTS

I. GENERAL CONSIDERATION

An upconverter using single crystal proustite (Ag_3AsS_3), a Nd:YAG laser, and an infrared $10.6\text{ }\mu\text{m}$ illuminated object as its primary components was used for the image upconversion experiment. The Nd:YAG laser radiating at $1.06\text{ }\mu\text{m}$ was chosen because of its moderate CW power and stable single mode output. The objects were illuminated with the $10.6\text{ }\mu\text{m}$ output of a CW CO_2 gas laser. The $1.06\text{ }\mu\text{m}$ pump radiation and infrared $10.6\text{ }\mu\text{m}$ object radiation were polarized as ordinary and extraordinary waves, respectively. The resulting upconverted image wave at $0.967\text{ }\mu\text{m}$ was polarized as an extraordinary wave. The proustite crystal was prepared in such a way that its two polished faces were nearly perpendicular to the phase-match (near collinear) direction. The angular relations of the crystal optic axis, the crystal surfaces, and the directions of beam propagation that were used for optimum upconversion have been discussed in detail in Section IV-2, Chapter 2.

The quality of an imaging system is usually assessed either by its limiting resolution or by its transfer function. The classical limiting resolution criterion is convenient and easy to apply, but it does not provide the complete quantitative data required to characterize the system. The basic measurement required for the transfer function description of a system is the spread function measurement. Since the spread function of a system is defined as the system response to a delta function input, the Fourier transform of the spread function is the system transfer function. Measurements of spread functions can be performed either in two-dimensions or one-dimension; that is, point or line spread function. The line spread

function technique was chosen for the initial experiments because of approximate symmetry and the ease of implementing the Fourier transform computation of a line spread function to obtain an optical transfer function.

The line spread functions were measured for two types of image upconverter configurations. The first configuration chosen was the Fourier space configuration, in which both the pump and object waves are nearly plane waves. The other system utilizes a Gaussian shaped pump beam and a cylindrical object wave. These measurements were made to obtain data on image location and the amount of optical aberrations. On- and off-axis spread functions of the Fourier space configuration were measured to determine the limiting resolution. The primary consideration in choosing a nearly plane wave pump in the experiment is the small pump acceptance angle of the upconversion process using a proustite crystal. As shown in Chapter 2, the pump angular aperture of the $1.06\text{ }\mu\text{m}$ pumped proustite is less than 0.2 degrees. Effective usage of available pump power, therefore, requires minimum pump beam divergence.

The intensity distribution was measured for the upconverted image of a resolution test bar chart, which was illuminated by $10.6\text{ }\mu\text{m}$ radiation. The data was in rough agreement with the predicted line spread function.

Measurements of the line spread function and the intensity distribution of the test chart image were taken only along the crystallographic a-axis. This is justified because of small birefringence of proustite crystal. Measurements along two orthogonal transverse directions, however, becomes necessary if the crystal anisotropy is appreciable enough to introduce large asymmetry.

The upconverted image of a 10.6 μm illuminated resolution test chart was recorded on photographic film. This result provides a visual display of an upconverted image and agrees with the measurements mentioned above.

II. EXPERIMENTAL ARRANGEMENT

The apparatus shown schematically in Figure 15 was arranged so that the nature of pump and IR object waves may be readily changed with the minimum physical alteration of components. A 2.5 cm in diameter and 0.6 cm thick proustite crystal was used. The crystallographic a-axis lies in the plane of paper and is parallel to the front surface. Its optic axis lies in a plane perpendicular to the paper and makes an angle of 20 degrees with the normal to the polished front and back surfaces. A single mode CW Nd:YAG laser radiating an electric field polarized parallel to the plane of paper was used as a pump source. Four glass lenses, labeled 1, 2, 3, and 4, were placed along the pump beam path so that the apparent location of the source and the beam size can be altered by adjusting the relative positions of those lenses. A CO_2 gas laser radiating with an electric field polarized perpendicular to the plane of paper was used to illuminate the transparent objects. Six BaF_2 lenses, No. 5 through No. 10, were used to obtain the desired illumination and to change the apparent object size and location.

The pump wave and the object wave are combined by a dichroic mirror which has a high reflectance coating for the 1.06 μm pump radiation. The insertion loss of the dichroic mirror to the IR 10.6 μm radiation is about 3 db. The 10.6 μm object field incident on to the proustite crystal is

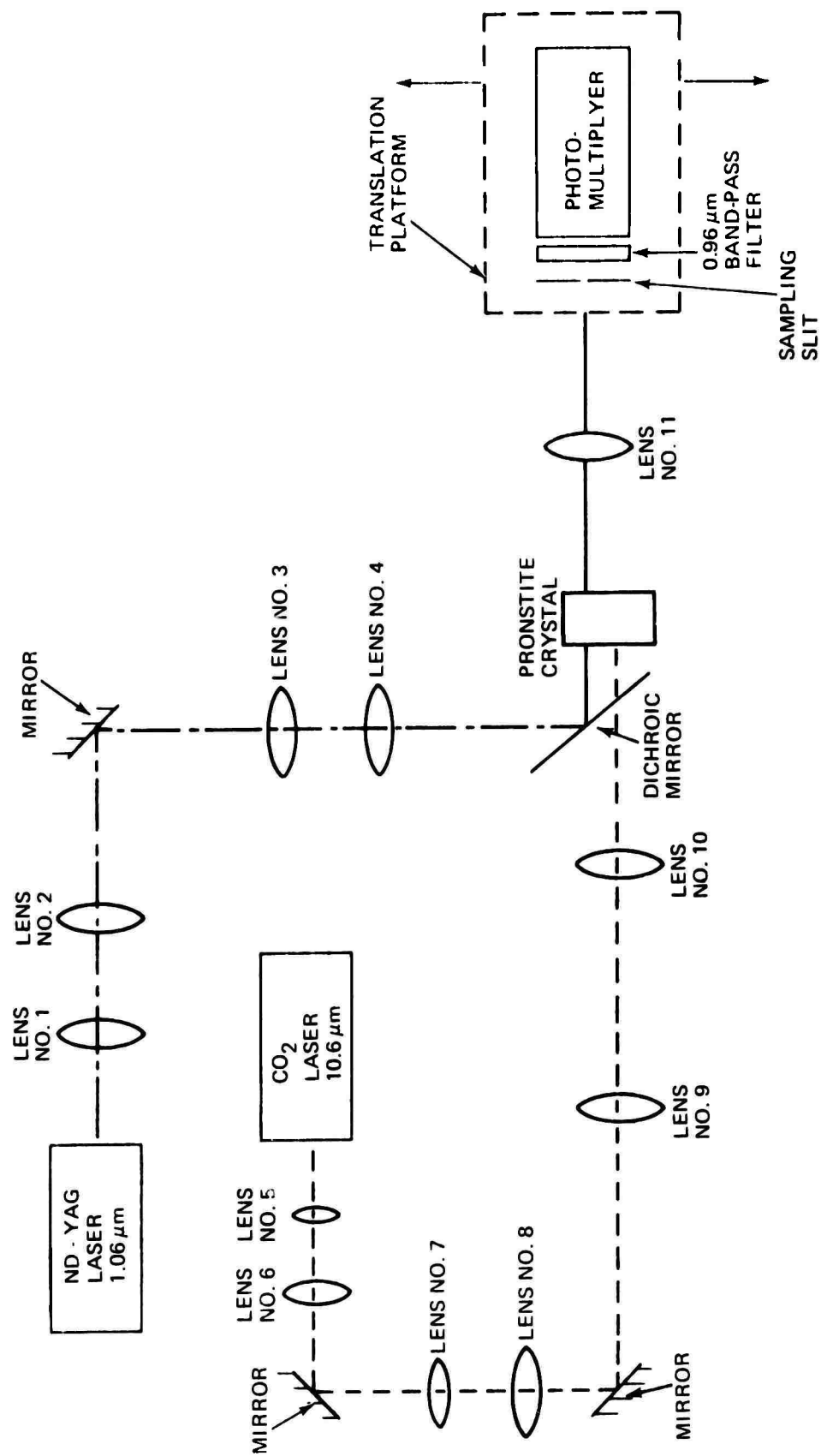


FIGURE 15. EXPERIMENTAL ARRANGEMENT FOR PARAMETRIC IMAGE UPCONVERSION

parametrically upconverted to $0.967\text{ }\mu\text{m}$ image waves. The upconverted image waves are then refocused by the glass lens No. 11 to form a real image. The upconverted real image is recorded by a image pick-up device.

The image pick-up unit consisting of a cooled (60°C) photomultiplier, a $0.96\text{ }\mu\text{m}$ band-pass filter and a narrow sampling slit, forming an integral detection unit, is mounted on a translation platform. The upconverted image is scanned by the sampling slit and the output from the photomultiplier was amplified and fed to the vertical drive of an X-Y recorder. An electrical signal indicating the transverse position of the sampling slit was applied to the horizontal drive of the X-Y recorder.

III. MEASUREMENT OF LINE SPREAD FUNCTIONS

Spherical lenses No. 1 and No. 2 are used as a pump beam expander. They are positioned so that the pump beam focuses at infinity. Magnification of beam size equals to the ratio of focal length of input lens No. 1 to that of output lens No. 2. Beam divergence is reduced also by that factor. The lenses No. 3 and No. 4 were omitted in the line spread function measurement. The spherical lenses No. 5 and No. 6 formed a beam expander for the CO_2 laser output beam. The lenses No. 9 and No. 10 were also omitted in this experiment. The $10.6\text{ }\mu\text{m}$ line source necessary for the measurement was generated by the lenses No. 7 and No. 8 and a narrow slit placed between these lenses. Lenses No. 7 and No. 8 are cylindrical and were oriented such that their surface curvature lies in the plane parallel to the plane of paper. The narrow slit was placed at the focus of lense No. 7 and its long edge was perpendicular to the paper. Width of the slit was adjusted narrower than the beam waist of focused $10.6\text{ }\mu\text{m}$ beam. The position of cylindrical lens No. 8 was adjusted so that the image of the

10.6 μm illuminated slit could be positioned at desired location.

III-1. Results on Fourier Configuration Upconverter

An image upconverter system with a plane pump wave and plane object wave has been shown to be free of thickness aberration. Its limiting resolution is governed by higher order effects such as birefringence, dispersion, mismatch, lens aberrations, and the aperture diffraction. It is, therefore, essential to investigate the image properties of this system to assess the optimum image quality attainable by the parametric image upconverter.

Experimentally the plane wave pump condition is achieved by placing the proustite crystal in the near field of a fundamental mode laser beam of large beam size. The beam size of the pump beam must be considerably larger than the interaction aperture determined by the infrared field of view. The 10.6 μm object wave radiating from the object slit is converted into a plane wave by lens No. 8. The distance between the object slit and lens No. 8 is equal to the focal length of lens No. 8. The 10.6 μm radiation emanating from lens No. 8 is a truncated plane wave provided the object slit diffracts the incoming 10.6 μm beam. The beam width of the collimated 10.6 μm radiation impinging on the proustite crystal was about 4 mm in the direction perpendicular to the object slit. The 1.06 μm pump beam was approximately 8 mm in diameter.

The sum-frequency radiation emanating from the proustite crystal is also collimated. This was checked by transversely scanning the 0.967 μm radiation at different distances from the crystal. A typical intensity profile of 0.967 μm radiation is shown in Figure 16. Neglecting slow decaying skirt, the beam width of 0.967 μm radiation was approximately 2.8 mm. This value agrees reasonably well with the expected beam

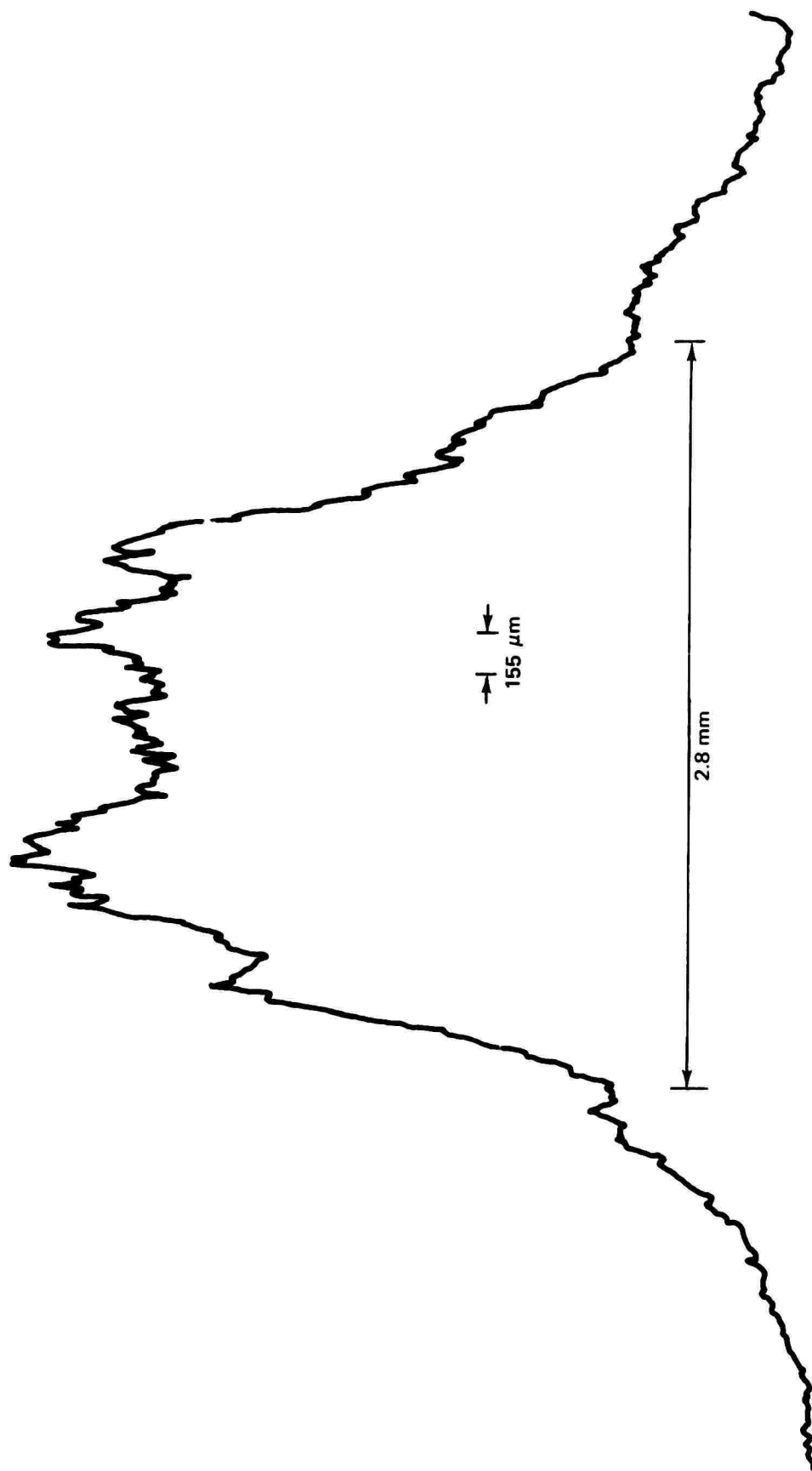


FIGURE 16. INTENSITY PROFILE OF SUM-FREQUENCY BEAM AT THE INPUT SURFACE OF IMAGE LENS NO. 11.

size of 2.66 mm calculated by the formula

$$\frac{1}{A_i} + \frac{1}{A_p} = \frac{1}{A_s}$$

where A_i , A_p , and A_s are respectively beam size of infrared object, pump, and sum-frequency beams.

The line spread function, which is a real image of object slit, is obtained by refocusing the 0.967 μm beam by lens No. 11. Figure 17 and Figure 18 are the line spread functions measured by scanning slit detection technique. A 76.2 mm focal length lens was used as lens No. 11 for the line spread function shown in Figure 17. The focal length of lens No. 11 is 152.4 mm for the line spread function shown in Figure 18. The slow decaying of the right skirt of the measured spread function is due to the long time constant of the signal amplifier employed. The line width of the measured line spread functions is compared with the diffraction limited line width. The diffraction limited line width of uniformly illuminated aperture is:

$$b = 2 \frac{\lambda f}{A} \quad (164)$$

where

b = diffraction limited line width

f = focal length of the lens

A = linear dimension of aperture

For the case considered here, A is equal to the sum-frequency beam width A_s .

Table I shows the measured and calculated line width for the two lenses used.

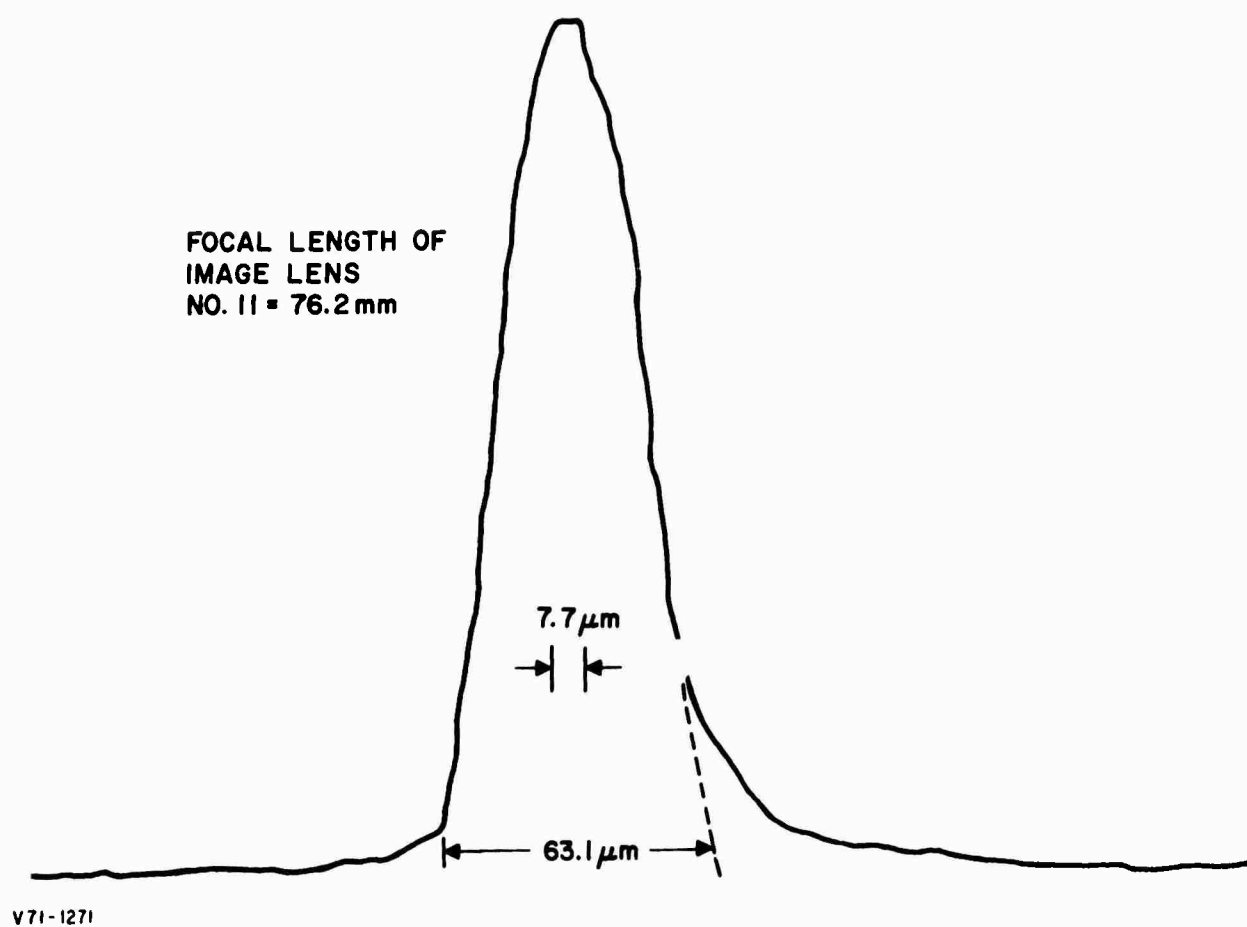


FIGURE 17. LINE SPREAD FUNCTION OF A FOURIER CONFIGURATION
UPCONVERTER SYSTEM

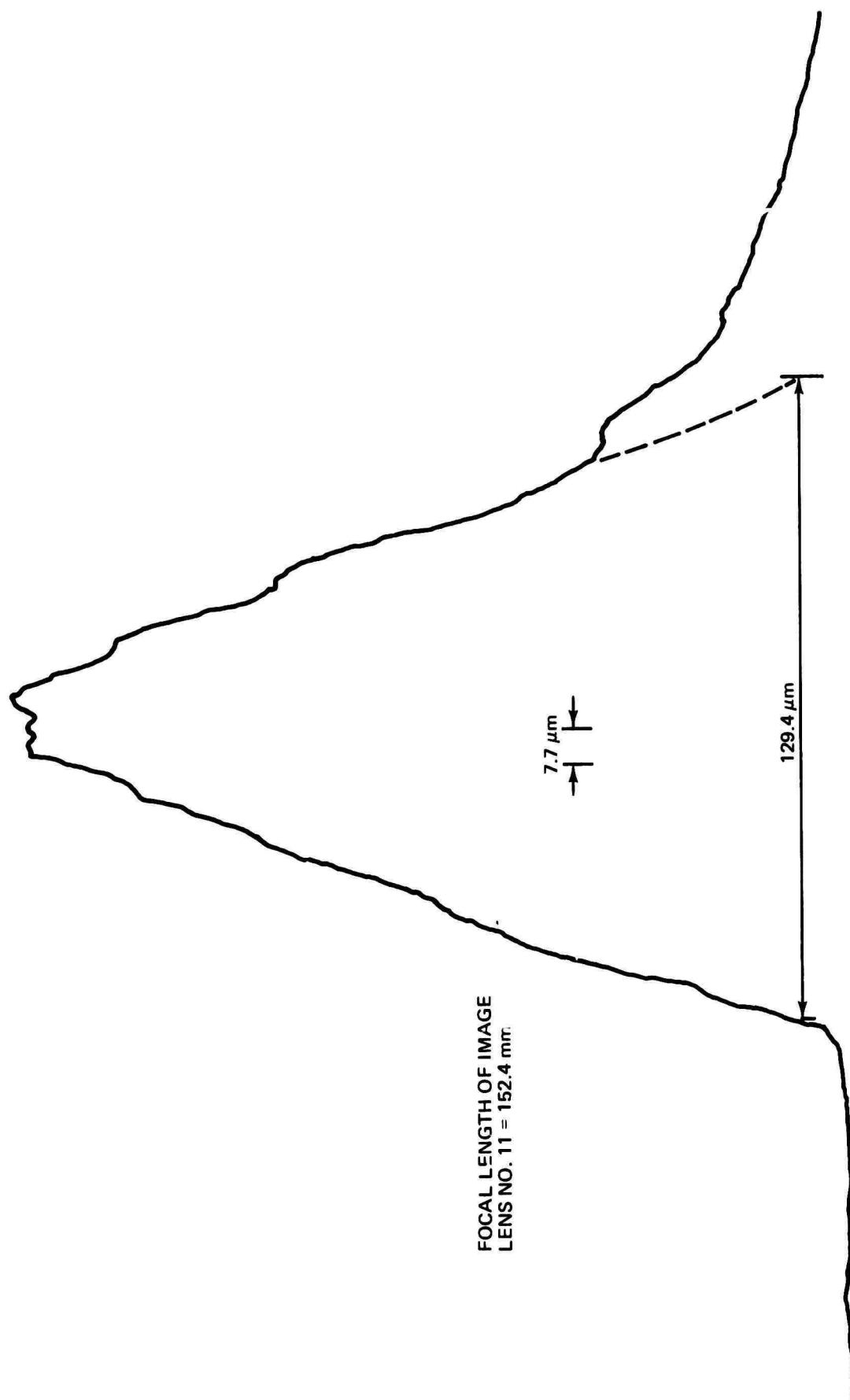


FIGURE 18. LINE SPREAD FUNCTION OF A FOURIER CONFIGURATION UPCONVERTER

**Table I Theoretical and Measured Line Width of
Line Spread Function**

f mm	Calculated by (164) μm	Measured μm	Percentage Error
76.2	52.62	63.1	20
152.4	105.24	129.4	22

In measuring the line width of spread functions shown in Figure 17 and Figure 18, the slow decay was neglected.

The discrepancy between measured and calculated line width is small enough to conclude that the system tested is practically diffraction limited. The small discrepancy is believed to be caused by the following reasons:

- 1) Diffraction limited line width of nonuniformly illuminated aperture is wider than that of uniformly illuminated aperture.
- 2) Finite width of the sampling slit tends to make measured line width appear wider than the actual width.

III-2. Results on Upconverter with Gaussian Beam Pump and Cylindrical Object Wave

Experimental arrangement and the position of pertinent components are shown in Figure 19. The $1.06\ \mu\text{m}$ pump beam was expanded to 8 mm and was collimated by lenses No. 1 and No. 2. The $10.6\ \mu\text{m}$ infrared beam was also expanded and collimated by lenses No. 5 and No. 6. An $125\ \mu\text{m}$ wide object slit was placed at the focus of lens No. 7. The lens No. 8, with 92 mm focal length, was positioned 130 mm from the object slit. The distance between lens No. 8 and the proustite crystal was 360 mm.

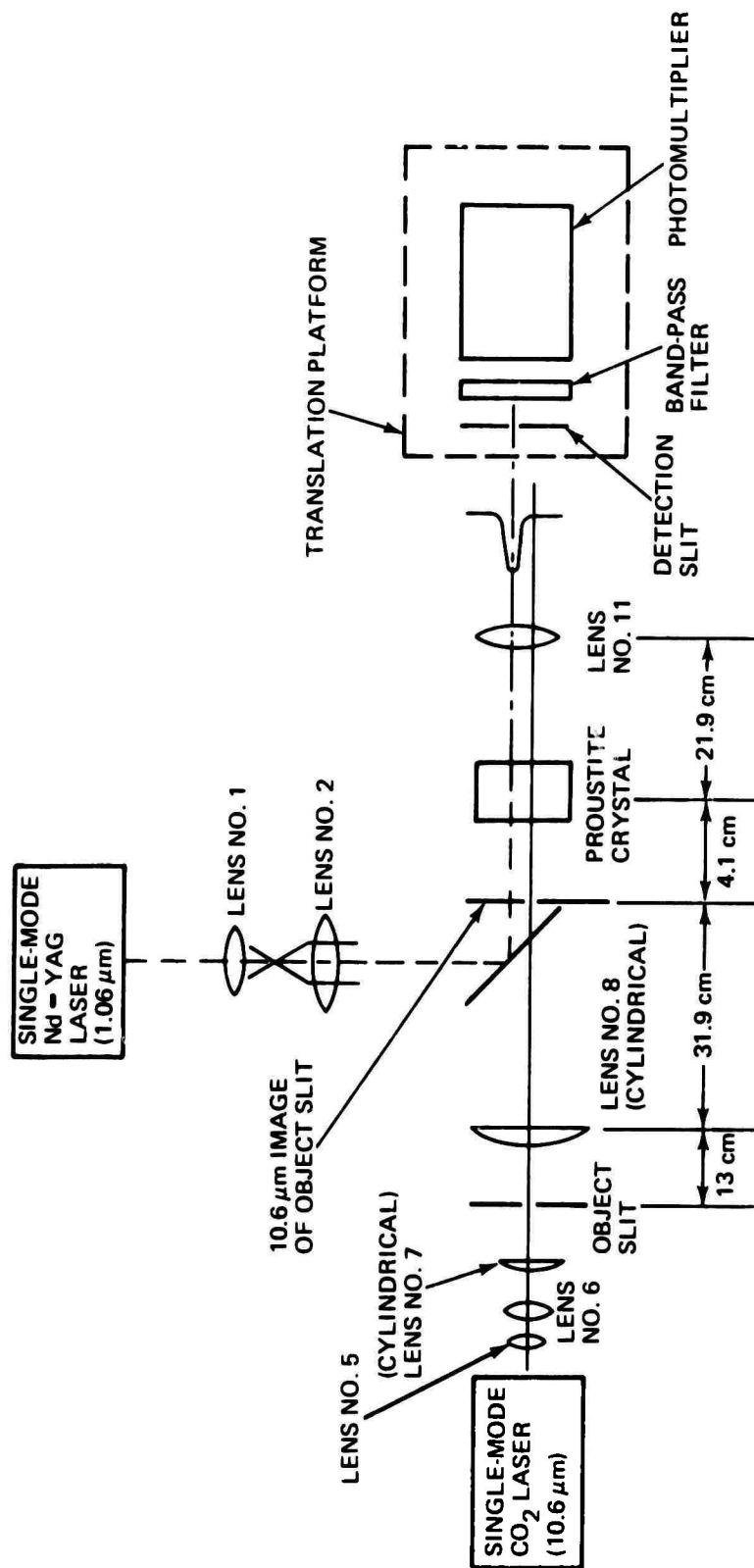


FIGURE 19. EXPERIMENTAL ARRANGEMENT TO REALIZE AN UPCONVERTER WITH GAUSSIAN BEAM PUMP AND CYLINDRICAL OBJECT WAVE

Lens No. 11 was located 219 mm from the crystal.

The infrared object wave is cylindrical, since lenses No. 7 and No. 8 are cylindrical. The 10.6 μm image of the object slit was found to be at 319 mm from lens No. 8. The distance between this infrared line image and the proustite crystal was therefore 41 mm. The infrared image of the object slit can be considered to be the apparent infrared object of the image upconverter. Limitation imposed by physical size of components such as carriages, holders, and mounts necessitates usage of an apparent object rather than positioning a real object at desired position. The infrared object aperture at the crystal may be calculated by the following relation:

$$A_p = s \theta_{i \max}.$$

Using measured value $s = 41$ mm and computed value $\theta_{i \max} = 0.18$ rad., it was found that the object aperture A_p is about 74 mm. As discussed in Chapter 3, Gaussian distribution of pump field cannot be neglected, since Gaussian pump aperture and object aperture are comparable.

On-axis line spread functions at different distances from lens No. 11 were measured and are shown in Figure 20. The numerical figures on top of the spread function indicate the distance between lens No. 11 and the sampling slit. The spread functions are seen to remain reasonably unchanged for a large axial range. The spread functions taken at 17, 16.73, 16.4 and 16.14 cm appear similar except for the difference in the peak intensity. Variation of peak intensity of those spread functions is believed to be caused by long term system instability. The line width of those spread functions is approximately 400 μm .

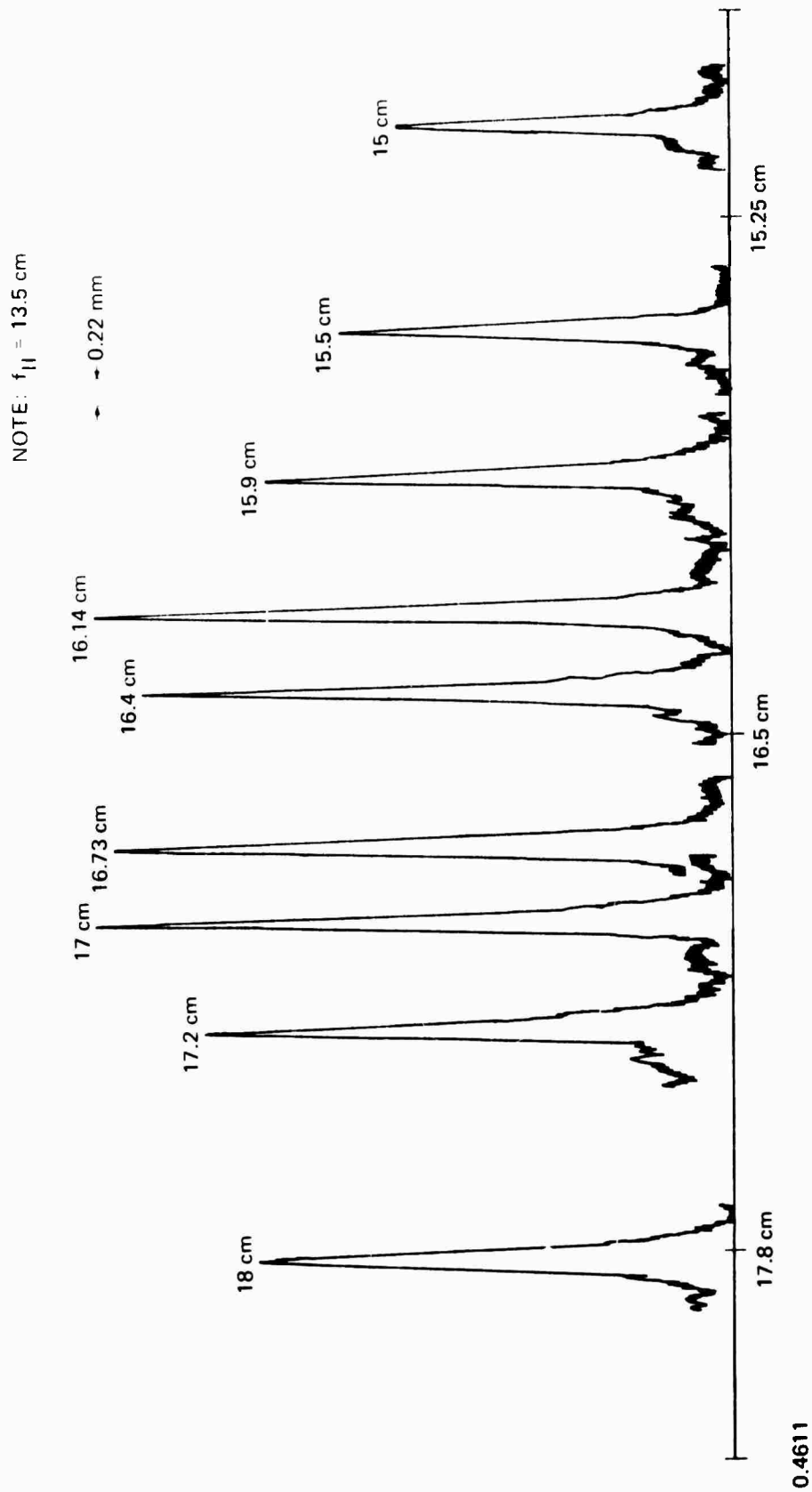


FIGURE 20. LINE SPREAD FUNCTIONS MEASURED AT DIFFERENT DISTANCE FROM LENS NO. 11 (GAUSSIAN BEAM PUMP AND CYLINDRICAL OBJECT WAVE CONFIGURATION)

To compare the experimental results with the theory, the axial position and the line width of the sum-frequency image are calculated by Eq. (6) of Chapter 2 and the lens formula. Axial position s' of the up-converted virtual image is related to the axial position s of infrared object, for $p = \infty$, by

$$s' \Big|_{p=\infty} = s \frac{n_i}{\beta n_s} \quad (165)$$

It was shown in Chapter 3 that the above relation also applies to the Gaussian beam pumped upconverter. Using parameter values $\beta = 0.0866$, $n_s = 2.80$ and $n_i = 2.677$, we found $s' \Big|_{\infty} = 11.0s$ and $s' = -431$ mm for $s = -41$ mm. The axial position of the real sum-frequency image formed by lens No. 11 was calculated by the lens formula. The distance between the virtual $0.967 \mu\text{m}$ image and lens No. 11 is 650 mm, which is the sum of s' and the distance between lens No. 11 and the crystal. The computed distance from lens No. 11 to the real sum-frequency image is then 170 mm. The measured mean distance was 166 mm. Agreement between the experimental result and theoretically computed value is reasonably well.

The width of sum-frequency line image was computed by the relation:

$$W_s = W_i M_8 M_{11} M_u$$

where W_s and W_i are respectively the width of sum-frequency image and object slit width. M_8 and M_{11} are respectively the magnification factor of lenses No. 8 and No. 11. M_u is transverse magnification factor of up-conversion process. Using known parameter values $W_i = 125 \mu\text{m}$, $M_8 = 31.9/13$, $M_{11} = 17/65$, and $M_u = 1$, we found that W_s is $87 \mu\text{m}$, which is

more than four times less than the measured value of 400 μm . It must be noted that the above computation was made without taking into account of thickness aberrations. The amount of thickness aberration in the plane wave pumped upconverter will be considered next.

It was shown that thickness aberration is independent of object location if the pump wave is plane wave and the object is at finite distance (Chapter 2). Longitudinal aberration $|\Delta s'|$ for this case is given by Eq. (30), Chapter 2. For a 1 cm long proustite crystal used in the experiment, $|\Delta s'|$ was found to be 376 mm. Longitudinal spread $|\Delta s''|$ of the real sum-frequency image formed by lens No. 11 is related to $|\Delta s'|$ by the relation

$$|\Delta s''| = |\Delta s'| M_{11}^2$$

It was found that $|\Delta s''|$ is equal to 2.57 mm. The minimum resolvable line width may be calculated by the relation

$$(W_s)_{\min} = \frac{1}{2} |\Delta s'| (\theta_s)_{\max} M_{11}$$

Using $|\Delta s'| = 3.76 \text{ cm}$, $(\theta_s)_{\max} = (\theta_i)_{\max} \lambda_s / \lambda_i = 0.016 \text{ rad.}$, and $M_{11} = 17/65$, we obtain that $(W_i)_{\min}$ is approximately 85 μm . Neglecting the effect of thickness coma, the line width of plane wave pumped upconverter should be 172 μm , which equals the sum of aberration free image width and the minimum resolvable width $(W_i)_{\min}$. The results of the above computation and measured results are tabulated in Table II.

Table II Comparison of Measured Results and Theoretically Computed Results

Computed				
	Aberration Free	Plane Wave Pumped Sys.	Measured	Measured Value/ Plane wave Pumped Value
Line width, μm	87	172	400	2.33
Longitudinal spread of 0.967 μm image, mm	0	2.57	8.6	2.21

Additional width broadening and longitudinal spread over the plane wave pumped case is due to Gaussian distribution of pump field as discussed in Chapter 3.

The above computation of aberrations of the plane wave pumped system was made with the results obtained in the geometric optics theory. The minimum resolvable spot size of sum-frequency virtual image can also be calculated by Eq. (107), Chapter 3. Using parameter value $D = 1 \text{ cm}$, $K_i = 2 \pi n_i / \lambda_i = 1.58 \times 10^4 \text{ cm}^{-1}$, we obtain the resolvable spot size $2 \rho_{\text{res}}$ equals to 223 μm . The geometric optics theory gives the resolvable spot size of virtual sum-frequency image as $1/2 |\Delta s'| \theta_{s \text{ max}}$, and it is found to be 293 μm . Agreement between these values is reasonable.

IV. MEASUREMENTS OF RESOLUTION AND INFRARED OBJECT FIELD OF VIEW

The number of linear resolution elements was measured with the Fourier configuration upconverter. The Fourier configuration was chosen because it is nearly diffraction limited. Measurement described

below allows us to obtain information on resolution and field of view. The experimental arrangement is shown schematically in Figure 21. Lenses No. 1 and No. 2 were again used as a pump beam expander. Lenses No. 5 and No. 6 formed a beam expander for 10.6 μm beam. Lenses No. 7 and No. 8 and a narrow slit were used to generate a collimated 10.6 μm ribbon beam. Mirrors No. 1 and No. 2 were adjusted so that the 1.06 μm beam travels along the direction which makes desired angle with the z-axis. The infrared 10.6 μm beam was guided by mirror No. 3 to propagate in the direction of the z-axis. Mirror No. 2 was arranged so that infrared 10.6 μm beam misses it. Mirror No. 3 was mounted on a sliding carriage so that it can be moved along the direction parallel to the y-axis. The vertical angle α shown in Figure 21 was adjusted for the maximum object angular aperture as discussed in Chapter 2.

Pump beam width A_p was made considerably larger than object beam width A_i so that the effect of Gaussian distribution is minimized.

Angle θ_i that the wave front normal of infrared object wave makes with the z-axis is related to the transverse position of mirror No. 3 by the relation

$$\theta_i = \tan^{-1}(y_i/\ell)$$

where ℓ is the distance from the proustite crystal to mirror No. 3.

The wave normal of sum-frequency beam emanating from the crystal makes an angle θ_s with the z-axis.

$$\theta_s = \frac{n_s}{n_i} \beta \theta_i \quad (166)$$

The sum-frequency image formed by lens No. 11 will be displaced a distance y_s from the z-axis

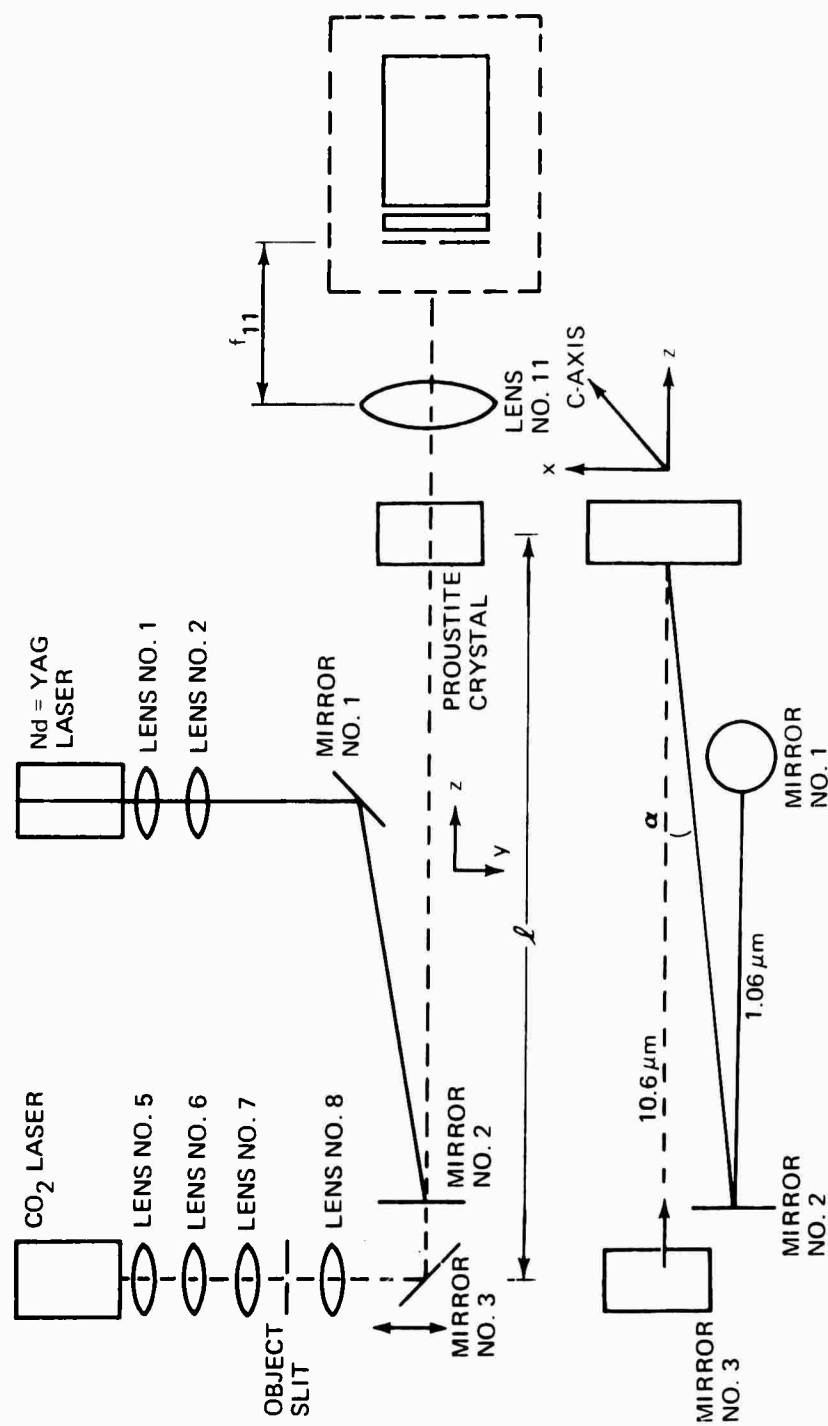


FIGURE 21. EXPERIMENTAL SETUP FOR MEASUREMENTS OF RESOLUTION AND FIELD OF VIEW

$$y_s \approx \theta_s f_{11} \quad (5-4)$$

where f_{11} is the focal length of lens No. 11

The measured on-axis and off-axis line spread functions are shown in Figure 22. The numerical value on top of each spread function indicates transverse position y_i of mirror No. 3. Measured and theoretically calculated transverse location y_s of sum-frequency image are tabulated in Table III.

Table III Measured and Computed Transverse Location of
0.967 μm image ($\ell = 160$ cm and $f_{11} = 76.2$ mm)

y_i cm	Computed y_s μm	Measured y_s μm	θ_i Computed	
			Degree	Radian
20.32	893	862	+7.3	0.129
15.24	660	616	+5.47	0.0953
4.45	193	192	+1.59	0.0278
0	0	0	0	0
-3.05	-137	-134	-1.09	0.0191
-13.97	-606	-585	-5.02	0.0874

The width of line spread functions shown in Figure 22 appears wider than actual width because of the fast scan speed and the long time constant of the amplifier. Fast scan speed was required in order to make overall measurement time interval short to avoid the effect of system instability and electrical interference. Separate measurements of an off-axis line spread function shown in Figure 23 indicates that the line width is approximately 70 μm , which is slightly larger than on-axis line width shown in Figure 17.

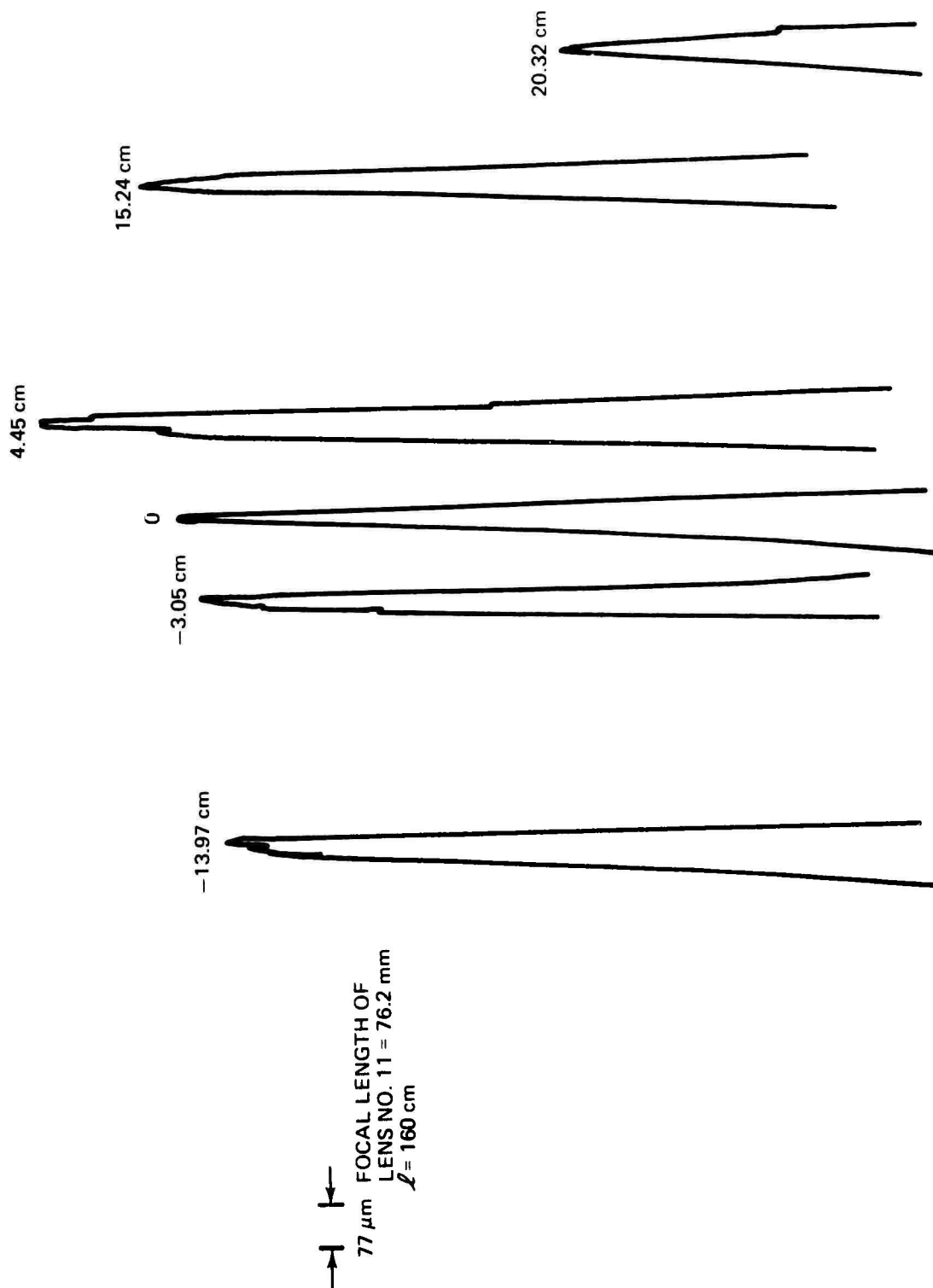


FIGURE 22. ON-AXIS AND OFF-AXIS SPREAD FUNCTION OF
FOURIER CONFIGURATION UPCONVERTER

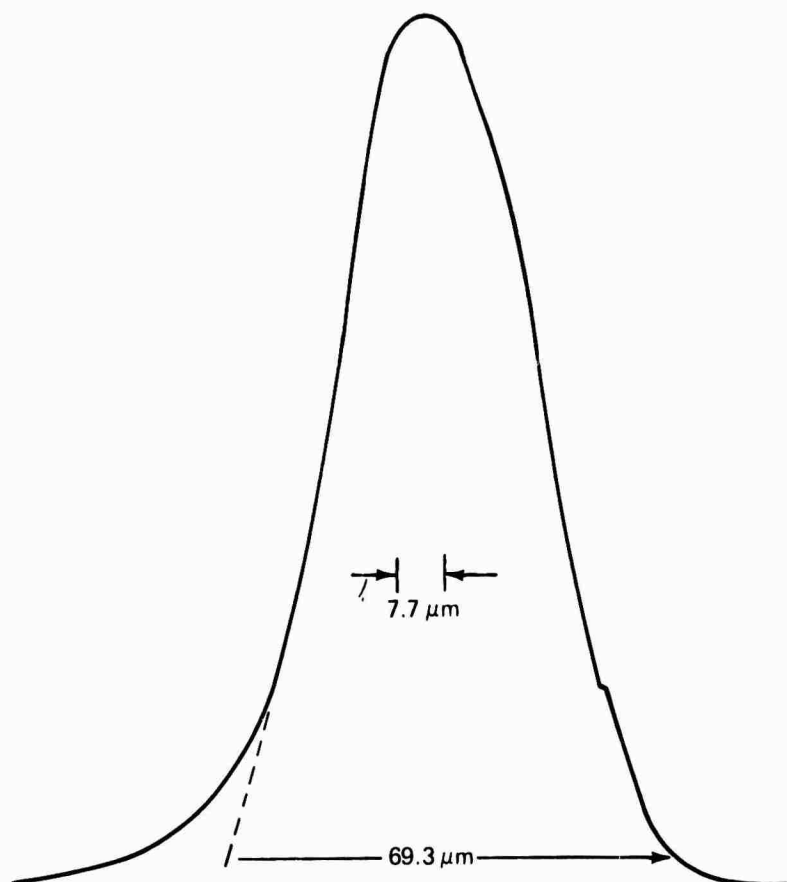


FIGURE 23. MEASURED OFF-AXIS LINE SPREAD FUNCTION

The number of linear resolution elements in the 10.6 μm angular aperture now can be calculated with measured line width and the amount of transverse dimension of sum-frequency image field shown in Figure 22. Using the Rayleigh criterion, we found that the number of linear resolution elements is 41 lines over the object angular aperture of 12.3 degrees. The number of linear resolution elements in the angular aperture of diffraction limited upconverter can be theoretically estimated

$$N = \frac{\theta_{i \max} \eta_s \beta A_s}{1.22 \lambda_s n_i}$$

where N is the number of linear resolution elements. The above relation is obtained by combining (164), (166), and (167). Assuming $A_s = 2.8 \text{ mm}$ and using known parameter values, we found that N is 39 lines, which is a good agreement with the measured result.

V. SUM-FREQUENCY IMAGES OF RESOLUTION TEST CHART WITH FOURIER CONFIGURATION UPCONVERTER

Experimental investigation of 0.967 μm image of an 10.6 μm illuminated resolution test chart is presented in this section. The experimental arrangement shown schematically in Figure 15 was used. Lenses No. 1 and No. 2 constitute the 1.06 μm pump beam expander. Lenses No. 3 and No. 4 are cylindrical and were used as a one dimensional beam compressor. The pump beam emanating from lens No. 4 is collimated and has nearly rectangular cross-section. The long side of the beam cross-section is about 8 mm and is in the direction parallel to the plane of paper. The short side of the beam cross-section is about 3 mm. Lenses No. 5 and No. 6 constitute the 10.6 μm beam expander. Lenses No. 7 and No. 8 are cylindrical and were used as one dimensional beam compressor. The 10.6 μm

beam emanating from lens No. 8 was collimated and also was nearly rectangular shape. The long side of the 10.6 μm beam cross-section was in the direction parallel to the plane of paper and was about 8 mm. The short side dimension was about 2 mm. The reason for shaping both the 1.06 μm pump and the 10.6 μm beam into rectangular shape is to utilize available 1.06 μm pump power and 10.6 μm illumination power efficiently. The resolution test bar chart shown in Figure 24 was placed between lens No. 8 and lens No. 9. The test chart was oriented such that horizontal bars are in the direction perpendicular to the paper.

The resolution chart used is the standard Air Force 1951 target. The change in pattern size is in a geometric progression based on the six root of 2. The number of line per millimeter doubles with every sixth target element. An element of target contains two patterns of three lines each at right angles to each other. The width of line to width of space ratio is a nominal 1:1. The line length to line width ratio is 5:1. Table IV lists the number of line-pair per millimeter of each element.

Table IV Number of Line-Pair per Millimeter of Each Element of 1951 Air Force Resolution Target

Group Number	Element Number					
	1	2	3	4	5	6
0	1	1.123	1.26	1.415	1.589	1.782
1	2	2.246	2.52	2.83	3.178	3.563
2	4	4.492	5.04	5.66	6.356	7.125
3	8	8.984	10.08	11.32	12.712	14.25
4	16	17.968	20.16	22.64	25.424	28.5
5	32	35.936	40.32	45.28	50.85	57

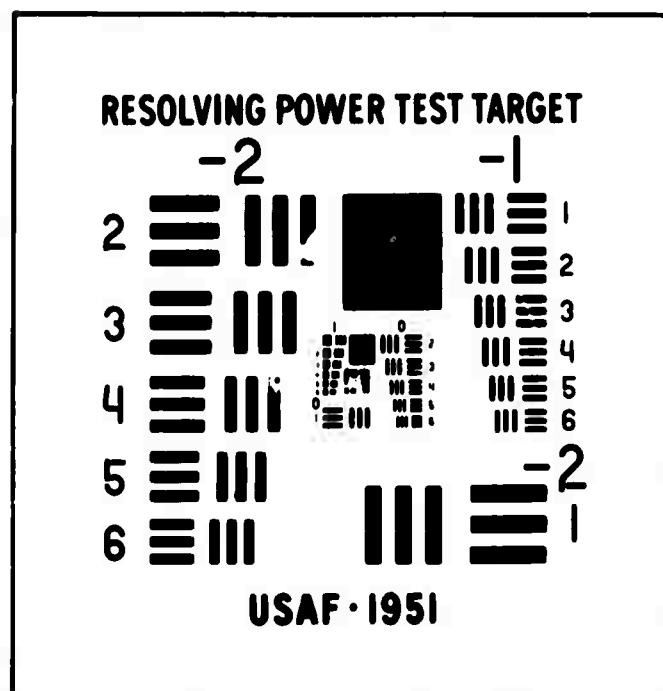


FIGURE 24. RESOLUTION TEST CHART

Table IV (Continued)

Group Number	Element Number					
	1	2	3	4	5	6
6	64	71.872	80.64	90.56	101.7	114
7	128	143.744	161.2	181.2	203.4	228

Lens No. 9, with 152.4 mm focal length, was used as an object magnifier. The magnified 10.6 μm image of the target patterns was formed in the front focal plane of lens No. 10. The proustite crystal was positioned so that the back focal plane of lens No. 10 is located at the center of the crystal. Lens No. 11 was positioned so that the distances from Lens No. 11 to the proustite crystal and to the sampling slit were exactly equal to its focal length. The object field entering the nonlinear crystal is Fourier transform (angular spectrum) of the real object field formed across the front focal plane of lens No. 10. Upconverted image field emanating from the crystal is inverse Fourier transformed by lens No. 11 and the upconverted real image is formed across the back focal plane of lens No. 11. The lens arrangement described above allows upconversion to take place in Fourier space and introduces minimum of aberrations. Focal length of lenses No. 10 and No. 11 is 120 mm and 120.7 mm, respectively.

The resolution test chart and lens No. 9 were positioned so that the 10.6 μm image of the bar pattern under study is approximately 25 mm. This arrangement makes full usage of 10.6 μm object angular aperture, since the maximum wave front tilt of angular spectrum of object field at the crystal is approximately six degrees which is comparable with measured half angular aperture of 6.15 degrees.

V-1. Intensity Profile of 0.967 μ m Images

Measured intensity profile of upconverted images are shown in Figures 25, 26, 27, and 28. In this measurement an arrangement was made so that only those test bars oriented perpendicular to the plane of the paper were illuminated by the 10.6 μ m beam. Figure 25 and Figure 26 are the image of resolution target elements 1/1 through 1/6. Figure 26 was obtained with more 10.6 μ m illumination on the element 1/6. These figures clearly show that the upconverter is capable of resolving the target element 1/6. Figure 27 is the image intensity profile of the elements 1/4, 1/5, 1/6, and 0/6. Figure 28 is the image of the elements 0/4, 0/5, and 0/6. Salient parameters of 10.6 μ m object and 0.967 μ m image of these figures are tabulated in Table V.

Table V Parameters for Figures No. 25, 26, 27, and 28

Fig. No.	Total Width of Targets Illuminated in mm	Magnification of Lens No. 9	Total Width of 10.6 μ m Image Across the Front Focal Plane of Lens No. 10 in mm	Measured Total Width of 0.967 μ m Image in mm	Theoretically Computed Width of 0.967 μ m Image in mm
25	8	3.18	25.4	2.3	2.32
26	6.8	2.76	18.75	1.71	1.72
27	7.5	2.7	20.3	2.13	1.86
28	6	3.2	19.2	1.73	1.76

Numerical values listed in last column of Table V were computed by the relation:

$$W_s = W_i \frac{n_s}{n_i} \frac{f_{11}}{f_{10}} M_9$$

where M_9 is the magnification factor of lens No. 9 and f_{10} and f_{11} are the focal length of lens No. 10 and lens No. 11, respectively. Agreement between theoretically computed total image width and measured results is reasonable. Observation of these figures shows, however, that the image width of the individual bar at the outer edge tends to be narrower than the expected width. The intensity reduction at the edge is due to tapered 10.6 μm illumination and phase-mismatch.

The number of linear resolution elements contained in the 0.967 μm image is 70 if one takes the element 1/6 as the smallest resolvable element. The angular resolution corresponding to above linear resolution is 3.0 milliradians (Fig. 26).

The intensity profile of defocussed 0.967 μm image is shown in Figure 29. Relative positions of the proustite crystal, lens No. 10, lens No. 11, and the sampling slit were arranged such that they are at the lens conjugate planes. Lens No. 9 was removed from the setup. The resolution targets 1/1 through 1/6 were illuminated with 10.6 μm laser beam and were positioned 92 cm from lens No. 10.

The effects of multi-mode pump were also investigated. Relative locations of test targets, the lenses, the crystal, and the sampling slit were the same as that used to obtain Figure 25. The 1.06 μm Nd:YAG laser output beam was purposely made multi-mode. The pump beam was collimated and shaped as described before. The intensity profile of 0.967 μm image of the target element 1/1 through 1/6 is shown in Figure 30. The resolving power of upconverted image was poorer than TEM_{00} mode pump case as was

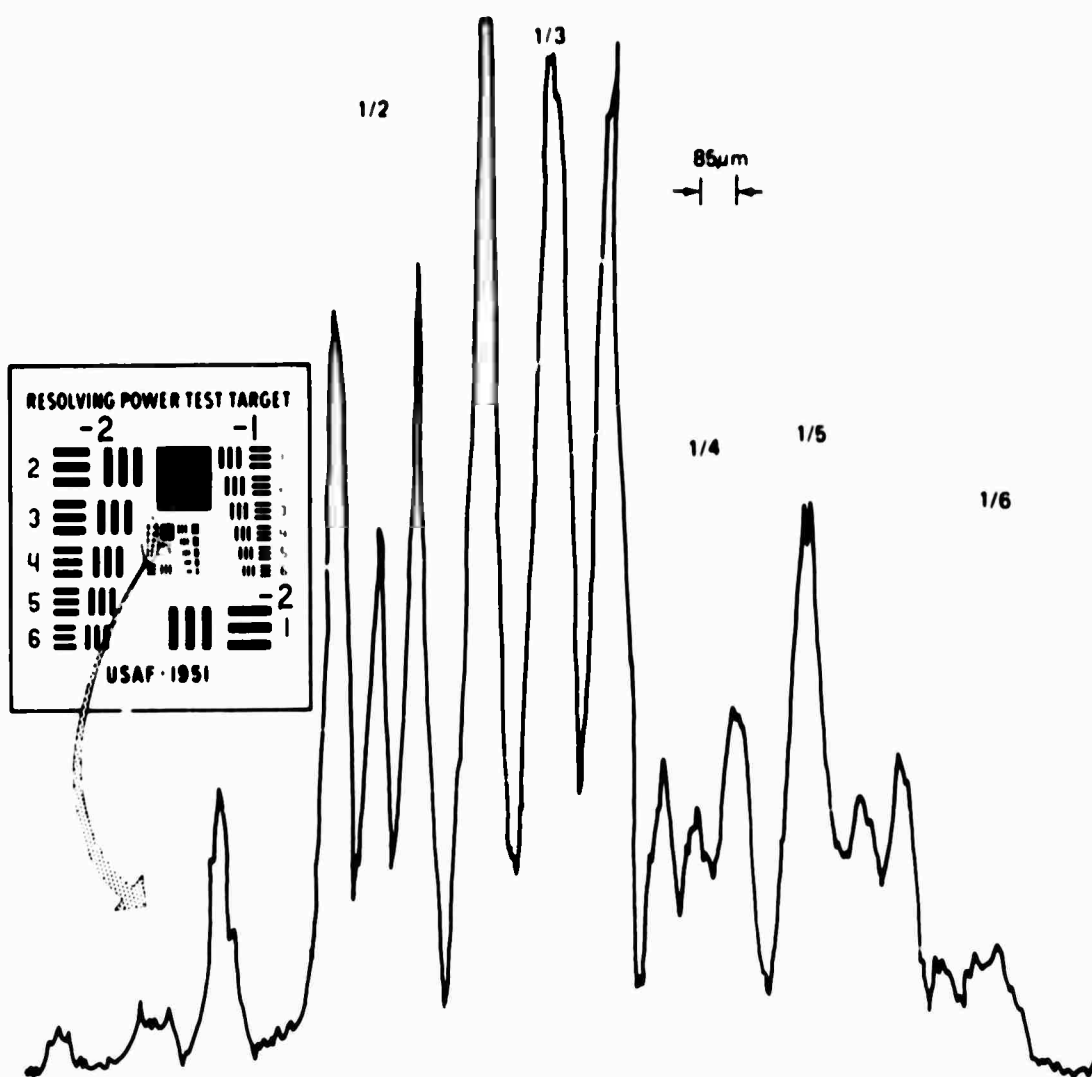


FIGURE 25. INTENSITY PROFILE OF 0.967 μm IMAGE OF 10.6 μm ILLUMINATED RESOLUTION TARGET ELEMENTS 1/1 THROUGH 1/6 .

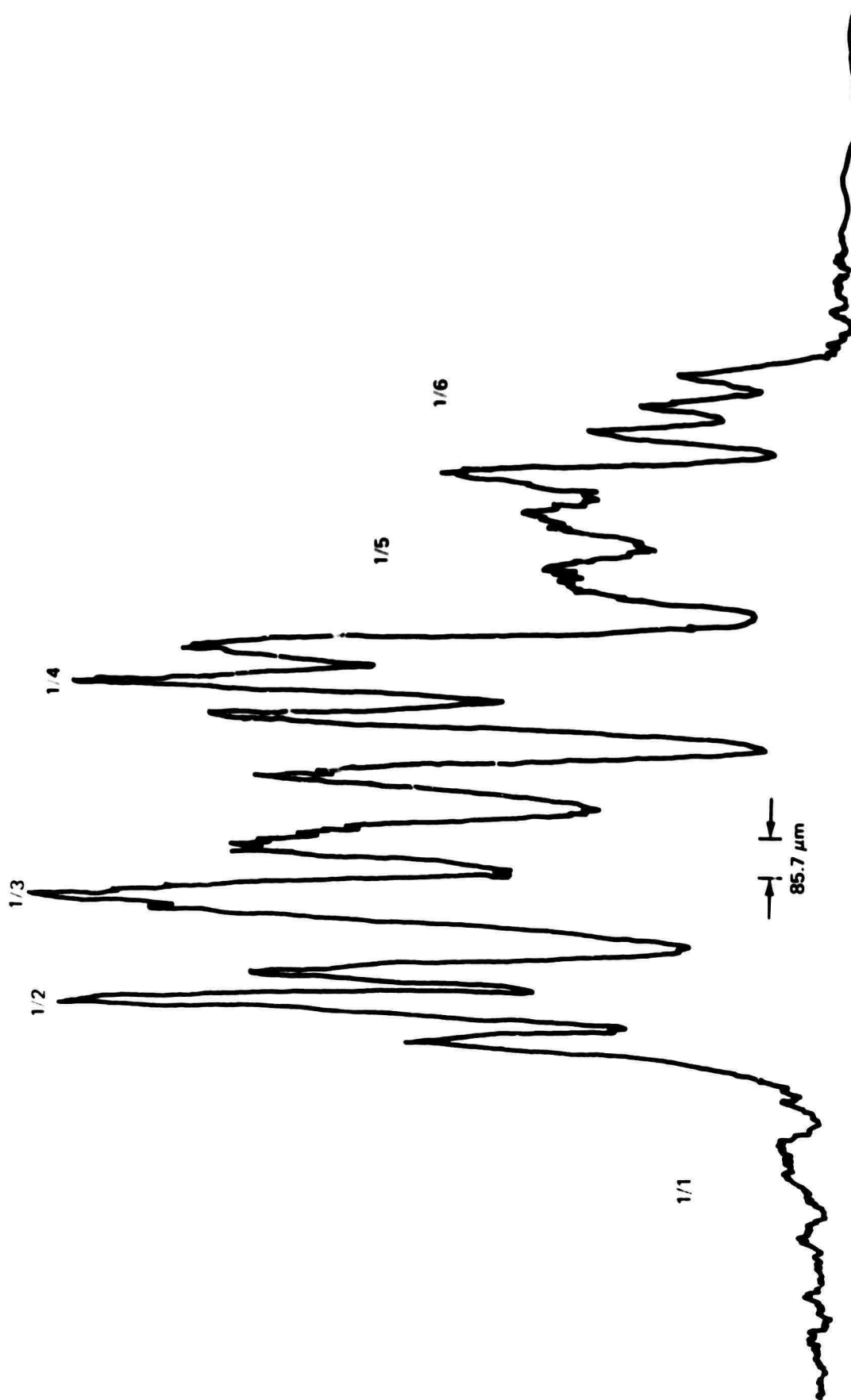


FIGURE 26. INTENSITY PROFILE OF $0.967 \mu\text{m}$ IMAGE OF $10.6 \mu\text{m}$ ILLUMINATED RESOLUTION TARGET ELEMENTS $1/1$ THROUGH $1/6$

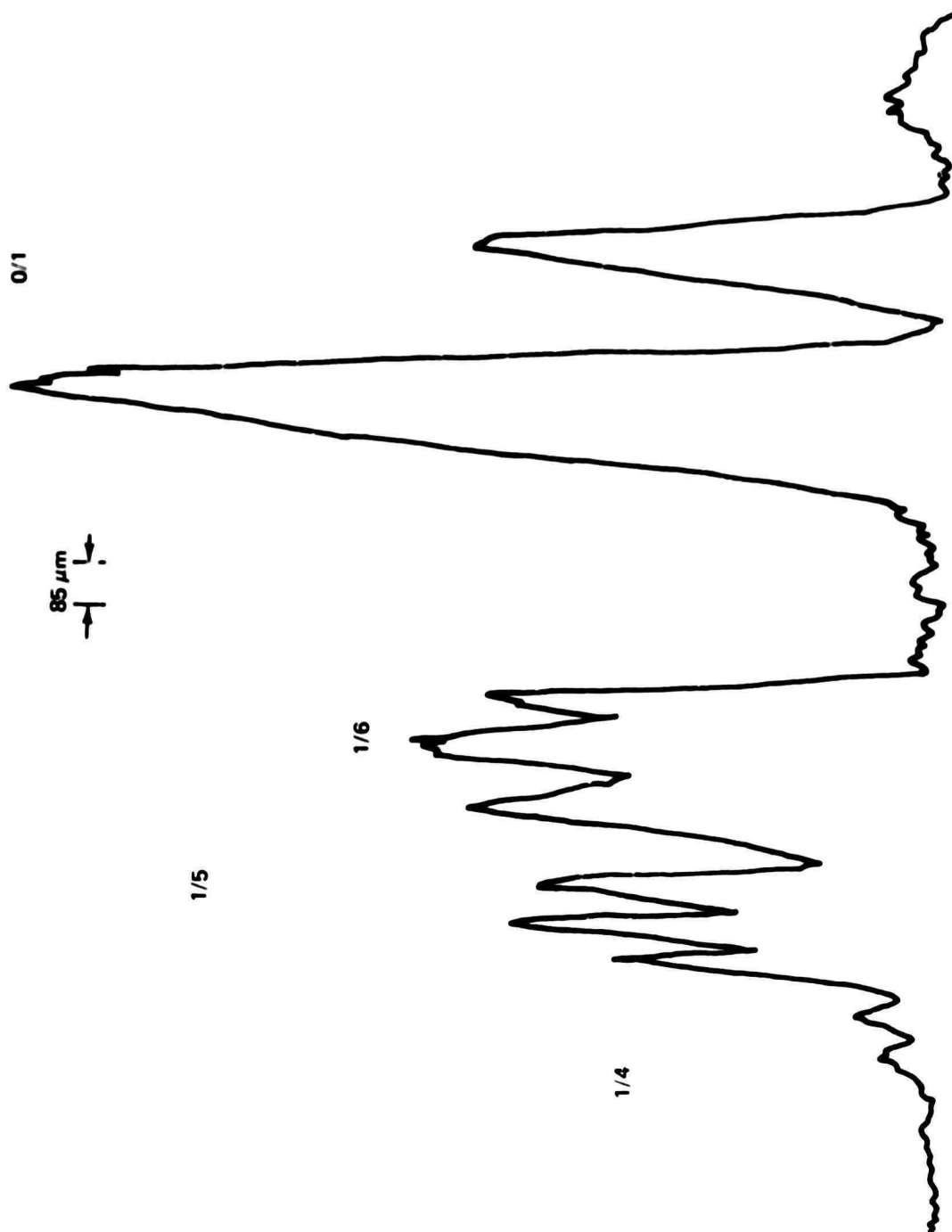


FIGURE 27. INTENSITY PROFILE OF 0.967 μm IMAGE OF 10.6 μm ILLUMINATED RESOLUTION TARGET ELEMENTS 1 4, 1/5, 1/6 AND 0/1

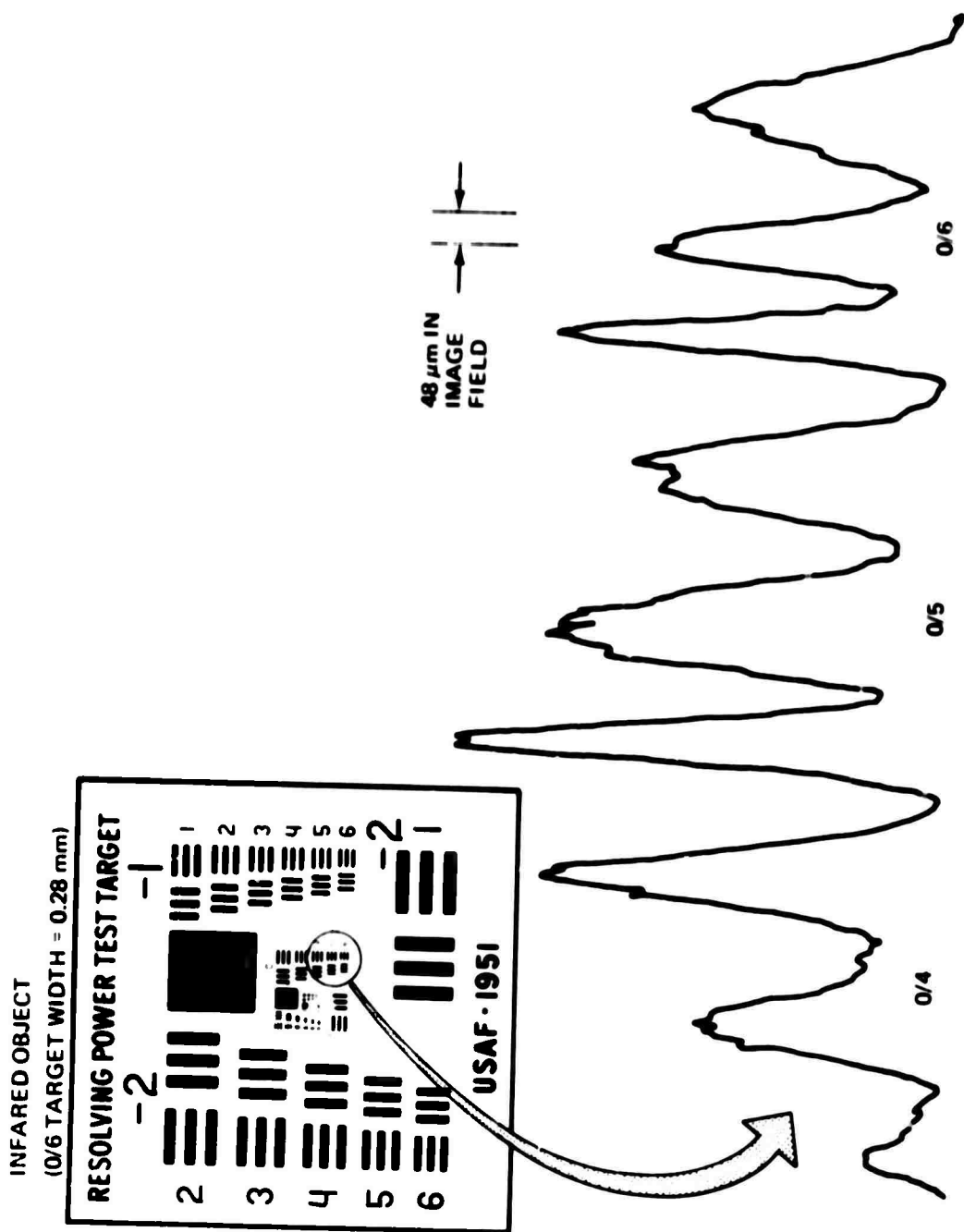
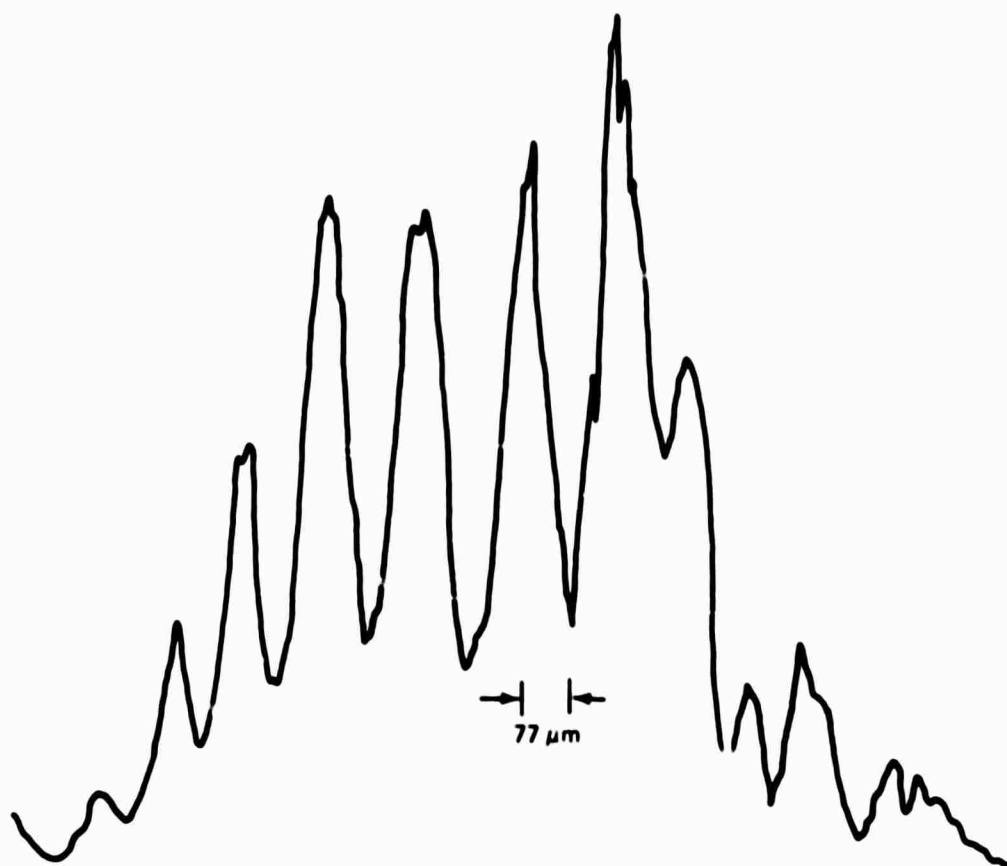


FIGURE 28. INTENSITY PROFILE OF 0.967 μm IMAGE OF 10.6 μm ILLUMINATED RESOLUTION TARGET ELEMENTS 0/4 THROUGH 0/6



**FIGURE 29. INTENSITY PROFILE OF 0.967 μm DEFOCUSSED
IMAGE OF 10.6 μm ILLUMINATED RESOLUTION
TARGET ELEMENTS 1/1 THROUGH 1/6**

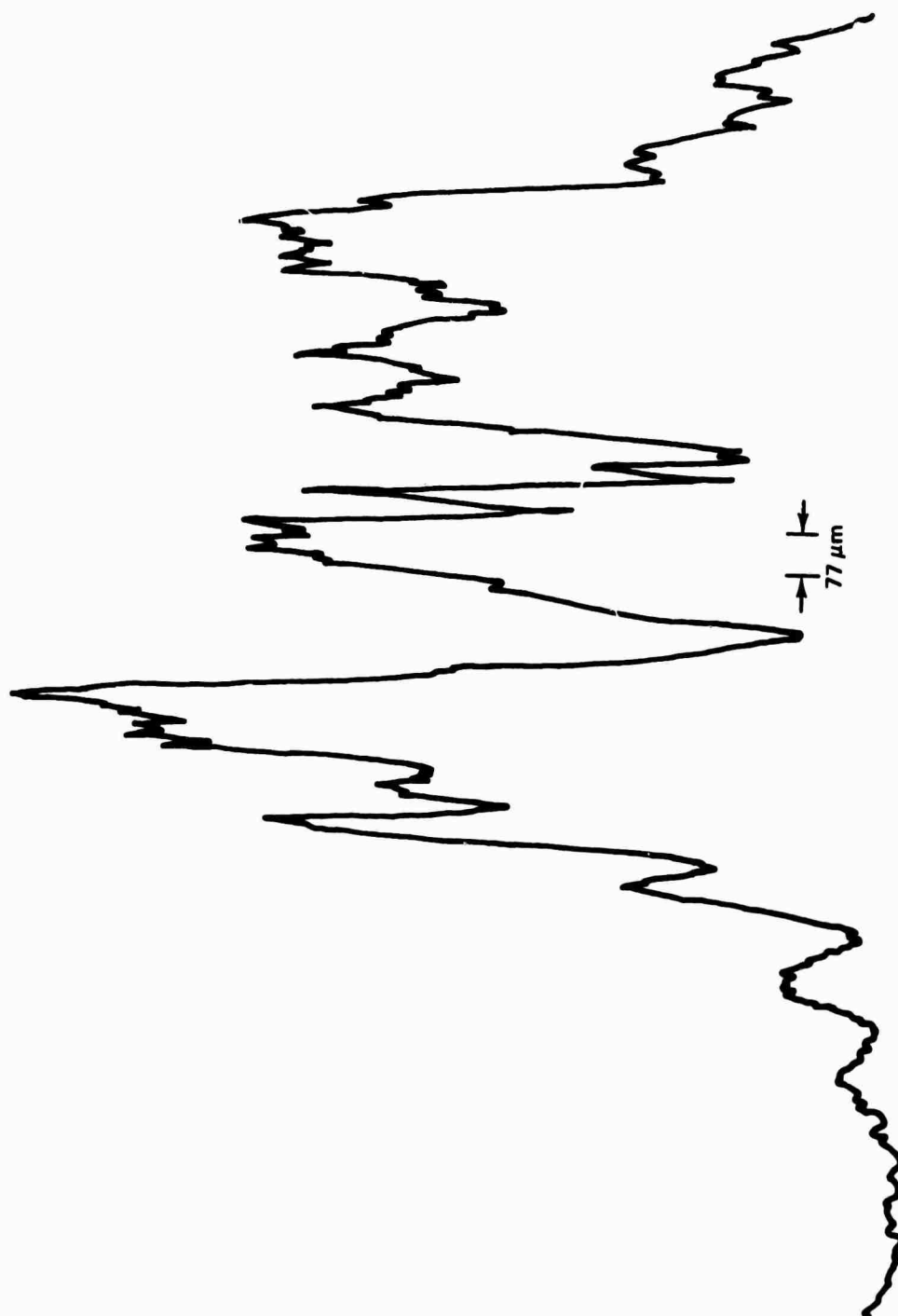


FIGURE 30. INTENSITY PROFILE OF 0.967 μm IMAGE OF 10.6 μm ILLUMINATED RESOLUTION TARGET ELEMENTS 1/1 THROUGH 1/6 (MULTI-MODE 1.06 μm PUMP)

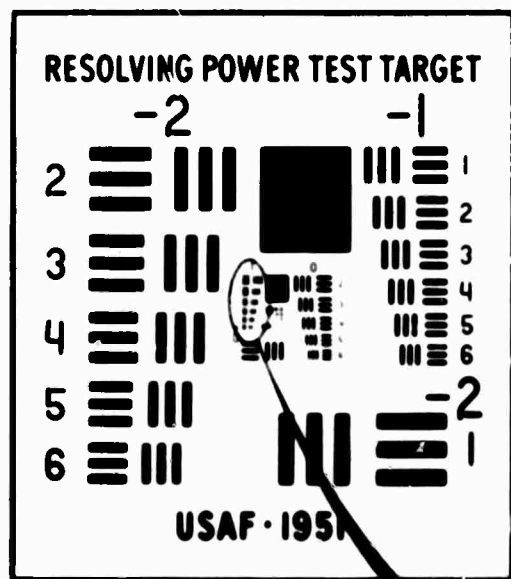
expected. Quantitative evaluation of resolution degradation due to pump beam divergence was not attempted.

V-2. Recording of 0.967 μ m Image of 10.6 μ m Illuminated Resolution Test Chart on Photographic Films

The experimental arrangement described in Section V-1 was employed except lenses No. 3, No. 4, No. 7 and No. 8 were deleted. Cross-section of both pump beam and 10.6 μ m illuminating beam is circular. A lens with 500 mm focal length was used as lens No. 11. This is required in order to obtain reasonable size 0.967 μ m image. Kodak infrared spectroscopic films Type I-M were used to record the 0.967 μ m images. A combination of 0.967 μ m bandpass and 1.06 μ m rejection filters is placed in front of the film. Figure 31 is an enlarged picture of the recorded 0.967 μ m image of resolution target elements 1/1 through 1/6. The density at the edge of the picture is low, but it clearly shows that the target element 1/6 is resolved. The actual size of the image recorded is 8.2 mm long and 3.2 mm wide. The measured magnification (image size/target size) of 1.14 agrees with the expected magnification 1.2 calculated by the relation:

$$M = M_9 \beta \frac{n_s}{n_i} \frac{f_{11}}{f_{10}} = 3.18 \times 0.091 \times \frac{500}{120} = 1.2$$

The reduction of density at the picture edge is again due to illumination taper and phase-mismatch. A portion of elements 1/1 and 1/6 were missing from the picture. It was checked later that the 10.6 μ m beam was not illuminating those portions of the pattern. The contrast of the picture is poor because of long exposure (180 sec.) required and some background light leakage.



1-2183

FIGURE 31. $0.967 \mu\text{m}$ IMAGE OF $10.6 \mu\text{m}$ ILLUMINATED RESOLUTION TEST TARGET

VI. IMAGING UPCONVERTER SENSITIVITY

As a result of analyses on upconversion carried out in Chapter 4, parametric relationships have been developed which are used in this section for evaluating the potential sensitivity of present and future upconverters. The equations used in the calculations are first given. The results are then presented and discussed.

A. Upconversion Efficiency

A key parameter in determining sensitivity is the power upconversion efficiency which for small crystal thickness is given by the classical expression

$$\eta_u = \frac{13.04 |d_{\text{eff}}|^2 \iota^2 P_p}{n_i n_s n_p \lambda_s^2 A} = K \frac{P_p \iota^2}{A} \quad (1)$$

where $|d_{\text{eff}}|$ = effective nonlinear coefficient for upconverter material

n_i, n_s, n_p = refractive indices for input signal, output signal and pump respectively

ι = thickness of upconverter material

λ_i, λ_s = wavelengths of input signal and output signal respectively

P_p = pump power

A = interaction area on upconverter material

For a Type II matched proustite crystal, a Nd:YAG pump laser, and a $10.6 \mu\text{m}$ input signal the following parameter values hold.

$\theta = 12 \text{ degrees} = 0.2 \text{ radians}$

$\lambda = 10.6 \mu\text{m}$

$|d_{\text{eff}}| = 66 \times 10^{-9} \text{ esu based on } d_{22} = 75 \times 10^{-9} \text{ esu and matching angle of } 20^\circ$

$$\begin{aligned}
 r &= 0.6 \text{ cm} \\
 n_i &= 2.677 \\
 n_s &= 2.804 \\
 n_p &= 2.817 \\
 \lambda_s &= 0.967 \text{ } \mu\text{m}
 \end{aligned}$$

For these parameters we compute

$$K = 2.95 \cdot 10^{-12} \text{ m}^2 \text{ W}^{-1}$$

B. Number of Resolution Elements

It can be shown that for diffraction limited imaging upconversion in both a Fourier space device and an image space device an imaging upconversion figure of merit may be defined for a circular image using equation 1 as

$$\eta_u n = \theta^2 P_p K_1 \quad (2)$$

where

η_u = conversion efficient of upconverter

n = number of Rayleigh resolution elements in upconverted image

θ = input signal acceptance angle

P_p = pump power

$$K_1 = \frac{4}{\pi} \frac{K^2}{(1.22 \lambda_i)^2} = 8.07 \cdot 10^{-2} \text{ } \omega^{-1}$$

λ_i = wavelength of input signal

C. Sensitivity

The noise equivalent power of the upconverter system $(NEP)_s$ may be computed as follows.

A 10.6 μm detection system is employed in which the upconverter is followed by the Varian Associates image intensifier being developed under ONR sponsorship, followed in turn by a detection device with a response peaked to the yellow green output of the P-20 phosphor at the image intensifier output. Then

$$(\text{NEP})_s = \frac{2h\nu_s}{\eta_u \eta_{ii}} + \frac{(\text{NEP})_d}{\eta_u G_{ii}}$$

where

h = Planck's constant

ν_s = frequency of output signal

η_{ii} = quantum efficiency of image intensifier

G_{ii} = power gain of image intensifier

$(\text{NEP})_d$ = noise equivalent power of visible light detection device

The first term is due to quantum noise effects and the second term is the noise contributed by the detector stage. The following set of values is employed:

$G_{ii} = 100$ (value obtained from Varian)

$\eta_{ii} = 0.10$

$2h\nu_s = 4 \times 10^{-19}$ watt

$(\text{NEP})_d = 10^{-16}$ watts for a 1 Hz bandwidth

We obtain

$$\begin{aligned} (\text{NEP})_s &= \frac{1}{\eta_u} \left[\frac{4 \times 10^{-19}}{0.1} + \frac{10^{-16}}{10^2} \right] \\ &= \frac{1}{\eta_u} \left[(4 + 1) \times 10^{-18} \right] = \frac{5 \times 10^{-18}}{\eta_u} \end{aligned} \tag{3}$$

Note that under the above conditions quantum noise limited operation has been approached and a further increase in image intensifier gain will do little to improve overall system performance (although an improvement in quantum efficiency would still be desirable).

D. Results

We obtain for the three principal equations:

$$\begin{aligned}\eta_u &= 1.03 \cdot 10^{-11} P_p/A \\ n \cdot \eta_u &= 3.23 \cdot 10^{-3} P_p \\ (NEP)_s &= \frac{5 \cdot 10^{-18}}{\eta_u} \text{ watt/Hz}^{1/2}\end{aligned}$$

Note that the first equation yields an upper bound on upconversion efficiency based on crystal power handling capability (pump power density). The second equation gives the relation between number of resolution elements and total pump power. The third equation gives the sensitivity.

Using the above values several interesting cases of imaging up-conversion have been tabulated in Table I for two materials:

1. Proustite (present)
2. Chalcopyrite (future)

The first one is a fair approximation of the present imaging up-converter not including the NEP estimate. This NEP estimate depends on the Varian Associates image intensifier that is expected GFE on the followon program. The present system NEP is about $10^{-8} \text{ W/Hz}^{1/2}$ since no image intensifier is used, although on a related single-resolution element $10.6 \mu\text{m}$ upconverter a value of $1.1 \times 10^{-9} \text{ watt sec}^{1/2}$ measured ($3.7 \times 10^{-10} \text{ watt sec}^{1/2}$ corrected) was obtained, which is the best value reported to date.

TABLE VI. CHARACTERISTICS OF IMAGING UPCONVERTERS

Number of Resolution Elements	P_p Watts	P_p/A Watts/cm ²	Nonlinear Material	η_u Conversion Efficiency	(NEP) _s ^{1/2} Watts/Hz	Comments
1400 (70x20)	0.3 cw	3	Proustite	3.1×10^{-7}	1.6×10^{-11}	Present system with 10% Inten- sifier
2.25×10^4 (150 x 150)	10 cw	14	Proustite	1.44×10^{-6}	3.5×10^{-12}	Proposed system
1000 (32x31)	10 cw	300	Proustite	3.1×10^{-5}	1.6×10^{-13}	Destructive power den- sity
2.25×10^4 (150 x 150)	100 cw	140	Proustite	1.4×10^{-5}	3.5×10^{-13}	Destructive power den- sity
2.25×10^4 (150 x 150)	10^6 pulsed	1.4×10^6 pulsed	Proustite	1.44×10^{-1}	3.5×10^{-17}	Low duty cycle op- eration
2.25×10^4 (150 x 150)	100 cw	140	CdGeP ₂	8.2×10^{-4}	6.1×10^{-15}	Shows future potential sensitivity

Experience both at AIL and elsewhere has indicated that a power density near 100 w/cm^2 the proustite crystal is damaged. Therefore the first two cases in Table IV are safe and the two shown for 300 and 140 w/cm^2 are not realistic. From the last equation above a power density of 10^6 w/m^2 gives a maximum conversion efficiency of 1.03×10^{-5} . This represents a material limit which can be approached but not safely surpassed on a cw basis. A pulsed upconverter with significantly high peak power but lower average power is capable of higher values of conversion efficiency. For example a 1 megawatt pulse on a 150×150 upconverter may be capable of achieving up to 1.4×10^{-1} conversion efficiency.

The Q-switched case in Table VI shows a very great improvement over the cw cases. However, this improvement is real only during the pulse duration. In order to obtain effectively an average improvement in system performance the system noise during the interpulse period must be suppressed by a gating technique that isolates the output detector from the system noise source. Such noise sources include dark current from the image intensifier and laser lamp leakage. A gating pulse on the power supply for the image intensifier or an electro-optic shutter would serve this purpose. Also, the output detector must provide integration of the upconverted signal during the pulse. This sample and hold approach should result in significant overall system performance although the maximum usable information bandwidth has been reduced to the periodic sampling frequency. In many applications a 100 frames/second imaging device would nevertheless be extremely useful.

An important aspect of imaging upconverter development is its future potential for growth. At several U. S. A. laboratories and in the U. S. S. R. work is proceeding to develop better upconverter materials. Significantly, in the U. S. A. Stanford University and Bell Telephone Laboratories are investigating the chalcopyrite crystal group for nonlinear

optics application. CdGeAs has shown good results for second harmonic generation and CdGeP₂ has a calculated figure of merit 57 times greater than proustite for a Nd:YAG pump and a 10.6 μm signal. The power-handling capacity of this material is comparable to GaAs and therefore very much better than proustite. Attempts to grow optical quality usable size crystals of CdGeP₂ are being made at Stanford University. They predict a usable sample within one year.

The computations of Table VI are shown for proustite and are then extrapolated to include this new material with which the long term potential of imaging upconverters becomes additionally attractive.

optics application. CdGeAs has shown good results for second harmonic generation and CdGeP₂ has a calculated figure of merit 57 times greater than proustite for a Nd:YAG pump and a 10.6 μm signal. The power-handling capacity of this material is comparable to GaAs and therefore very much better than proustite. Attempts to grow optical quality usable size crystals of CdGeP₂ are being made at Stanford University. They predict a usable sample within one year.

The computations of Table VI are shown for proustite and are then extrapolated to include this new material with which the long term potential of imaging upconverters becomes additionally attractive.

REFERENCES

- ¹ J. E. Midwinter, and J. Warner, Upconversion of Near Infrared to Visible Radiation in LiNbO_3 , J. Appl. Phys. 38, 519 (1967).
- ² R. C. Miller, and W. Norland, Conversion of Near Infrared to Visible Light by Optical Mixing, IEEE QE-3, 642 (1967).
- ³ J. Warner, Photomultiplier Detection of 10.6- μ Radiation Using Optical Upconversion in Proustite, Appl. Phys. Letters 12, 232 (1968).
- ⁴ Y. Klinger, and F. Arams, Infrared 10.6 Micron CW Upconversion in Proustite Using an Nd:YAG Laser Pump, IEEE 57, 797 (1969).
- ⁵ W. Gandrud, and G. Boyd, Photomultiplier Detection of 10.6- μ Radiation Using CW Sum-Mixing in Ag_3SbS_3 , Opt. Comm. 1, 187 (1969).
- ⁶ J. E. Midwinter, Image Conversion from 1.06- μ to the Visible in LiNbO_3 , Appl. Phys. Letters 12, 68 (1968).
- ⁷ J. E. Midwinter, Parametric Infrared Image Converters, IEEE QE-4, 716, (1968).
- ⁸ R. A. Andrews, IR Image Upconversion in KDP, IEEE Conf. on Laser Engineering and Application (1969).
- ⁹ R. Lucy, and J. Gunter, Frequency Conversion of Blackbody Objects into Visible Images by Optical Mixing, 1970 Spring Meeting, Opt. Soc. of Amm., Paper # FE 11, (1970).
- ¹⁰ J. Armstrong, N. Bloembergen, J. Ducuing, and P. Pershen Interaction Between Light Waves in a Nonlinear Dielectric, Phys. Rev. 127, 1918 (1962).
- ¹¹ G. Boyd, and D. Kleinman, Parametric Interaction of Focused Gaussian Light Beam, J. Appl. Phys. 39, 3957 (1968).

- ¹² D. Kleinman, and G. Boyd, Infrared Detection by Optical Mixing, J. Appl. Phys. 40, 546 (1969).
- ¹³ A. H. Firester, Image Upconversion, Part III, J. Appl. Phys. 41, 703 (1970).
- ¹⁴ A. H. Firester, The Thin Lens Equation for Optical Parametric Image Conversion, Opto-Electronics 1, 138 (1969).
- ¹⁵ R. Andrews, IR Image Parametric Upconverter, IEEE QE-6, 68 (1970).
- ¹⁶ S. Peng, and E. Cassedy, Scattering of Light Waves at Boundaries to Parametrically Modulated Media, Modern Optics, Polytechnic Institute of Brooklyn, 299 (1966).
- ¹⁷ M. V. Hobden, The Dispersion of the Refractive Indices of Proustite (Ag_3AsS_3), Opto-Electronics 1, 159 (1969).
- ¹⁸ J. Warner, Phase-Matching for Optical Upconversion with Maximum Angular Aperture - Theory and Practice, Opto-Electronics 1, 25 (1969).
- ¹⁹ J. E. Midwinter, Infrared Upconversion in Lithium-Niobate with Large Bandwidth and Solid Acceptance Angle, Appl. Phys. Letters 14, 29 (1969).
- ²⁰ Warner, J., Spatial Resolution Measurements in Upconversion from 10.6 μm to the Visible, Applied Physics, Letters, Vol. 13, p 360, 1968.
- ²¹ Klinger, Y., and Arams, F., Infrared 10.6-Micron CW Upconversion in Proustite using an ND:YAG Laser Pump, Proc. IEEE, Vol. 57, p 1797-1798, October 1968.
- ²² Goodman J., Introduction to Fourier Optics McGraw-Hill 1968.
- ²³ Kleinman D., Theory of Second Harmonic Generation of Light Phys. Rev., 128, p 1761 (1962).

- ²⁴Boyd G., Ashkin A., Dziedzic J. and Kleiman D. Second Harmonic Generation of Light with Double Refraction Phys. Rev. 137, p A1305 (1965).
- ²⁵Yariv A. Quantum Electronics, Wiley & Sons 1967.
- ²⁶Bloembergen, N., Pershan, P. Light Waves at the Boundary of Nonlinear Media Phys. Rev. 218 p 606 (1962).
- ²⁷Born & Wolf, Principles of Optics 2nd Ed. Press.
- ²⁸G. D. Boyd and J. P. Gordon Confocal Multimode Resonator for Millimeter through Optical Wavelength Masers Bell System Tech J. 40 p 489 (1961).
- ²⁹G. D. Boyd and A. Ashkin Theory of Parametric Oscillator Threshold with Single Mode Optical Masers and Observation of Amplification in LiNbO_3 Phys. Rev. 146 p 187 (1966).
- ³⁰Rose, A. The Relative Sensitivities of Television Pickup Tubes, Photographic Film, and the Human Eye , Proc. IRE, p. 293, (1942)
- ³¹Rose, A. Television Pickup Tubes and the Problem of Vision , Advances in Electronics, Vol. 1, 1948, Academic Press, Inc. N. Y.
- ³²Lewis, W. B. Fluctuations in Streams of Thermal Radiation , Proc. Phys. Soc., Lond. 59 p 34 (1947).
- ³³Fried, D. L., Noise in Photoemission Current , Applied Optics 4, p. 79, (1965.)
- ³⁴Eberhardt, E. H., Noise in Photomultiplier Tubes , IEEE Trans. Vol. NS-14, p. 7, 1967.
- ³⁵Weimer, P.K., Television Camera Tubes: A Research Review , Advances in Electronics and Electron Physics, Vol. 13, (1960).

- ³⁶ DeHaan, E. F., Signal-to-Noise Ratio of Image Devices, Advances in Electronics and Electron Physics, Vol. 12, (1960).
- ³⁷ Louisell, W. and Yariv, A. Quantum Fluctuations and Noise in Parametric Process I, Phys. Rev. 124, p.1646.

APPENDIX A

FOURIER REPRESENTATION OF COMPLEX FIELD DISTRIBUTION

If the complex field distribution across any plane is Fourier analyzed, the various spatial Fourier components can be identified as plane waves traveling in different directions. The field at any other point in space can be calculated by summing the contribution of these plane waves, taking due account of the amplitude change and the phase shifts they have undergone in propagating to the point in question.

Let the field across a plane at $z = z_1$, be represented by $U_{-1}(x, y, z_1)$. This field can be represented as a Fourier integral

$$U_{-1}(x, y, z_1) = \int \underline{u}_{-1}(\underline{\kappa}, z_1) e^{i\underline{\kappa} \cdot \underline{\rho}} d\underline{\kappa} \quad (A1)$$

The component field amplitude, called the angular spectrum of $U_{-1}(x, y, z_1)$, $\underline{u}_{-1}(\underline{\kappa}, z_1)$ can be expressed as inverse transform

$$\underline{u}_{-1}(\underline{\kappa}, z_1) = \frac{1}{(2\pi)^2} \int U_{-1}(\underline{\rho}, z_1) e^{-i\underline{\kappa} \cdot \underline{\rho}} d\underline{\rho} \quad (A2)$$

Now recall that the equation for a unit-amplitude plane wave propagating with direction cosine (α, β, γ) is simply $\exp \left[i \frac{2\pi}{\lambda} (\alpha x + \beta y + \gamma z) \right]$ where $\alpha^2 + \beta^2 + \gamma^2 = 1$. Thus across the plane $z = z_1$, a complex exponential function $\exp \left[i(\underline{\kappa}_x x + \underline{\kappa}_y y + \gamma z) \right]$ may be regarded as a plane wave propagating with direction cosines

$$\alpha = \frac{\lambda}{2\pi} \underline{\kappa}_x, \quad \beta = \frac{\lambda}{2\pi} \underline{\kappa}_y \quad \text{and} \quad \gamma = \sqrt{1 - \alpha^2 - \beta^2}$$

Consider now the angular spectrum of U across a plane parallel to the xy plane at a distance z_2 from the transverse plane z_1 . Let the $\underline{u}_{-2}(\underline{\kappa}, z_2)$ be the angular spectrum of $U_{-2}(\underline{\rho}, z_2)$

$$\underline{u}_2(\underline{\kappa}, z_2) = \frac{1}{(2\pi)^2} \int \underline{u}_2(\underline{\rho}, z_2) e^{-i\underline{\kappa} \cdot \underline{\rho}} d\underline{\rho} \quad (\text{A3})$$

where

$$\underline{\kappa} = \kappa \hat{x}_0 + \kappa \hat{y}_0$$

$$\underline{\rho} = x \hat{x}_0 + y \hat{y}_0$$

The effect of wave propagation on the angular spectrum can be found easily by substituting Fourier integral representation of $\underline{u}_2(\underline{\rho}, z_2)$ into the wave equation. For the case of source free isotropic space it can easily be shown that $\underline{u}_2(\underline{\kappa}, z_2)$ and $\underline{u}_1(\underline{\kappa}, z_1)$ are related by

$$\underline{u}_2(\underline{\kappa}, z_2) = \underline{u}_1(\underline{\kappa}, z_1) e^{i(K^2 - \underline{\kappa}^2)^{1/2} (z_2 - z_1)} \quad (\text{A4})$$

This result shows that when $\underline{\kappa}$ satisfies $K^2 - \underline{\kappa}^2 > 0$ the effect of propagation over a distance $(z_2 - z_1)$ is simply a change in the relative phases of the various angular spectrums. Since each plane-wave component propagates at a different angle, each travels a different distance to reach a given transverse plane and relative phase delays are thus introduced.

We note that the field $\underline{u}_2(\underline{\rho}, z_2)$ can be written in terms of initial angular spectrum by

$$\underline{u}_2(\underline{\rho}, z_2) = \int \underline{u}_1(\underline{\kappa}, z_1) e^{i(K^2 - \underline{\kappa}^2)^{1/2} (z_2 - z_1)} e^{i\underline{\kappa} \cdot \underline{\rho}} d\underline{\kappa} \quad (\text{A5})$$

APPENDIX B

WAVE EQUATION FOR ANGULAR SPECTRUM

In this section the wave equation that describes interaction of angular spectrum in a lossless non-linear material is derived. In anisotropic medium the electromagnetic fields are related by Maxwell's equation:

$$\nabla \times \underline{\underline{E}}(\rho, z, t) = -\frac{1}{c} \frac{\partial \underline{\underline{B}}(\rho, z, t)}{\partial t} \quad (\text{B1})$$

$$\nabla \times \underline{\underline{H}}(\rho, z, t) = \frac{1}{c} \frac{\partial \underline{\underline{D}}(\rho, z, t)}{\partial t} \quad (\text{B2})$$

where $\underline{\rho}$ is transverse coordinates normal to the z direction and c is velocity of light. Other symbols bear customary meaning. If the fields are monochromatic with angular frequency ω and its time dependence can be expressed in complex notation $\exp(-i\omega t)$. Spatial variation of field vectors can be represented by two dimensional Fourier integral:

$$\underline{\underline{U}}(\underline{\rho}, z) = \int \underline{\underline{u}}(\underline{\kappa}, z) e^{i\underline{\kappa} \cdot \underline{\rho}} d\underline{\kappa}$$

where $\underline{\kappa} = \kappa_x \hat{x}_0 + \kappa_y \hat{y}_0$ is a vector spatial angular frequency. Bold face $\underline{\underline{U}}(\underline{\rho}, z)$ represents field quantity in space and italic $\underline{\underline{u}}(\underline{\kappa}, z)$ represents its Fourier component.

In such a field, differentiation in time $\frac{\partial}{\partial t}$ is always equivalent to multiplication $-i\omega$ and Eq. (B1) can be written as

$$\nabla \times \left(\int \underline{\underline{g}}(\underline{\kappa}, z) e^{i\underline{\kappa} \cdot \underline{\rho}} d\underline{\kappa} \right) = \frac{i\omega}{c} \int \underline{\underline{g}}(\underline{\kappa}, z) e^{i\underline{\kappa} \cdot \underline{\rho}} d\underline{\kappa}$$

Since the integration is in $\underline{\kappa}$ space, the order of spatial differentiation and $\underline{\kappa}$ space integration can be interchanged.

$$\begin{aligned} \int [\nabla \times \underline{\mathcal{E}}(\underline{\kappa}, z) + i \underline{\kappa} \times \underline{\mathcal{E}}(\underline{\kappa}, z)] e^{i \underline{\kappa} \cdot \underline{\rho}} d \underline{\kappa} \\ = \int [\frac{i \omega}{c} \underline{\mathcal{D}}(\underline{\kappa}, z)] e^{i \underline{\kappa} \cdot \underline{\rho}} d \underline{\kappa} \end{aligned}$$

Maxwell's equation for component fields in nonmagnetic material ($\mu = 1$) then becomes

$$\nabla \times \underline{\mathcal{E}}(\underline{\kappa}, z) + i \underline{\kappa} \times \underline{\mathcal{E}}(\underline{\kappa}, z) = \frac{i \omega}{c} \underline{\mathcal{H}}(\underline{\kappa}, z) \quad (\text{B3})$$

$$\nabla \times \underline{\mathcal{H}}(\underline{\kappa}, z) + i \underline{\kappa} \times \underline{\mathcal{H}}(\underline{\kappa}, z) = - \frac{i \omega}{c} \underline{\mathcal{D}}(\underline{\kappa}, z) \quad (\text{B4})$$

combining Eq. (B3) and Eq. (B4),

$$\nabla \times \underline{\mathcal{H}}(\underline{\kappa}, z) = - \frac{i \omega}{c} \underline{\mathcal{D}}(\underline{\kappa}, z) - \frac{c}{\omega} [\underline{\kappa} \times \nabla \times \underline{\mathcal{E}}(\underline{\kappa}, z) + i \underline{\kappa} \times \underline{\kappa} \times \underline{\mathcal{E}}(\underline{\kappa}, z)] \quad (\text{B5})$$

Taking curl of Eq. (3B) and substituting it in Eq. (B5).

$$\nabla \times \nabla \times \underline{\mathcal{E}}(\underline{\kappa}, z) = \frac{\omega^2}{c^2} \underline{\mathcal{D}}(\underline{\kappa}, z) + \underline{\kappa} \times \underline{\kappa} \times \underline{\mathcal{E}}(\underline{\kappa}, z) \quad (\text{B6})$$

Using

$$\underline{\mathcal{D}}(\underline{\kappa}, z) = \underline{\epsilon} : \underline{\mathcal{E}}(\underline{\kappa}, z) + 4 \pi \underline{\mathcal{P}}(\underline{\kappa}, z) \quad (\text{B7})$$

and defining equivalent dielectric constant tensor

$$\underline{\epsilon}_e = \frac{\omega^2}{c^2} \underline{\epsilon} - \kappa^2 \underline{I} + \underline{\kappa} \underline{\kappa}$$

where $\underline{\epsilon}$ = linear dielectric constant tensor

$\underline{\phi}(\underline{\kappa}, z)$ = Fourier components of polarization

and

\underline{I} = idemfactor or unit dyadic

Wave equation for angular spectrum becomes

$$\nabla \times \nabla \times \underline{\phi}(\underline{\kappa}, z) - \underline{\epsilon} \cdot \underline{\phi}(\underline{\kappa}, z) = \frac{4\pi\omega^2}{c^2} \underline{\phi}(\underline{\kappa}, z) \quad (\text{B9})$$

$\underline{P}(\underline{\kappa}, z)$ = Fourier components of polarization

and

\underline{I} = idemfactor or unit dyadic

Wave equation for angular spectrum becomes

$$\nabla \times \nabla \times \underline{\delta}(\underline{\kappa}, z) - \underline{\epsilon} \underline{e} : \underline{\delta}(\underline{\kappa}, z) = \frac{4\pi\omega^2}{c^2} \underline{\phi}(\underline{\kappa}, z) \quad (\text{B9})$$

APPENDIX C

FOURIER INTEGRAL REPRESENTATION OF NONLINEAR POLARIZATION

The nonlinear polarization of sum-frequency produced in the nonlinear material is given by

$$\underline{P}(\underline{\rho}, z) = \underline{d} : \underline{E}_p(\underline{\rho}, z) \underline{E}_i(\underline{\rho}, z) \quad (C1)$$

where $\underline{\rho}$ = transverse position in the material

z = longitudinal position in the crystal

$\underline{E}_p(\underline{\rho}, z)$ = electric field of pump beam

$\underline{E}_i(\underline{\rho}, z)$ = electric field of infra-red object wave

\underline{d} = second order polarization tensor

Expressing field quantities in their Fourier integral representation Eq. (C1) becomes

$$\underline{P}(\underline{\rho}, z) = \underline{d} : \int \int \underline{E}_p(\underline{\kappa}_p, z) \underline{E}_i(\underline{\kappa}_i, z) e^{i(\underline{\kappa}_p + \underline{\kappa}_i) \cdot \underline{\rho}} d\underline{\kappa}_p d\underline{\kappa}_i \quad (C2)$$

Using phase-matching condition

$$\underline{\kappa}_s = \underline{\kappa}_p + \underline{\kappa}_i \quad (C3)$$

We write Eq. (C2) as

$$\begin{aligned} \underline{P}(\underline{\rho}, z) &= \int d\underline{\kappa}_s e^{i\underline{\kappa}_s \cdot \underline{\rho}} \left\{ \underline{d} : \left[\int d\underline{\kappa}_i \underline{\mathcal{E}}_p(\underline{\kappa}_s - \underline{\kappa}_i, z) \underline{\mathcal{E}}_i(\underline{\kappa}_i, z) \right] \right\} \\ &= \int d\underline{\kappa}_s e^{i\underline{\kappa}_s \cdot \underline{\rho}} \left[\underline{d} : \underline{\delta}_p(\underline{\kappa}_s, z) \otimes \underline{\mathcal{E}}_i(\underline{\kappa}_s, z) \right] \end{aligned} \quad (C4)$$

where $\underline{\mathcal{E}}_i(\underline{\kappa}, z) \otimes \underline{\delta}_p(\underline{\kappa}, z)$ indicate convolution integral.

It now follows Eq. (C4) that Fourier components of the nonlinear polarization at sum-frequency are product of second-order polarization tensor and the convolution of those of the input object and the pump angular spectrum that satisfy the condition Eq. (C3)

$$\underline{\phi}(\underline{\kappa}_s, z) = \underline{d} : \underline{\delta}_i(\underline{\kappa}_s, z) \otimes \underline{\delta}_p(\underline{\kappa}_s, z) \quad (C5)$$

APPENDIX D

MISMATCH FACTOR

We shall carry out the analysis in the index space rather than in the wave vector space. These two spaces are related only by a constant factor ω/c in a way

$$n(\underline{K}) \hat{K}_0 = \frac{\omega}{c} \underline{K}$$

where \hat{K}_0 is a unit vector along the direction of \underline{K} . The constant factor ω/c , therefore, does not appear in the index space.

Referring to Fig. 12 of the text the equation of indicatrix of a uniaxial crystal expressed in the Cartesian coordinate system, in which the z axis makes an angle α with the crystallographic axis Z and the x axis lies in the crystallographic XZ plane, is given by

$$x^2 \frac{\cos^2 \alpha}{n_e^2} + \frac{\sin^2 \alpha}{n_0^2} + \frac{y^2}{n_e^2} + \frac{z^2}{n^2} + 2xz \cos \alpha \sin \alpha \left(\frac{1}{n_e^2} - \frac{1}{n_0^2} \right) = 1 \quad (D1)$$

where

n_0 = index of refraction along the optic axis

n_e = index of refraction normal to the optic axis

n = index of refraction along $\underline{r} = x \hat{x}_0 + y \hat{y}_0 + z \hat{z}_0$

Equation of tangent plane at the point $z = n$, $x = y = 0$ is

$$z + n^2 \cos \alpha \sin \alpha \left(\frac{1}{n_e^2} - \frac{1}{n_0^2} \right) x - n = 0 \quad (D2)$$

If we define ζ to be an angle that the normal to the tangent plane (D2) makes with the z -axis, the equation of tangent plane can be written as

$$z + x \tan \zeta - n = 0 \quad (D3)$$

Comparing Eqs. (D2) and (D3)

$$\tan \zeta = n^2 \cos \alpha \sin \alpha \left(\frac{1}{n_e^2} - \frac{1}{n_0^2} \right) \quad (D4)$$

Equation of indicatrix in the coordinate (x, y, z) expressed in terms of n_0 , n_e , n , and ϵ becomes

$$x^2 \left(\frac{\cos^2 \alpha}{n_e^2} + \frac{\sin^2 \alpha}{n_0^2} \right) + \frac{y^2}{n_e^2} + \frac{z^2}{n^2} + 2xz \frac{\tan \zeta}{n} = 1 \quad (D5)$$

The difference between an arbitrary vector (η_x, η_y, η_z) and a vector (η_x, η_y, η_z) lying on the indicatrix surface is

$$\eta_z - n_z \approx \eta_z - n + \eta_x \tan \zeta + \frac{n}{2} \left[\eta_x^2 \left(\frac{\cos^2 \alpha}{n_e^2} + \frac{\sin^2 \alpha}{n_0^2} - \frac{\tan^2 \zeta}{n^2} \right) + \frac{\eta_y^2}{n_e^2} \right] \quad (D6)$$

Terms containing higher than second power in η_x and η_y are neglected in arriving at Eq. (D6). The assumption is valid for paraxial case.

Eq. (D6) is equal to the mismatch factor defined in Eq. (27)

Chapter 3 in the text

The relation

$$\frac{\cos^2 \alpha}{n_e^2} + \frac{\sin^2 \alpha}{n_0^2} - \frac{\tan^2 \zeta}{n^2} = \frac{n^2}{n_e^2 n_0^2} \quad (D7)$$

can easily be proven by using Eq. (D4) and the relation

$$n = \frac{n_0 n_e}{(n_0^2 \sin^2 \alpha + n_e^2 \cos^2 \alpha)^{1/2}}$$

Using Eq. (D7) we finally obtain the mismatch factor

$$\psi = \eta_z - \eta_z = \eta_z - n + \eta_x \tan \zeta + \frac{n}{2} \left[\frac{n^2 \eta_x^2}{n_e^2 n_0^2} + \frac{\eta_y^2}{n_e^2} \right] \quad (D8)$$

$$n = \frac{n_0 n_e}{(n_0^2 \sin^2 \alpha + n_e^2 \cos^2 \alpha)^{1/2}}$$

Using Eq. (D7) we finally obtain the mismatch factor

$$\psi = \eta_z - \eta_z = \eta_z - n + \eta_x \tan \zeta + \frac{n}{2} \left[\frac{n^2 \eta_x^2}{n_e^2 n_0^2} + \frac{\eta_y^2}{n_e^2} \right] \tag{D8}$$

APPENDIX E

HANKEL TRANSFORM OF $\frac{\sin(ax^2)}{ax^2}$

Hankel transform of $\frac{\sin(ax^2)}{ax^2}$ is defined

$$H(\rho) = \int_0^{\infty} \frac{\sin(ax^2)}{ax^2} J_0(\rho x) x dx \quad (E-1)$$

Changing the variable $ax^2 = y$, it can be written

$$H(\rho) = \frac{1}{2a} \int_0^{\infty} \frac{\sin y}{y} J_0\left(\rho \sqrt{\frac{y}{a}}\right) dy \quad (E-2)$$

Integration by parts gives

$$H(\rho) = \frac{-\rho}{4a^{3/2}} \int_0^{\infty} J_0'(\rho \sqrt{\frac{y}{a}}) y^{-1/2} \text{Si}(y) dy \quad (E-3)$$

where $\text{Si}(y)$ is a sine-integral function defined by

$$\text{Si}(y) = \int_0^y \frac{\sin t}{t} dt = \text{si}(y) + \frac{\pi}{2} \quad (E-4)$$

and

$$\text{si}(y) = - \int_y^{\infty} \frac{\sin t}{t} dt$$

Using the relation

$$J_0'(x) = -J_1(x) \quad (E-5)$$

We can write

$$\begin{aligned}
 H(\rho) &= \frac{\rho}{4a^{3/2}} \int_0^\infty \left[\text{si}(y) + \frac{\pi}{2} \right] y^{-1/2} J_1 \left(\rho \sqrt{\frac{y}{a}} \right) dy \quad (\text{E6}) \\
 &= \frac{\rho}{4a^{3/2}} \int_0^\infty y^{-1/2} \text{si}(y) J_1 \left(\rho \sqrt{\frac{y}{a}} \right) dy + \frac{\pi}{4a} \int_0^\infty J_1(z) dz
 \end{aligned}$$

where change of variable $z = \rho \sqrt{\frac{y}{a}}$ has been used for the 2nd term.

Using the formula

$$\int_0^\infty y^{-1/2} \text{si}(y) J_1(2\sqrt{by}) dy = - \left[\text{si}(b) + \frac{\pi}{2} \right] / \sqrt{b}$$

and

$$\int_0^\infty J_1(z) dz = 1$$

We finally obtain

$$H(\rho) = - \frac{1}{2a} \text{si} \left(\frac{\rho^2}{4a} \right) = \frac{1}{2a} \left[\frac{\pi}{2} - \text{Si} \left(\frac{\rho^2}{4a} \right) \right] \quad (\text{E7})$$

APPENDIX F
EVALUATION OF MISMATCH FACTOR FOR
NEARLY ISOTROPIC CRYSTALS ($\zeta \approx 0$)

Referring to Fig. F1, the mismatch factor ΔK is given by

$$\Delta K = K_{sz} - K_M \quad (F1)$$

$$K_{sz} = K_p \cos \theta'_p + K_i \cos \theta'_i \quad (F2)$$

$$\approx K_p + K_i - \frac{1}{2} (K_p \theta'^2_p + K_i \theta'^2_i)$$

From geometry (Fig. 3 Chapter 2)

$$\theta_s = \frac{y}{s' + D/2} = \theta'_s n_s \quad (F3)$$

$$\theta_p = \frac{y}{p - D/2} = \theta'_p n_p \quad (F4)$$

$$\theta_i = \frac{y}{s - D/2} = \theta'_i n_i \quad (F5)$$

Eliminating y from (F3) and (F4)

$$\theta'_p = \frac{n_s (s' + D/2)}{n_p (p - D/2)} \theta'_s \quad (F6)$$

Eliminating y from (F3) and (F5)

$$\theta'_i = \frac{n_s (s' + D/2)}{n_i (s - D/2)} \theta'_s \quad (F7)$$

Using $\theta'_s = \kappa_s/K_s$, (F6) and (F7). We can rewrite (F2)

$$K_{sz} \approx K_p \cdot K_i - \frac{\kappa_s^2 (s' + \frac{D}{2})^2 n_s^2}{2K_s^2} n_p^2 (p - \frac{p}{2})^2 + \frac{K_i}{n_i^2 (s - \frac{D}{2})^2} \quad (F-8)$$

For the collinear matched nearly isotropic case

$$K_p + K_i = K_M \approx K_s$$

Finally we obtain

$$\Delta K \approx - \frac{\kappa_s^2 n_s^2 (s' + \frac{D}{2})^2}{2K_M^2} \left[\frac{K_i}{n_p^2 (p - \frac{D}{2})^2} + \frac{K_i}{n_i^2 (s - \frac{D}{2})^2} \right] \quad (F-9)$$

If $p = \infty$

$$\Delta K \approx - \frac{\kappa_s^2}{2K_i} \left(\frac{n_s (s' + \frac{D}{2})}{n_i (s - \frac{D}{2})} \frac{K_i}{K_M} \right)^2 = - \frac{\kappa_s^2}{2K_i} \quad (F-10)$$

Since

$$\frac{n_s (s' + \frac{D}{2})}{n_i (s - \frac{D}{2})} = \frac{1}{\beta} = \frac{K_M}{K_i}$$

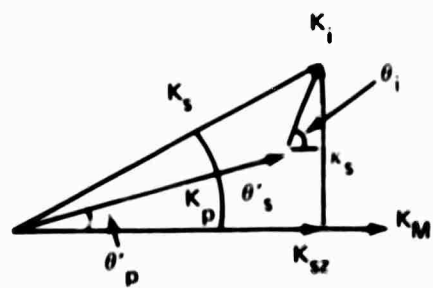


FIGURE F1. WAVE VECTOR RELATION